T.R.
EGE UNIVERSITY
Graduate School of Applied and Natural Science

DEVELOPMENT OF NANOSTRUCTURED COMPOSITE ELECTRODES AND THEIR ANALYTICAL APPLICATIONS

PhD Thesis

Merve AKTÜRK

Department of Chemistry
Analytical Chemistry

İzmir
2023

T.R.
EGE UNIVERSITY
Graduate School of Applied and Natural Science

DEVELOPMENT OF NANOSTRUCTURED COMPOSITE ELECTRODES AND THEIR ANALYTICAL APPLICATIONS

Merve AKTÜRK

Supervisor : Prof. Dr. Zekerya DURSUN

Department of Chemistry
Analytical Chemistry

İzmir
2023

Merve AKTÜRK tarafından Doktora Tezi olarak sunulan **"Development of Nanostructured Composite Electrodes and Their Analytical Applications"** başlıklı bu çalışma E.Ü. Lisansüstü Eğitim ve Öğretim Yönetmeliği ile E.Ü. Fen Bilimleri Enstitüsü Eğitim ve Öğretim Yönergesi'nin ilgili hükümleri uyarınca tarafımızdan değerlendirilerek savunmaya değer bulunmuş ve 12/12/2023 tarihinde yapılan tez savunma sınavında aday oybirliği/oyçokluğu ile başarılı bulunmuştur.

Jüri Üyeleri:	**İmza**
Jüri Başkanı : Prof. Dr. Zekerya DURSUN	**...……...**
Üye : Prof. Dr. H. İsmet GÖKÇEL	**...……...**
Üye : Prof. Dr. Filiz KURALAY	**...……...**
Üye : Prof. Dr. Nuri NAKİBOĞLU	**...……...**
Üye : Prof. Dr. Nur AKSUNER	**...……...**

EGE ÜNİVERSİTESİ FEN BİLİMLERİ ENSTİTÜSÜ

ETİK KURALLARA UYGUNLUK BEYANI

E.Ü. Lisansüstü Eğitim ve Öğretim Yönetmeliğinin ilgili hükümleri uyarınca Doktora Tezi olarak sunduğum **"Development of Nanostructured Composite Electrodes And Their Analytical Applications"** başlıklı bu tezin kendi çalışmam olduğunu, sunduğum tüm sonuç, doküman, bilgi ve belgeleri bizzat ve bu tez çalışması kapsamında elde ettiğimi, bu tez çalışmasıyla elde edilmeyen bütün bilgi ve yorumlara atıf yaptığımı ve bunları kaynaklar listesinde usulüne uygun olarak verdiğimi, tez çalışması ve yazımı sırasında patent ve telif haklarını ihlal edici bir davranışımın olmadığını, bu tezin herhangi bir bölümünü bu üniversite veya diğer bir üniversitede başka bir tez çalışması içinde sunmadığımı, bu tezin planlanmasından yazımına kadar bütün safhalarda bilimsel etik kurallarına uygun olarak davrandığımı ve aksinin ortaya çıkması durumunda her türlü yasal sonucu kabul edeceğimi beyan ederim.

12/12/2023

Merve AKTÜRK

ÖZET

NANOYAPILI KOMPOZİT ELEKTROTLARIN GELİŞTİRİLMESİ VE ANALİTİK UYGULAMALARI

AKTÜRK, Merve
Doktora Tezi, Kimya Anabilim Dalı
Tez Danışmanı: Prof. Dr. Zekerya DURSUN
2023, 136 sayfa

Bu tez çalışması kapsamında analitlere karşı katalitik etkinliği ve seçimliliği yüksek, farklı yüzeyler geliştirilmiştir. Geleneksel elektrotların uygulamalardaki yetersizliği sebebiyle geliştirilen bu elektrotlarda etkin yüzey alanı, yüksek iletkenlik gibi özelliklere sahip olan karbon nanotüp, iletken polimer film ve metal/metal oksit nanoparçacılar ile birleştirilmiş ve yeni elektrot malzemesi olarak kullanılmıştır. Ayrıca grafen oksit ve farklı hibrit malzemeler sentezlenmiş ve belirli oranlarda karıştırılıp elektrot malzemesi olarak kullanılmıştır.

Üç bölümden oluşan bu tezin ilk çalışmasında metal oksit nanoparçacıklar ile modifiye, koşullandırılmış çok duvarlı karbon nanotüp (MWCNT) ve polimer (polifenosafranin) kaplı elektrotlar hazırlanarak rutinin seçimli ve duyarlı tayini gerçekleştirilmiştir. Rutinin modifiye elektrottaki elektrokimyasal davranışı pH 3.0 BR tamponunda incelenmiş ve gerçek örnek analizi rutin tablet örneğinde gerçekleştirilmiştir. Rutine ilişkin yükseltgenme pik akımı Co_3O_4/MWCNT/PPSF/GCE' da $8.0x10^{-9}$ mol L^{-1} – $6.0x10^{-7}$ mol L^{-1} ve $8.0x10^{-7}$ mol L^{-1}– $6.0x0x10^{-6}$ mol L^{-1} aralıklarında iki farklı eğimli doğrusal değişim göstermekte olup belirtme alt sınırı $3.79x10^{-9}$ mol L^{-1} olarak saptanmıştır (S/N=3).

İkinci çalışmada ise Brodie yöntemi kullanılarak grafen oksit (GO) sentezlendi ve ayrıca kimyasal çöktürme yöntemi ile mangan dioksit-hegzagonal molibden (VI) oksit (MnO_2-$hMoO_3$) hibrit malzemesi sentezlenmiş. Sentezlenen MnO_2-$hMoO_3$ hibrit yapısı % 5 ve % 95 oranında olacak şekilde GO ile DMF içinde süspanse edilerek GCE yüzeyine damlatılmış ve asetaminofen (ACP)'in seçimli ve duyar tayini gerçekleştirilmiştir. ACP'ye ilişkin yükseltgenme pik akımı (5%)(MnO_2-h-MoO_3)+(95%)GO/GCE'de 0.06 µmol L^{-1} ile 10.0 µmol L^{-1} and 20.0 ile 80.0 µmol L^{-1} aralıklarında iki farklı eğimli doğrusal değişim göstermekte olup belirtme alt sınırı 1.33 x 10^{-8} mol L^{-1} olarak saptanmıştır (S/N=3).

Üçüncü çalışmada ise hidrotermal yöntem kullanılarak nikel molibdat ($NiMoO_4$) hibrit malzemesi sentezlenmiştir. Diğer çalışmada sentezlenen GO ile süspanse edilerek elektrot yüzeyine damlatılıp ((5%)($NiMoO_4$)+(95%)GO/GCE); asetaminofen (ACP) ve triptofan (TRP) ın eş zamanlı duyar tayini gerçekleştirildi. (5%)($NiMoO_4$)+(95%)GO/GCE'de ACP için doğrusal aralık $1.0x10^{-7}$ mol L^{-1} – $1.0x10^{-5}$ mol L^{-1}; TRP için ise doğrusal aralık $2.0x10^{-7}$ – $6.0x10^{-6}$ mol L^{-1}'dır. Belirtme alt sınırı ACP ve TRP için sırasıyla $10.0x10^{-9}$ mol L^{-1} ve $7.98x10^{-8}$ mol L^{-1} olarak saptanmıştır (S/N=3). Sentetik idrar örneğinde standart katma yöntemi ile ACP ve TRP tayin edilmiştir.

Hazırlanan metal oksit nano parçacık modifiye polimer film ve karbon nanotüp ve GO+hibrit malzeme elektrot yüzey karakterizasyonları; taramalı elektron mikroskobu, X-ışını foto elektron spektroskopisi, enerji dağılım X-ray spektroskopisi, elektrokimyasal impedans ve X-ışını kırınımı tekniği ile gerçekleştirilmiştir.

Anahtar Kelimeler: rutin, acetaminofen, triptofan, grafen oksit, hegzagonal molibdentrioksit, nikel molibdat, metal oksit, hibrid kompozit, modifiye elektrotlar, kompozit elektrotlar

ABSTRACT
DEVELOPMENT OF NANOSTRUCTURED COMPOSITE ELECTRODES AND THEIR ANALYTICAL APPLICATIONS

AKTÜRK, Merve
PhD Thesis, Chemistry Department
Supervisor: Prof. Dr. Zekerya DURSUN
2023, 136 Pages

In thesis study, different electrode surfaces with high catalytic efficiency and selectivity against analytes were developed. In these electrodes, which were developed due to the inadequacy of traditional electrodes in applications, carbon nanotubes, which have properties such as effective surface area and high conductivity, were combined with conductive polymer film and metal/metal oxide nanoparticles and used as a new electrode material. Additionally, graphene oxide and different hybrid materials were synthesized and mixed in certain proportions and used as electrode materials.

In the first study of this three-part thesis, selective and sensitive determination of rutin was carried out by preparing conditioned multi-walled carbon nanotube (MWCNT) and polymer (polyphenosafranine) coated electrodes modified with metal oxide nanoparticles. The electrochemical behavior of Rutin in the modified electrode was examined in pH 3.0 BR buffer, and real sample analysis was performed on the Rutin tablet sample. The oxidation peak current for the rutin Co_3O_4/MWCNT/PPSF/GCE shows two different inclined linear changes in the ranges of $8.0x10^{-9}$ mol L^{-1} – $6.0x10^{-7}$ mol L^{-1} and $8.0x10^{-7}$ mol L^{-1} – $6.0x10^{-6}$ mol L^{-1}, and the detection limit was found $3.79x10^{-9}$ mol L^{-1}(S/N=3).

In the second study, graphene oxide (GO) was synthesized using the Brodie method, and manganese dioxide-hexagonal molybdenum (VI) oxide (MnO_2-$hMoO_3$) hybrid material was synthesized by the chemical precipitation method. The synthesized MnO_2-$hMoO_3$ hybrid structure was suspended in DMF with GO at the ratio of 5% and 95% and dropped onto the GCE surface, and selective and sensitive determination of acetaminophen (ACP) was carried out. The oxidation peak current for ACP (5%)(MnO_2-h-MoO_3)+(95%)GO/GCE have shown a

linear change with two different slopes in the ranges of 0.06 μmol L^{-1} to 10.0 μmol L^{-1} and 20.0 μmol L^{-1} to 80.0 μmol L^{-1} and the LOD was $1.33x10^{-8}$ M (S/N=3).

In the third study, nickel molybdate ($NiMoO_4$) hybrid material was synthesized using the hydrothermal method. It was suspended with GO synthesized and dropped onto the electrode surface ((5%)(NiMoO4)+(95%)GO/GCE) and simultaneous sensitivity determination of acetaminophen (ACP) and tryptophan (TRP) was performed. A linear changing of peak currents of individual ACP or TRP concentrations were found and the calibration curves were constituted for ACP with two different linear parts at $NiMoO_4$(5%)+GO(95%)/GCE: the first linear part was obtained as from $0.1x10^{-6}$ to $1.0x10^{-6}$ mol L^{-1} and the second linear part from $2.0x10^{-5}$ to $1.0x10^{-5}$ mol L^{-1} and the calibartion curve was constructed in the concentration range of TRP from $6.0x10^{-7}$ – $6.0x10^{-5}$ mol L^{-1}. The detection limits were found to be 10.0 nmol L^{-1} ACP and 0.798 nmol L^{-1} TRP respectively.

Electrode surface characterization of the prepared metal oxide nanoparticle modified polymer film and carbon nanotube and GO+hybrid material were carried out using scanning electron microscopy, X-ray photoelectron spectroscopy, energy dispersion X-ray spectroscopy, electrochemical impedance and X-ray diffraction techniques.

Key Words: rutin, acetaminophen, tryptophan, graphene oxide, hexagonal molybdenum trioxide, nickel molybdate, metal oxide, hybrid composite, modified electrodes, composite electrodes

ÖNSÖZ

Nanobilim ve nanoteknoloji, tüm bilim disiplinlerini ve mühendisliği bünyesinde barındıran, gelişmekte olan bir alandır ve "Nanoteknoloji ve ileri malzeme teknolojisinin" gelişimine uygun olarak, nanometre boyutundaki fonksiyonel malzemelerin tasarımı, üretimi ve karakterizasyonunun iyileştirilmesi gerekmektedir. Son yıllarda artan hızda birçok bilimsel araştırmada öncelikli olarak tercih edilen ve farklı konular üzerine çalışılmaya imkan sağlayan elektrokimyasal araştırmalara tez çalışmam ile katkıda bulunmak benim için büyük bir mutluluktur.

Bu amaçla bu tez çalışması kapsamında biyolojik önem sahip olan maddelerin tayini için çeşitli yüzeyler geliştirilmiştir. İlk olarak rutinin elektrokimyasal davranışı polimer, çok duvarlı karbon nanotüp ve metal oksit komposit elektrot yüzeyinde incelenmiştir. Diğer çalışmalarda ise grafen oksit ve çeşitli hibrit malzemelerin sentezi gerçekleştirilmiştir. GO ve hibrit malzemelerden süspanse oluşturularak elektrot yüzeyine damlatılıp acetaminofen ve eş zamanlı asetaminofen ve triptofanın tayini gerçekleştirilmiştir.

Yapılan tüm çalışmaların merdiven basamakları gibi bizleri bir adım öteye taşıyan ve aynı zamanda bambaşka bakış açıları ile bakabilmemizi sağlayan bilimsel çalışmalara, doktora tezimde yaptığım çalışmalarım ile ufak da olsa katkı sağladığım için mutluluk duymaktayım. 2017 yılında başladığım ve iş hayatım ile birlikte yürüttüğüm tez sürecimde, sevgili danışman hocam Prof. Dr. Zekerya DURSUN ve değerli tez izleme jüri üyelerim Prof. Dr. H. İsmet GÖKÇEL ve Prof. Dr. Filiz KURALAY'a tüm bilgi birikimlarini sabır ve yol göstericiliği ile bana sundukları için teşekkür ederim. Ayrıca bu tez çalışması kapsamında yürütülen FDK-2020-21471 numaralı bilimsel araştırma projesi için maddi destek sağlayan Ege Üniversitesi Bilimsel Araştırma Enstitüsü'ne de teşekkür ederim.

İZMİR Merve AKTÜRK

12/12/2023

CONTENTS

Page

CONTENT (Continued)

Page

CONTENT (Continued)

Page

CONTENT (Continued)

Page

LIST OF FIGURES

Figure **Page**

LIST OF FIGURES (Continued)

Figure **Page**

LIST OF FIGURES (Continued)

Figure **Page**

LIST OF FIGURES (Continued)

Figure **Page**

LIST OF FIGURES (Continued)

Figure **Page**

LIST OF FIGURES (Continued)

Figure **Page**

LIST OF FIGURES (Continued)

Figure **Page**

LIST OF FIGURES (Continued)

Figure **Page**

LIST OF FIGURES (Continued)

Figure **Page**

LIST OF FIGURES (Continued)

Figure **Page**

LIST OF FIGURES (Continued)

Figure **Page**

LIST OF FIGURES (Continued)

Figure **Page**

LIST OF FIGURES (Continued)

Figure **Page**

LIST OF FIGURES (Continued)

Figure **Page**

LIST OF TABLES

Table **Page**

LIST OF TABLES (Continued)

Table **Page**

LIST OF TABLES (Continued)

Table **Page**

ABBREVIATIONS AND SYBMBOLS

SWV	Square Wave voltammetry
ACP	Acetaminophen
TRP	Tryptophan
h-MoO_3	Hexagonal Molybdenium (VI) Oxide
CV	Cyclic voltammetry
EIS	Electrochemical impedance spectroscopy
GCE	Glassy carbon electrode
LOD	Limit of detection
MCM	Mesoporous carbon material
PPSF	Poli(phenosafranine)
SEM	Scanning electron microscopy
TEM	Transmission Electron Microscope
XPS	X-ray photoelectron spectroscopy
XRD	X-ray diffraction
Z	Impedance

1. INTRODUCTION

Electroanalytical techniques have attracted significant interest of organic and inorganic compounds with large linear concentration range, high sensitivity and selecticity easy to use instrument software and low cost. Since the conventional working electrodes are not stable due to the electrode materials oxidize at even low positive potentials and have slow surface kinetics. These properties causes low sensitivity and worst selectivity. Therefor they did not meet the expectations. In addition, it is quite challenging to separate peaks for analytes that have oxidation or reduction potentials that are very close to one another. Therefore the conventional electrodes have some limitations in voltammetric studies (Baig, N. et.al., 2019). It is clear that the importance of electrode material in the development of high-performance electrochemical sensors is required.

In recent years, many studies have been attracted great interest on the preparation of nanomaterials nanohybrite materials and composites by combining a conducting polymer with metal/metal oxide stuructures. Conducting polymers containing composite materilas have a porous morphology to modified the surface with metal/metal oxide nanoparticles, improve the stability, electrical and ionic conductivity of the composite materials. Therefore the nanocomposite electrodes have been widely used for analytical applications with high selectivity and sensitivity (Zhu et.al., 2015).

In last three decades, the integration of nanomaterials has had a significant influence on the development of electrochemical sensors. In electrochemical methods, conductive polymers, organic and inorganic compounds, metal nanoparticles, metal oxides, carbon-based materials and hybrid materials have also been frequently used to electrode modification. They play a crucial part in the process of achieving sensitive and selective detection of organic and inorganic substances with a high degree of stability and precision.

In spite of nanocomposites own a extensive range of applications, there are several subject matter to be analyzed. The properties of nanocomposites, such as; the shape, dimension, agglomeration, size distribution, crystallinity and defect structure, play a major act on the electrode’s performance in analytical applications

and there is still a need to develop these features.. Generally, three main purpose, including the forming of active sites, enhancing electronic conductivity, and constituting a porous structure in nanocomposite structure, have been defined to prove the electrode's surface chemistry and therefore improve the composites performance and a encouraging alternative to conventional electrode materials.

1.1. The Aim of the Thesis

This thesis study consists of two purposes; the first purpose was to developed composite electrodes from metal/metal oxide nanoparticles (based on gold, copper, cobalt, nickel, etc.) multiwall carbon nanotube (MWCNT) and condicting polymer containing film covered glassy carbon electrodes (GCE) for sensitive and selective detection of rutin. In this study; optimization studies were carried out by varying type of metal/metal oxide nanoparticles, electrochemical deposition of metal/metal oxide cycle number, MWCNT ratio, monomer concentration, polymer cycle number, and supporting electrolyte pH using cyclic voltammetry. The ontained data for first purpose show that an Co_3O_4 nanoparticles decorated on MWCNT poly(phenosafranine) composite electrode was found to have the highest activity towards rutin determination.

The second purpose of the this thesis was syhentheis of graphene oxide (GO) and different hybrid metal oxide materials (MnO_2:h-MoO_3; NiV_2O_4; $NiMoO_4$; ZrO_2+CeO_2) to prepare a composite electrodes for sensitive and selective individual determination of acetaminophen; and also simultenaous determination of acetaminophen (ACP) and tryptophan (TRP). Based on this purpose, newly synthesized hybrid materials were attached with GO in different ratio to form a perfect surface with high surface area of composite electrode for indiviual or simultaneous detection of ACP and TRP. The morphological, chemical and electrical surface characterization of these developed composite electrodes were identified by scanning electron microscopy (SEM), cyclic voltammetry, X-Ray photoelectron spectroscopy (XPS), X-Ray diffraction (XRD), energy dispersive X-Ray spectroscopy (EDX) and electrochemical impedance spectroscopy (EIS).

1.2. Modified Electrodes

Modified electrodes, also known as chemically modified electrodes (CMEs) or functionalized electrodes, that have been intentionally altered or enhanced by the addition of a modifier or a surface coating. These modifications are typically carried out to enhance the performance of the subsrate electrode material in electrochemical processes.

There are various reasons why modified electrodes are used in electrochemistry:

- *To improve the charge or electron transfer rate for selective and sensitive detection of analytes:* Modifying the electrode surface can significantly prove the charge or electron transfer rate while resolving the peaks formation in simultaneously determinations. Therefore, the modified electrodes can be improved the selectivity for a particular analyte or class of analytes by incorporating specific receptors or modifiers, the modified electrode can discriminate against interfering species, leading to more accurate and reliable electrochemical measurements (Eden E. L. Tanner and Richard G. Compton, 2018; Fagan-Murphy et.al, 2015). On the other hand the modification procedure can also increased the electrode active surface area for sensitive detection of analytes. These can be achieved by introducing specific functional groups or nanoparticles that facilitate the selective recognition or electrocatalytic activity towards the target species. The modifiers or surface coatings can amplify the signal response, allowing for the detection of analytes at lower concentrations with lower detection limits.

- *Stability and Longevity:* Electrochemical processes can sometimes cause electrode degradation or fouling over time, leading to reduced performance. Modification can protect the electrode surface from fouling or enhance its stability, resulting in a longer term storage and more reliable measurements.

- *Reduced Overpotentials:* Certain electrochemical reactions require high overpotentials to proceed, leading to increased energy consumption.

Modification can reduce the overpotential required for these reactions, making them more efficient and potentially reducing energy consumption.

- *Electrochemical Catalysis:* Modification of electrodes can facilitate specific electrochemical reactions by acting as catalysts. These modified electrodes can enhance reaction rates, lower overpotentials, and improve the overall efficiency of electrochemical processes.

Examples of modifications used in electrode surfaces include the deposition of thin films, electrodeposition of metal nanoparticles, attachment of biomolecules, adsorption of specific polymers, or incorporation of redox mediators. These modifications can be tailored to suit the requirements of the specific electrochemical application.

Overall, the use of modified electrodes in electrochemistry provides a versatile platform for improving the performance and expanding the application range of electrochemical systems, including sensors, biosensors, fuel cells, batteries, and many other electroanalytical techniques.

1.2.1. Preparation of chemically modified electrodes

Chemically modified electrodes (CMEs) play a crucial role in various electrochemical applications, including sensing, energy conversion, and catalysis. The preparation of CMEs involves modifying the surface of conventional electrodes with different materials or functional groups to enhance their electrochemical performance. In following paragraphs are some common methods used to prepare chemically modified electrodes in electrochemistry:

Electrochemical Deposition: This method involves electrochemically depositing a layer of desired material onto the electrode surface. It can be done by applying a potential to the working electrode in a solution containing the precursor of the desired material. The deposition can be controlled by adjusting the deposition potential, time, and concentration of the precursor (Tonelli et.al., 2019).

Chemical Vapor Deposition (CVD): CVD involves the deposition of a thin film on the electrode surface using chemical reactions in the gas phase. The precursor gas is introduced to the reaction chamber, where it undergoes a chemical reaction and deposits the desired material onto the electrode surface (Creighton and Ho, 2001).

Langmuir-Blodgett Technique: This method involves transferring a monolayer of molecules from the air-water interface onto the electrode surface. The molecules are spread as a monolayer on the water surface and then transferred to the electrode by vertically dipping the electrode into the water subphase (Ariga et.al, 2013).

Sol-Gel Method: In this technique, a precursor solution is prepared by hydrolyzing and condensing metal alkoxides or other precursors. The solution is then applied to the electrode surface, and subsequent drying and calcination processes lead to the formation of a thin film or coating with desired properties (Bokov et al., 2021).

Physical Vapor Deposition (PVD): PVD methods, such as sputtering or evaporation, involve the deposition of a thin film onto the electrode surface by physical means. The precursor material is vaporized and condensed onto the electrode, forming a thin film with controlled thickness and composition (Uzakbaiuly et al., 2021).

Surface Functionalization: This involves attaching functional groups or molecules to the electrode surface using appropriate chemical reactions. For example, the electrode surface can be modified with specific functional groups through diazonium chemistry, thiol chemistry, or silanization reactions (Chen et al., 2012).

Polymer Coating: Electrodes can be modified by coating them with conductive polymers, such as polyaniline, polypyrrole, or polythiophene. Polymer coatings can provide improved electrochemical properties, stability, and selectivity (Malinauskas, 2001; Koçak and Dursun, 2013).

1.2.2. Chemically modified electrodes types and their applications

Research into developing composite modified materials, in particular for electrode modification, that have unique capabilities thanks to the synergistic effect of two or more functional materials, has increased significantly in recent years. These conductive modifiers such as; conductive polymers (Koçak and Dursun, 2013); carbon based materials (MWCNTs and graphene oxide) (Aktürk, M. et.al., 2018; Dalkıran et.al., 2017); metal nanoparticles (Lavanya et.al., 2021); metal oxides (Poo-arporn et.al., 2019); hybrid metal oxides (Li et. al.; 2019; Isacfranklin et.al., 2020) were commonly utilized for modified electrode preparation. The next paragraphs provide extensive information on the modifiers utilized in this thesis.

1.2.2.1. Conducting polymer films

In the mid-1970s, the collaborative work of three scientists, Alan Heeger, Alan MacDiarmid, and Hideki Shirakawa, led to the discovery of the first inherently conducting polymer, polyacetylene. This breakthrough marked a significant milestone in the field of materials science and chemistry. The groundbreaking work on conducting polymers was recognized with the Nobel Prize in Chemistry in the year 2000. Alan Heeger, Alan MacDiarmid, and Hideki Shirakawa were jointly awarded this prestigious prize for their pioneering contributions to the field. Conducting polymers are often referred to as "intelligent materials" because of their extraordinary properties. These materials exhibit electrical conductivity while still being organic polymers, which is quite remarkable. This characteristic results from the delocalization of electrons along the chain of polymer molecules. (Wallace et al., 2002)

Conducting polymers are characterized by their delocalized π-electron systems, which are formed by the overlap of p-orbitals along the polymer backbone. This delocalization allows the movement of charge carriers (electrons or holes) through the polymer structure, giving rise to electrical conductivity (Wagner, 2013).

Some commonly studied conducting polymers include polypyrrole (PPy), polyaniline (PANI), polythiophene (PTh), and poly(phenosafranine) (PPSF) which are used wide range areas including organic electronics, energy storage and conversion, biosensors, and corrosion protection. These polymers can be synthesized through various methods, including chemical polymerization, electrochemical polymerization, and oxidative coupling reactions (Jaymand, 2014).

Many researchers have studied polymer film-modified electrodes, which are explained in the next few paragraphs.

Karabiberoğlu and coworkers utilizing an over-oxidized and electrochemically polymerized rutin film on GCE, a new facile and sensitive method was developed to individually and simultaneous detection of catechol (CC) and hydroquinone (HQ). Firstly, the electrode was put in a solution of PBS (0.1 mol L^{-1} pH 7) in the presence of 1.0 mmol L^{-1} Rutin and 25 current- potential cycles were performed between 1.3 V and +1.8 V at a rate of 0.2 V s^{-1}. The name for the resulting electrode is PRT/GCE. The electrode was kept at 1.0 V

constant potentail for 150 s in NaOH solution using the chronoamperometry technique to prepare ox- PRT/GCE. The final obatined electrode was used individually and simultaneously determination of CC and HQ by DPV in a pH 7.2 PBS. The LOD values for CC and HQ were 8.8 nmol L^{-1} and 5.2 nmol L^{-1}, respectively, when they were estimated on individually. For simultaneous measurement, the detection limits for CC and HQ were found to be 31 nM and 53 nM, respectively. Also, real sample analysis were also carried out in tap water and waste water (Karabiberoğlu et al., 2019).

Selvaraju and Ramaraj have studied simultaneously determination of AA, DP and serotonin (5-HT) using poly(phenosafranine) (PPS) modified electrode. The electrochemical deposition of PPS films on the GC electrode was carried out using 5.0 x 10^{-4} mol L^{-1} phenosafranine (PS^{+}) aqueous solutions in 50.0 mmol L^{-1} H_2SO_4. Glassy carbon electrode immersed in the solution and polymerized with 28 potential cycles between -0.50 and 1.30 V. The poly(phenosafranine) film-modified electrode was shown a considerably enhance AA and DA separation as well as simultaneous measurement of AA, DA, and 5-HT (Selvaraju and Ramaraj, 2003).

1.2.2.2. Carbon Based Materials

Carbon-based nanomaterials refer to a wide range of materials that are composed predominantly of carbon atoms and exhibit unique properties at the nanoscale. These materials have gained significant attention because of their exceptional mechanical, electrical, thermal, and chemical properties. Some of the most commonly studied carbon-based nanomaterials include carbon nanotubes, graphene, fullerenes, and carbon nanofibers (Fig. 1.1). Carbon-based nanomaterials provide the ability to interact with other nanomaterials to create composites with synergistic effect. The related nanomaterials' synergistic impact significantly increases the sensitivity and selectivity of the modified surfaces (Baig et.al., 2019). Carbon-based nanomaterials have the potential to revolutionize various industries, including electronics, energy, medicine, and materials science. Ongoing research aims to further explore their unique properties, develop scalable synthesis methods, and unlock their full potential in diverse applications.

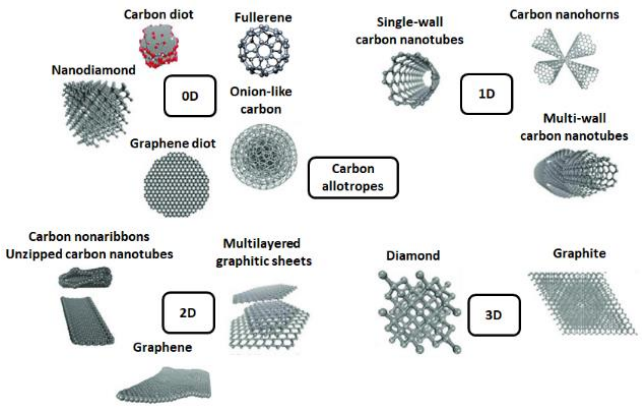

Figure 1.1 Carbon allotropes are categorized by their dimensionality.

Carbon nanotubes :

Carbon nanotubes (CNTs) are indeed one-dimensional cylindrical tubes composed of sp^2 hybridized carbon atoms. The carbon atoms are arranged in a honeycomb lattice structure, similar to graphene. The sp^2 hybridization results in the formation of strong sigma bonds within the hexagonal lattice, while the remaining p-orbitals form delocalized π bonds above and below the plane of the hexagons (Fan et.al., 2017).

CNTs are cylindrical structures made of rolled-up graphene sheets, forming tubes with diameters on the nanoscale. They are considered one of the most important and widely studied carbon-based nanomaterials. CNTs have remarkable mechanical, electrical, and thermal properties, making them attractive for a wide range of applications (Eatemadi et.al., 2014). Carbon nanotubes can be categorized into two main types: single-walled carbon nanotubes (SWCNTs) and multi-walled carbon nanotubes (MWCNTs). SWCNTs consist of a single graphene layer rolled into a seamless cylinder, while MWCNTs consist of multiple layers of graphene concentrically arranged (Fig. 1.2; Alhans et.al., 2018).

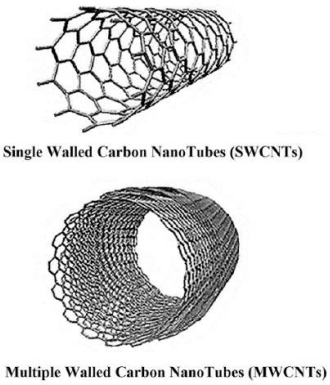

Figure 1.2 Structure of CNTs (Lamberti et.al., 2015)

Carbon nanotubes exhibit exceptional properties. They have high tensile strength, surpassing most other materials, and are highly flexible. CNTs also have excellent thermal conductivity, comparable to diamond, and high electrical conductivity, with values ranging from metallic to semiconducting, depending on their structure.

CNTs show great promise in electronics and computing. Due to their high electrical conductivity, CNTs can be used as components in transistors, interconnects, and other electronic devices. They offer potential advantages over traditional materials, such as silicon, due to their superior electrical properties and smaller size (Liu L. et.al, 2011). Carbon nanotubes continue to be an active area of research, and their unique properties make them versatile materials for a wide range of applications which are energy storage (Jang et.al., 2020; Li, X. et. al., 2022), sensors (Pushpanjal et.al., 2021; Han et.al., 2021), nanomedicine (Harsha et.al., 2019), water purification (Obaidullah, 2019; Roy et.al., 2020).

Babaci and Afrasiabi studied MWCNTs, nickel hydroxide nanoparticles (NHNPs), and MCM-41 modified GCE (MWCNTs-NHNPs-MCM-41/GCE) for the simultaneous determination of dopamine, piroxicam, and cefixime (Babaei and Afrasiabi, 2015). Alizadeh and coworkers synthesized Fe_3O_4 NPs by chemical synthesis method. Then, 0.2 mg of Fe_3O_4 NPs and 0.2 mg of MWCNT were sonicated with 5 ml of DMF for 1.0 h to modifying GCE (Fe_3O_4.NPs@MWCNT/GCE).Fe_3O_4 NPs@MWCNT/GC modified electrode was dried at 50°C for 10 min and used for rifampicin electrochemical sensor (Alizadeh et.al., 2022).

Our research group also studied CNTs that adenine and guanine simultaneous determination were carried out at CeO_2 and Cu nanaoparticles decorated CNTs

modifed GCE in pH 7.0 phosphate buffer solution (Aktürk and Dursun, 2018). In addition, acid treated multiwalled carbon nanotubes and poly(aniline) are effectively deposited on GCE for selective detection of serotonin (Koluaçık et.al., 2018). In other study, Cu-Au bimetallic nanoparticles coated CNTs modified GCE was developed for electrocatalytic reduction of oxygen in alkaline media (Bakır et al., 2011).

Graphene Oxide :

Graphene oxide (GO) is a derivative of graphene, a two-dimensional carbon allotrope consisting of a single layer of carbon atoms arranged in a hexagonal lattice. Graphene oxide is obtained from graphene through a chemical oxidation process that introduces oxygen-containing functional groups onto the graphene sheet, altering its properties and making it more appropriate to certain applications. This process makes GO highly hydrophilic and dispersible in water and other polar solvents, unlike graphene, which is hydrophobic (Sharma, 2018). It retains the sp^2 hybridization of carbon atoms, resulting in its exceptional mechanical strength and flexibility.

GO contains various oxygen functional groups, such as epoxy (-O-), hydroxyl (-OH), and carboxyl (-COOH) groups, attached to the carbon lattice. Due to the presence of oxygen functional groups, GO exhibits strong hydrophilic behavior, enabling it to form stable dispersions in water and other polar solvents. These functional groups provide GO with excellent chemical reactivity, allowing it to interact with other materials and be modified for specific applications.

GO is also widely utilized in composite materials (Darabdhara et.al., 2019; Ahamed et.al., 2021), biomedical (Placha and Jampilek, 2019), supercapacitors (Kakaei et.al., 2019; Korkmaz and Kariper, 2020), solar cells (Lima et.al., 2016) and batteries (Fu et.al., 2016; Liu Y. et.al.,2019), optoelectronics (Karyaoui et.al., 2021), sensors (Hazra and Basu, 2019).

GO has also found in applications of electrochemical determination of biomolecules. Its unique properties, such as excellent electrical conductivity, high surface area, and biocompatibility, make it an attractive material for sensing and detecting various biomolecules.

Karthika and coworkers was studied the electrochemical determination of nicotin using copper tungstate modified reduced GO nanocomposite ($CuWO_4$/rGO) nafion (Nf) immobilized GCE (Karthika et.al., 2019). In other study, a novel nanocomposite based on ruthenium nanoparticles (RuNPs) uniformly constructed at chemically treated GO nanosheets (CTGONS) was created as an active electrode surface for simultaneous determination of DA and AC in the presence of high concentrations of AA (Abdelwahab A. et.al., 2020). Zhang and Liu synthesized nitrogen-doped graphene oxide (N-rGO) materials and then prepared by pyrolysis of poly(p-phenylenediamine)-rGO (PpPD-rGO) hybrids for simultaneous detection of DP, AA and UA. (Zhang and Liu, 2020). Sohouli and coworkers syhthesized GO by Hummer's method and iron oxide nanoparticles (Fe_3O_4) were synthesized by the co-precipitation method. Also methyl cellulose (MC) modified GO was syhthesized (MC-GO). The dropdrying approach was employed to deposit the MC-GO-Fe_3O_4 composite on the GCE surface. The modified GCE was used for determination of uric acid in urine samples (Sohouli et. al., 2020).

These data indicate a highly efficient route to the synthesis of graphene-based compounds for use in electrochemical sensing.

1.2.2.3. Metal Nanoparticles

The distinct properties of MNPs have made them versatile and valuable in several scientific and technological fields, including materials science, chemistry, physics, biomedicine and nanotechnology (Di Ventra et. al., 2004). Metal and metal oxide nanoparticles own acquired considerable attention in the field of modified electrodes due to their unique properties and potential applications. These nanoparticles offers several advantages, such as high surface area, improve catalytic activity, enhance electron transfer kinetics and tunable properties, making them suitable for various electrochemical applications.

Metal and metal oxide nanoparticles (MNPs) can be synthesized on various materials using a range of methods. Physical methods, containing microwaves, sonication, laser, UV, plasma and supercritical fluids rutes to synthesize metal or metal oxide nano particles Chen et.al., 2019). The chemical synthesize methods are co-precipitation and deposition–precipitation, impregnation, emulsions, chemical

vapor impregnation, photochemistry, chemical and electrochemical reduction (Guzmán et.al., 2009).

These are electrodeposition (Chen et.al., 2019), sol-gel method (Parashar et.al., 2020), physical vapor deposition (PVD) (Gholami et.al., 2020), atomic layer deposition (ALD) (Lu, J., 2021). The other MNPs synthesize method is used a sonoelectrochemistry and flame spray pyrolysis routes as physico-chemical method (White et.al., 2009).

The preference of nanoparticle depends on the specific application requirements, such as desired properties, stability, and compatibility with the electrode material and target analyte. Of all these mentioned tecniques electrochemical tecniques offer some adventages such as control over particle size, density, and purity, along with low cost and short preparation time. Electrodes that have been modified by metal nanoparticles have also been used in electroanalysis for molecules that are organic, inorganic and biologically important molecules. The recent examples of electrocanalytical applications is given following paragraphs.

Tajyani and Babaei syhenthized Fe_3O_4@NiO core/shell MNPs using solvothermal/decomposition method and modified carbon paste electrode (Fe_3O_4@NiO/CPE). The modified electrode used for simultaneous determination of quercetin and tryptophan (Tajyani and Babaei, 2019). In other study, graphene oxide and Au nanoparticles co-electrodeposition method into a ITO-PET substrate for detection of dopamine. Au NPs characterized SEM and dimension of about 28nm have been deposited (Patella et.al., 2019).

Sujie Xing and coworkers was prepared by nafion and silver nanoparticles for detection of Cr (VI) using lineer sweep voltammetry. Ag nanoparticles were electrodeposited at the GCE/ Nf electrode 0.8 V (Ag/AgCl) for 400 s in containing 0.1 mM $AgNO_3$. The proposed sensor was implemented in practice to detect low concentrations of Cr (VI) in real water samples (Xing et.al., 2011). Chikere et.al. studied cobalt oxide nanoparticles modified carbon paste electrode (CoO-NPs-CPE) for sensitive determination of Gallic acid. The nanoparticles

syhentsized using co-precipitation method. The cobalt oxide nanoparticles were characterized SEM, EDXA, FTIR and a Zetasizer (Chikere et. al., 2021).

Beitollahi and coworkers studied electrooxidation of 6-thioguanine in presence of folic acid at carbon pasta electrode modified ZnO-CuO nanoplates. They synthesized ZnO-CuO nanoplates and 2-chlorobenzoyl ferrocene and utilized to construct a modified carbon paste electrode. The developed modified electrode was shown excellent activity to separate oxidation peaks of 6-thioguanine and folic acid, making it appropriate for detecting 6-thioguanine in the presence of folic acid in real samples (Beitollahi et. al., 2016).

In summary, the incorporation of MNPs onto electrode surfaces offers several benefits, including increased catalytic activity, a larger surface area and unique properties. These advantages make MNPs on catalyst surfaces highly desirable for analytical applications enabling improved sensitivity, selectivity, and efficiency in various analytical techniques.

1.2.2.4. Hybrid Composites

Hybrid composites involve the combination of different materials, but the integration occurs at a submicron level. The term "hybrid" refers to the blending or mixing of materials on a macroscopic scale (Singh et.al., 2019). There have been several definitions of hybrid omposites offered. Some definitions emphasize the hybridization of macroscopic mixtures, while others focus on the submicron scale (Fig. 1.3).

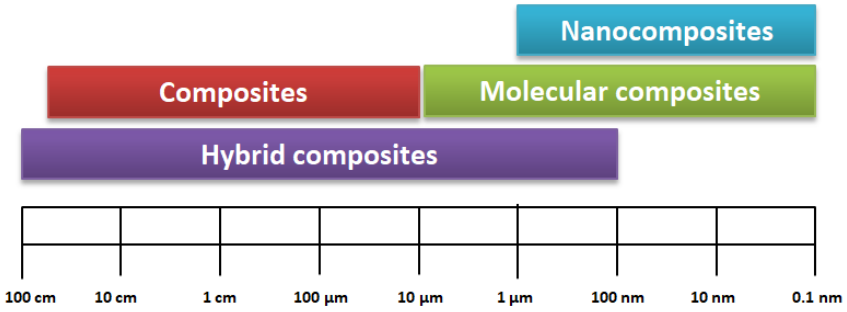

Figure 1.3 Classification of materials at different scale levels.

The concept of hybrid materials, as described by Niizeki in 1986 and Yamada et al. in 1989, aligns with the idea of combining different materials to create new properties. These hybrid materials involve the hybridization of two or more monolithic materials or the formation of new electron orbitals between different materials, resulting in a mixture with unique characteristics.

According to Gomez-Romero and Sanchez, the hybrid materials can be categorized based on the characteristic scale and the materials involved. Two common categories are organic-inorganic hybrid materials and inorganic biomaterials with a characteristic scale below 103 nm (Gomez-Romero and Sanchez, 2004). Firstly, Organic-inorganic hybrid materials: these materials combine organic and inorganic components at the nanoscale or molecular level. The organic component typically consists of polymers, small organic molecules, or carbon-based materials, while the inorganic component includes nanoparticles, metal oxides, or other inorganic structures. The combination of organic and inorganic components can lead to unique properties such as improved mechanical strength, enhanced conductivity, or tailored surface properties. Organic-inorganic hybrid materials can be used in different application areas such as electronics, optics, coatings, and biomedical devices.

The other category is inorganic biomaterials at the nanoscale. This category includes inorganic materials with dimensions below 103 nm that are specifically designed for biomedical applications. These materials can include nanoparticles, nanocomposites, or nanostructured surfaces made from inorganic materials like metals, metal oxides, or ceramics. Inorganic biomaterials at the nanoscale are utilized in various biomedical fields, including drug delivery, tissue engineering, biosensing, and medical imaging. Their small size allows for improved cellular interactions, targeted delivery, and enhanced biocompatibility.

In summery, the concept of hybrid materials, as mentioned, refers to mixtures of two or more materials with newly formed chemical bonds. These materials combine the properties of the constituent materials and can exhibit unique properties or enhanced performance compared to the individual components.

1.2.3. Rutin

1.2.3.1. Chemical properties of rutin

Rutin is a flavonol glycoside made up of the flavonol quercetin and the disaccharide rutinose (Fig. 1.4). It is also known as quercetin-3-rutinoside or sophorin. Rutin is a flavonoid derivative belonging to the group of flavonols. Flavonoids are a class of polyphenolic compounds commonly found in various fruits, vegetables, and plants. for example are found in buckwheat seed, fruits and fruit rinds, especially in citrus fruits. The chemical structure describes the arrangement of the quercetin core with two sugar moieties (rutinose) attached to it (e.g. orange, grapefruit, lemon, lime) (Mauludin et.al., 2009; Aktürk and Dursun, 2023).

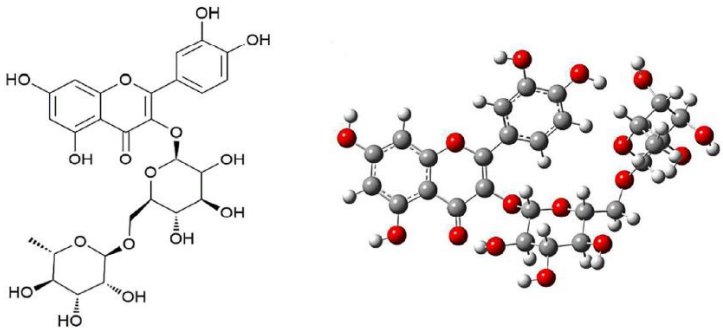

Figure 1.4 Chemical Structure of Rutin

Rutin is known for its potential health benefits due to its antioxidant and anti-inflammatory properties. It also has for its potential health utility which include its effects on capillary permeability and blood pressure. Therefore to treat hemorrhagic diseases and hypertension used (Elancheziyan et.al., 2022). It is therefore important to establish methods for detecting rutin levels in food and pharmaceutical samples.

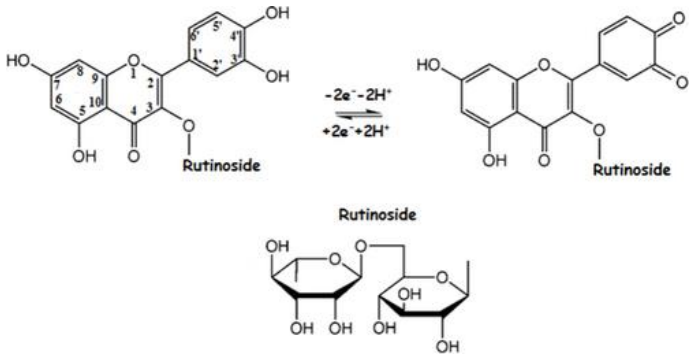

Figure 1.5 Possible mechanism of the electrochemical oxidation of rutin.

1.2.3.2. Determination of Rutin

Up to date, many methods for detection of rutin have been developed using different techniques, such as flourimetric and capillary electrophoresis (Lıu, 2013; Sun et.al., 2003), chemiluminescence (Song and Wang, 2001), high-performance liquid chromatography (Yıldırım et.al., 2017), spectrophotometric determination (Xu et.al., 2010). Electrochemical techniques offer several advantages such as high sensitivity, low cost and fast response to compare with other techniques. Because of this, a lot of study has been published on the electrochemical deterination of rutin up until now.

Askari and coworkers synthesized a binary transition metal oxide, specifically nickel and iron oxide ($NiFe_2O_4$), and then hybridizing it with reduced graphene oxide (rGO) through the hydrothermal method to obtain nanocomposite materials for electrochemical detection of rutin. These nanomaterials were characterized using TEM, SEM, Raman spectroscopy and XRD. The lineer concentration range of rutin were found from 100 nM to 100 μM with the detection limit of 100nM. According to the study, the oxidation mechanism of rutin involves a multi-step process, where the molecule undergoes a two-electron/two-proton oxidation (Askari et.al., 2021).

Another study, functionalized CNTs using H_2SO_4/HNO_3 (3:1) mixture (f-CNT) and prepared CuO nanoparticles. This electrochemical sensor have used for detection of rutin in real herbal samples (Cinnamomum camphora (L.)). DPV analysis was used to study the electrochemical properties of CuO@f-CNTs/GCE. The results suggested that the material exhibited a selective and sensitive electrochemical response. The linear range from 10.0 to 200.0 μmol L^{-1} and a detection limit of 11.0 nmol L^{-1}. The analyte was determined in herbal samples with excellent recoveries (Liu, Z. et.al., 2022).

The one-pot synthesis involves the ultrasonication of graphene oxide and multi-walled carbon nanotubes, followed by the addition of H_2PtCl_6 solution and $NaBH_4$ for reduction. The product is then washed and further treated with an ethanol and water mixture to obtain the desired ternary nanocomposite. The resulting nanocomposite is named Pt@r-GO@MWCNTs. The obtained ternary Pt@r-GO@MWCNTs nanocomposite has shown promising electrocatalytic activity

towards myricetin and rutin. The nanocomposite sensor shows excellent performance such as wide linear range (0.05–50.00 μmol L^{-1} for both analytes), low detection limits (0.010 μmol L^{-1}; 0.005 μmol L^{-1}), good reproducibility, and stability The successful application of the ternary nanocomposite sensor for the simultaneous determination of myricetin and rutin in real orange juice samples is a remarkable achievement (Tursynbolat et.al., 2019).

1.2.4. Acetaminophen

1.2.4.1. Chemical properties of acetaminophen

Acetaminophen (4-acetamidophenol or paracetamol (ACP)) is one of the drugs widely used all over the World. The molecular formula for acetaminophen is $C_8H_9NO_2$ (Fig. 1.6). It consists of a benzene ring with a hydroxyl group (OH^-) and an amide group (-NH) attached to it. The amide group is responsible for its pain-relieving and fever-reducing properties. Acetaminophen is also known as N-acetyl-p-aminophenol.

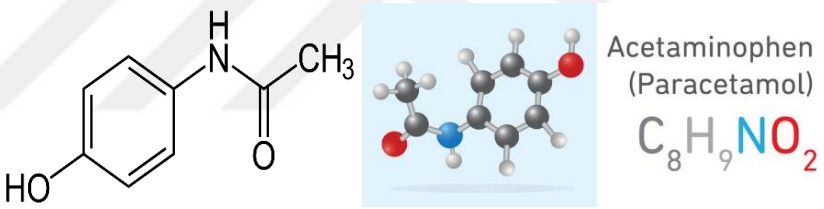

Figure 1.6 Chemical structure of acetaminophen.

ACP is used to treat colds and fevers, as well as to relieve various types of pain, including migraines, muscular pain, and chronic pain (Uzun and Tanablıgil, 2022; Kiaeefar et.al., 2022). Furthermore, for aspirin-sensitive persons and to reduce the danger of Reye's syndrome in newborns, the use of ACP as a medicine has practically replaced the usage of aspirin (Goyal et.al., 2010). The World Health Organization (WHO) recommends an adult daily intake of 1.0 g every 4-6 hours and no more than 4 g ACP in a 24-hour period (Demir et.al., 2020). When ACP content is consumed in excess of the allowed levels, toxic metabolite occurs, resulting in hepatotoxicity and nephrotoxicity, which may cause to the liver and

kidneys damage (Keerthi et.al., 2019). Therefore, determination of ACP is important using analytical methods.

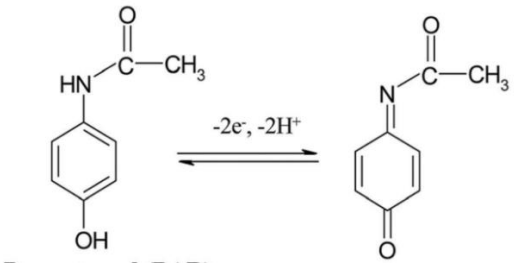

Figure 1.7 Oxidation of Acetaminophen (Uzun, 2022)

1.2.4.2. Determination of Acetaminophen

Various analytical techniques have been applied for the detection of acetaminophen which are spectrophotometry (Dinç and Baleanu, 2002), HPLC (Cook et.al., 2015), capillary electrophoresis (Hernández-Carabalí et.al., 2021). Electrochemical techniques have some superiorities such as simple, low cost and high sensitivity compare with these techniques. Recently, modified electrodes using nanomaterials such as carbon-based (Goyal et.al.2010; Ren et.al., 2022) metal-metal oxides (Baezzat and Jahromi, 2022) and conductive polymer composites (Wei et.al., 2019) have been developed for the detection of ACP. The following paragraphs provided an overview of the electrochemical methods that were used to analyze ACP.

Kiaeefar and coworkers prepared an Ag polyaniline heteropoly acid (Ag/PANI/PW12) nanocomposites containing carbon pasta electrode to determination of acetaminophen. The linear concentration range was found as 6.62×10^{-8} mol L^{-1} – 9.29×10^{-5} mol L^{-1} and detection limit of 0.016 μmol L^{-1} (Kiaeefar et.al., 2022).

SnO_2 nanoparticles with functionalized MWCNT as a hybrid material were described in recent research as being synthesized with hydrothermal-assisted synthesis. The SnO_2@f-MWCNT/GCE has high electrocatalic activity for detection of acetaminophen. It has low detection limit (0.36 nmol L^{-1}) and wide lineer range (0.001 to 673 μmol L^{-1}). In addition the SnO_2@f-MWCNT-modifed electrode showed high reproducibility, repeatability, long term storage, and stability (Vinoth and Wang, 2023).

In another published study, two different metal nanoparticles containing modified electrode was deveopled by synthesizing GN/PDA Au@Pt/Au nanoflowers for electrochemical detection of ACP. For this aim firstly, dopamine polymerized onto graphene (GN) surface to obtain GN/PDA and the the Pt and Au alloy NPs was attached GN/PDA nanocomposites that used for substrate. The developed electrode was applied to detection of paracetamol level in wastewater and paracetamol tablet samples (Shi et.al, 2020).

1.2.5. Tryptophan

1.2.5.1. Chemical properties of tryptophan

Tryptophan (2-amino-3-(1H-indol-3-yl)-propionic acid) is an essential α-amino acid, and it must be obtained through the diet because the human body cannot synthesize it. Tryptophan, also denoted by the symbols Trp or W, is a α-amino acid that plays a role in the production of proteins. The molecular formula for tryptophan is $C_{11}H_{12}N_2O_2$ (Fig. 1.8). Tryptophan is polar because of its –amino and -carboxylic acid groups, and indole on the side chain, and non-polar because of its aromatic beta carbon substituent. It is one of the 20 standard amino acids that serve as the building blocks of proteins.

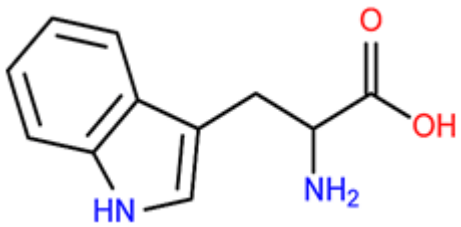

Figure 1.8 Chemical structure of tryptophan.

Tryptophan can be formed in various food products, particularly in foods like chocolates, eggs, and milk, as well as in other protein-rich sources like meats, nuts, and seeds (Beitollahi, 2019). Tryptophan plays a crucial role in various physiological processes and is involved in the synthesis of important molecules such as serotonin and melatonin. A positive nitrogen balance is crucial to human nutrition, and TRP is an essential component of proteins that is required for this balance to be established and maintained. In particular, defective TRP metabolization might result in a waste product in the brain, which can produce hallucinations and delusions (Mao et. al, 2012; Kochen, W. and Steinhart, H.

Eds.1994). Thus, it is of important to develop a simple, fast and inexpensive method for the detection of TRP.

1.2.5.2. Determination of tryptophan

To date, there are several methods for determining tryptophan levels in samples including fluorescence spectroscopy (Reynolds, 2003), HPLC (Zhen et.al., 2011; Çevikalp et.al., 2016), and electrochemical methods (Mattioli et. al., 2019; Mehmandoust et.al., 2021). Among these methods, electrochemical techniques stand out because they are faster, more economical, high selectivity and sesitivity. The tryptophan studies with voltammetric techniques are summarized following paragraphs.

A solvothermal approach was used to generate cerium dioxide (CeO_2) nanoparticles, and a modified Hummers method was used to prepare GO. Nanocomposites of CeO_2 and rGO were coated on the electrode surface using an electrochemical technique. A CeO_2-GO nanocomposite suspension was prepared and coated the GCE surface. Then a constant potential as -1.2 V for 120 s was applied on the CeO_2/GO/GCE surface for reducing the GO. The prepared electrode (denoted as nano-CeO_2/rGO/GCE) used for determination of tryptophan. The current was increased by TRP concentration in the range of 0.01–10 μmol L^{-1} with 6.0 nmol L^{-1} LOD (Nie et.al., 2020).

In another study, multiwallled carbon nanotube was functionelized using sulphuric acid and nitric acid (3:1). The F-MWCNT was dispersed in of pure water and drop into the GCE. This paper deals with development of a diferential pulse voltammetric method for determination of TRP at F-MWCNT/GCE. The infuence of various interference substances on TRP voltammetric signal has been investigated by the DPV method. The content of TRP in fresh milk have determiened by developing the electrode and method (Mehmandoust et. al., 2021).

The other study used differential pulse voltammetry to study the simultaneous determination of AA, DP, UA, and L-tryptophan (L-Trp). In this study, Ag nanoparticles and poly(l-arginine)- GO composite electrode (GCE/AgNPs/P(Arg)-GO) have been fabricated. All analytes can be easily separated at the GCE/AgNPs/P(Arg)-GO electrode. Based on the results of DPV, there were linear relationships between the peak currents and the analytes concentrations in the

ranges of 0.05–50.0 mol L^{-1} for DA, 4.0–2400.0 mol L^{-1} for AA, 0.5–150.0 mol L^{-1} for UA, and 1.0–150 mol L^{-1} for L-TRP, with detection limits (3 s/m) of 0.984, 0.01, 0.142 and 0.122 μmol L−1 for AA, DA, UA and L-TRP, respectively. In addition, the sensor was effectively used to detection of these compounds in human urine samples (Tığ, 2017).

1.2.5.3. Simultaneous determination of Acetaminophen and Tryptophan

Acetaminophen (also known as paracetamol) can alter tryptophan metabolism in the body. Studies have shown that it can inhibit the activity of the enzyme tryptophan 2,3-dioxygenase (TDO) which plays a crucial role in the metabolism of tryptophan. TRP is a precursor for the synthesis of serotonin, a neurotransmitter that plays a key role in regulating mood and emotions. When TDO is inhibited by acetaminophen, the availability of TRP increases, potentially leading to increased production of serotonin and melatonin in the brain. Serotonin and melatonin levels that are abnormal have been linked to depression, Alzheimer's, and Parkinson's illnesses, respectively. The simultaneous determination of ACP and TRP compounds could be of considerable value (Beitollahi, 2019; Mazloum-Ardakani, 2012). The electrochemical methods for simultaneous determination of ACP and TRP were given in the following paragraphs.

Karimi-Maleh and coworkers studied carbon pasta electrode modified with 8,9-dihydroxy-7-methyl-12H-benzothiazolo[2,3-b]quinazolin-12-one (DMBQ) modified multiwalled carbon nanotube. Electrochemical oxidation of isoproterenol (ISPT), ACP, TRP and these mixtures have all been studied. The DMBQ/MWCNT modified electrode showed high catalitic activity for three anlytes. The concentration range of ISPT, ACP and TRP 0.04–400, 5.0–500, and 10.0–800 μmol L^{-1}, with detection limits of 0.009, 1.0, and 4.0 μmol L^{-1}, respectively. DMBQ-MCNTPE was used for determination of ISPT, ACP and TRP in urine, serum, tablet and ampoule samples (Karimi-Maleh et.al., 2014).

Murugan and Kumar were fabricated SnS/TiO_2@GO modified electrode for simultaneous determination of ACP, TRP and caffeine using DPV. Hydrothermal method was used to prepare SnS/TiO_2@GO ternary composite and GO was syhtehesized modified Hummer’s method. Peak currents during separate determination of ACP (9.8 nmol L^{-1} to 280.0 mol L^{-1}), TRP (13.3 nmol L^{-1} to 157.0

mol L^{-1}), and caffeine (16.6 nmol L^{-1} to 333.0 mol L^{-1}) all increased linearly with concentration. The detection limits of ACP, TRP, and caffeine have been obtained as 7.5, 7.8, and 4.4 nmol L^{-1} (3/S), respectively. Wide linear range, high selectivity and stability and low detection limit, were all characteristics of the produced electrode. (Murugan and Kumar, 2019).

In another study, a new nanocomposite electrode has been fabricated based on the (Au/Ag/Pd)NPs/EPGr for the simultaneous determination for AA, DP, ACP and TRP. Firstly, 10 μL of the GrO suspension solution is drop-coated onto the polished GCE surface and left to dry at room temperature, forming a GrO film on the electrode. Then, the GrO film undergoes electrochemical pretreatment by holding the potential at -1.8 V for 5 minutes in a pH 7.0 solution of 0.1 mol L^{-1} PBS. This process results in the formation of an electropolymerized graphene oxide (EPGrO) film on the electrode surface. The electrochemical treatment introduces active sites on the EPGrO surface, potentially facilitating the immobilization of the (Au/Ag/Pd)NPs. The citric acid reduction was used for trimetallic nanoparticles of (Au/Ag/Pd)NPs. The (Au/Ag/Pd)NPs are uniformly capped onto the EPGrO film by immersing the EPGrO-modified electrode in a 0.5% (w/v) aqueous solution of (Au/Ag/Pd)NPs for 2 hours. The immobilization is achieved through physical adsorption, where the NPs are attached to the active sites on the EPGrO surface. After the immobilization step, the (Au/Ag/Pd)NPs/EPGrO/GCE sensor is washed with double distilled water to remove any unbound or loosely attached nanoparticles. The (Au/Ag/Pd)NPs/EPGrO/GCE sensor is ready to use for analytical detection of AA, DP, ACP, TRP. The Au/Ag/Pd)NPs/EPGrO nanocomposite were characterized by XPS, scanning electron SEM, EDX, TEM and XRD. The nanocomposite electrode has an effective electron mediating behavior with large separation peak potentials for AA-DA, DA-AP, and AP-TP, which were calculated to be 0.16, 0.18, and 0.29 V, respectively. Furthermore, the nanocomposite electrode was able to simultaneously determine AA, DA, AP, and TP in linear calibration plots ranging from 5.0 - 650.0 mol L^{-1}, 1.0 - 700.0 mol L^{-1}, 5.0 - 700.0 mol L^{-1} and 1.0 – 600.0 mol L^{-1}, with detection limits calculated at 0.24 0.03, 0.02 0.01, 0.12 0.04, and 0.03 0.01 mol L^{-1}. It was used to analyze how much of these analytes were in a real sample of human blood serum (Abdelvahab et. al., 2020).

1.3. Surface Characterization Techniques

Surface characterization techniques refer to a set of analytical methods used to examine and analyze the properties and features of a material's surface. These techniques are crucial in various scientific and industrial fields, including materials science, chemistry, physics, nanotechnology, and engineering. By understanding the surface characteristics of a material, researchers can gain insights into its composition, structure, morphology, and chemical properties.

Characterization of modified electrodes involves analyzing and understanding the properties and performance of electrodes that have been altered or functionalized with different materials, coatings or surface modifications. These modifications are often made to improve the electrode's sensitivity, selectivity, stability, and other attributes for specific applications, such as in sensors, batteries, fuel cells, and electrochemical analysis. Various techniques are employed to characterize modified electrodes which are electrochemically impedance spectroscopy (EIS), X-Ray Photoelectron Spectroscopy (XPS), cyclic voltammetry (CV), scanning electron microscopy (SEM), X-Ray diffraction (XRD) (Miyoshi, 2002).

1.3.1. Electrochemical Impedance Spectroscopy (EIS)

Electrochemical Impedance Spectroscopy (EIS) is a technique used to study the electrochemical behavior of a system by measuring its impedance response to an applied small-amplitude AC signal over a range of frequencies. The method is widely used in various fields of electrochemistry, materials science, and engineering to understand the fundamental processes governing the behavior of electrochemical systems.

EIS was used to study electrode kinetics in the presence of faradaic reactions. The Randles model is widely employed because it can provide valuable insights into the charge transfer and diffusion processes occurring at the electrode-electrolyte interface. The double-layer capacitance is denoted by Cdl, the resistance of the solution phase is denoted by Rs, and the Warburg impedance, which is caused by constraints placed on mass transport, is denoted by W. The charge-transfer resistance, denoted as Rct, is inversely related to the rate of electron transfer. These

components make up the Randles equivalent-circuit model (Uygun and Uygun, 2014).

The Nyquist plot obtained from EIS have showed distinct features at different frequency ranges. While high-frequency region provides information about charge transfer processes at the electrode-electrolyte interface, low-frequency region provides insights into mass transport processes, such as diffusion and conduction (Qu et. al., 2022).

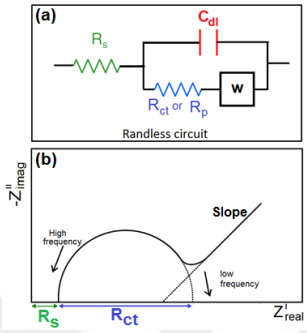

Figure 1.9 Nyquist plot (a) arising from the Randles circuit (b).

1.3.2. X-ray Photoelectron Spectroscopy (XPS)

X-ray Photoelectron Spectroscopy (XPS), also known as Electron Spectroscopy for Chemical Analysis (ESCA), is a powerful surface analysis technique used to determine the elemental composition and chemical state of materials. It provides valuable information about the outermost layers of a material, typically within a few nanometers from the surface. XPS is widely utilized in various fields, including materials science, chemistry, physics, and surface analysis.

XPS have rely on the photoelectric effect, which occurs when X-ray photons are directed at a material's surface. When an X-ray photon interacts with an atom in the material, it can eject a core-level electron from one of the inner electron shells (usually from the 1s or 2s levels) of the atom. The energy of the emitted photoelectron is characteristic of the element from which it originates, and its intensity is proportional to the number of atoms of that element present in the sample (Kloprogge et al., 2020).

In XPS, monochromatic soft X-rays are used to irradiate the sample. Commonly, Mg Kα (1253.6 eV) or Al Kα (1486.6 eV) X-rays are utilized. These X-ray photons have limited penetrating power in a solid, typically on the order of

1-10 micrometers. As a result, they interact mainly with atoms in the surface region of the material, causing photoelectrons to be emitted through the photoelectric effect (Chastain et.al., 1992).

1.3.3. Scanning Electron Microscopy (SEM)

Scanning Electron Microscopy (SEM) is a powerful technique used for surface characterization and imaging at high magnification. The process involves using a focused beam of electrons to interact with the sample's surface, which generates various signals providing information about the sample's topography and composition. SEM utilizes a high-energy electron beam that is scanned across the sample's surface in a raster pattern. The interactions between the electron beam and the sample produce various signals, such as secondary electrons, backscattered electrons, X-ray photons, Auger electrons, and any other photon fluoresans, which can be detected and used for imaging and analysis. Among these signals, backscattered electrons and secondary electrons are the most commonly used for surface imaging. The highly advanced optical lens system helps focus the electron beam onto the sample's surface, allowing for detailed imaging of surface morphology and features. SEM is a versatile technique with applications in various scientific and industrial fields for surface characterization and analysis (Inkson, 2016).

SEM requires a high vacuum environment, conductive samples are easier to work with due to reduced charging effects, and non-conductive samples can be imaged after coating. While SEM is not primarily used for imaging living biological systems, some advancements have enabled limited imaging of cryogenically preserved or hydrated biological samples using specific sample holders in advanced SEM equipment (Skoog et.al., 1998).

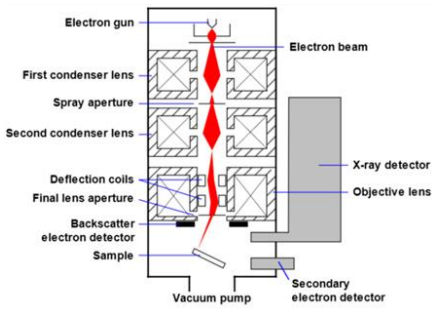

Figure 1.10 Illustration of a SEM.

1.3.4. X-Ray Diffraction (XRD)

X-ray diffraction (XRD) is an analytical technique used to study the structure and composition of crystalline materials. It is widely employed in various scientific fields, including physics, chemistry, materials science, geology, and biology. X-ray diffraction (XRD) and its applications have determined the three-dimensional arrangement of building blocks in crystalline compounds. XRD is indeed a powerful technique used in various fields, including those you mentioned, such as applications in geological prospection, steel/aluminum industries, pharmaceuticals, microelectronics, coatings, cosmetics, paints, and mining.

It is based on the principle of Bragg's law, which describes the scattering of X-rays by a crystal lattice. (n = an integer representing the order of diffraction, λ = wavelength of X-rays, d = spacing between crystal lattice planes, θ = scattering angle)

$$n\lambda = 2d \sin(\theta)$$

In XRD, X-ray radiation is directed at a powdered sample, which contains many randomly oriented crystallites. When the X-rays hit the crystallites at the right angle, they undergo constructive interference, and the X-rays are diffracted into specific directions. By rotating the sample and varying the tilt angle, different crystallites will meet the diffraction condition at various points during the rotation. The diffracted X-rays are detected and analyzed, allowing researchers to determine the angles and intensities of the diffraction peaks. From this information, they can then deduce the lattice parameters and the three-dimensional arrangement of the atoms, ions, or molecules within the crystalline compound (Ali et.al., 2022).

1.4. Voltammetric Techniques

Voltammetry is an electroanalytical technique used to study the behavior of electroactive species in a solution. It involves the application of a controlled potential to an electrode while measuring the resulting current. By varying the applied potential, researchers can investigate the redox properties, electron transfer kinetics and concentration of the analyte in the solution.

The technique relies on polarized electrodes and is typically carried out using a three-electrode system to accurately measure the applied potential on the working

electrode. The three-electrode system consists of a working electrode, a reference electrode (with a known and constant potential), and a counter electrode. The reference electrode ensures accurate potential measurement at the working electrode, while the counter electrode completes the electrical circuit and allows the current (Kounaves, 1997).

In this thesis; CV, SWV and chronoamperometry techniques were used with composite materials modified electrodes.

1.4.1. Cyclic voltammetry

Cyclic voltammetry (CV) has emerge as an necessary and broadly used electroanalytical method in many areas of chemistry. In cyclic voltammetry, a potential that varies linearly with time is applied to a stationary electrode, and a forward potential is ended at a certain value and scanned in the reverse direction. During the forward scan, the electrochemical reaction occurs, leading to the oxidation or reduction of species at the electrode surface. On the reverse scan, the reverse reaction takes place, causing the reduction or oxidation of the same species back to its original state. The resulting CV curve provides valuable information about the redox processes and the behavior of the electrochemical system (Tural et.al., 2006).

Quantitative information in cyclic voltammetry is often obtained through the application of the Randles-Sevcik equation (at 25°C). The Randles-Sevcik equation is derived from theoretical considerations of mass transport and diffusion-controlled electrode processes.

$$i_p=(2.69\times10^5)\cdot n^{3/2}\cdot A\cdot D^{1/2}\cdot C\cdot v^{1/2}$$

i_p is the peak current (A).

n is the number of electrons transferred in the redox process.

A is the electrode area (cm^2).

D is the diffusion coefficient of the electroactive species in the solution (cm^2/s).

C is the concentration of the electroactive species (mol/cm^3 or M).

v is the scan rate (V/s).

1.4.2. Pulse voltammetry

Pulse techniques can significantly reduce the background current and improve the signal-to-noise ratio, leading to lower detection limits in voltammetric measurements. The choice of the most suitable pulse technique depends on the specific electrochemical system being studied and the nature of the background currents to be eliminated. Normal Pulse Voltammetry (NPV) and Differential Pulse Voltammetry (DPV) are two different pulse techniques in voltammetry.

In NPV, successive voltage pulses are applied with increasing amplitudes, and the direct current potential is applied to the electrode. Currents are measured only in a few seconds after each pulse. This results in an increment in the faradaic current and a reduction in the charging current. NPV's focus is on observing changes in faradaic current (current associated with electrochemical reactions) and charging current (current associated with charging the electrode double layer). the limiting currents observed are related to the modification of the Cottrell equation, which describes the relationship between current, time, and concentration for electrochemical reactions. NPV voltammograms tend to have sigmoidal shapes, reflecting the gradual increase in current with increasing pulse amplitude.

In Differential Pulse Voltammetry (DPV), a series of voltage pulses with constant amplitudes are applied to the working electrode. During each differential pulse, the resulting current response is measured. The duration of these pulses is typically very short, and they are applied to the electrode at specific potential points along the potential scan. The primary parameter of interest in DPV is the peak current observed during each differential pulse. DPV voltammograms typically show a sharp peak corresponding to the differential pulse, making it easier to identify and quantify analytes.

In SWV, the potential applied to the working electrode is modulated as a square wave. SWV takes advantage of the difference between these two current measurements (at the rising and falling edges of the square wave) to extract information about the electrochemical reactions occurring at the electrode. It enhances sensitivity because the current is measured twice per cycle, leading to improved signal-to-noise ratios (Wang, 1994; Skoog et al., 2009).

2. EXPERIMENTAL

2.1 Apparatus

Autolab 101 potentiostat/galvanostat was used for CV, square-wave voltammetric (SWV) and chronoamperometric experimental studies. EIS measurements were performed with an Autolab/302 N and a three-electrode system that included a working electrode (*bare GCE, polymer-carbon nanotube composite GCE, various metal nanoparticles modified polymer-carbon nanotube composite GCE, poly(phenosafranine) film GCE, graphene oxide modified GCE, various hybrid molecules modified GCE*), Ag/AgCl (sat. KCl) reference electrode and a platinum wire counter electrode. Electrodes were cleaned in a Bandelin Sonorex type ultrasonic bath. Composites electrodes characterized by scanning electron microscope (SEM) (ZEISS GEMINI 500 and Thermo Scientific Apreo S) and X-ray photoelectron spectroscopy (XPS) (Thermo K-Alpha-Monochromate high-performance spectrometer). The WTW handheld 330i ion analyzer meter pH was utilized in order to carry out the pH measurements.

2.2 Chemicals

All reagents were of analytical reagent quality. Rutin hyrate ($C_{20}H_5N_5$), N-acetyl-para-aminophenol (acetaminophen) ($C_8H_9NO_2$), tryptophan ($C_{11}H_{12}N_2O_2$), ethonol (EtOH), multi-walled carbonanotube (MWCNT-diam: 110-170 nm, lenght: 5-9 micron), cobalt chloride ($CoCl_2.2H_2O$), ammonium chloride (NH_4Cl), alimuna (Al_2O_3), phenosafranine ($C_{18}H_{15}ClN_4$) phosphoric acid (H_3PO_4), boric acid (H_3BO_3), sulfuric acid (H_2SO_4), acetic acid (CH_3COOH), *N*,*N*-dimethylformamide (DMF), graphite, ammonia heptamolybdate tetrahydrate (AHM), manganese dioxide, concentrated nitric acid (HNO_3), nickel nitrate hepta hydrate ($Ni(NO_3)_2.2H_2O$), sodium molybdate (Na_2MoO_4), ammonia (NH_3), sodium hydroxide (NaOH) were supplied from Merck and Sigma Aldrich.

The solutions of phenosafranine monomer in 0.05 mol L^{-1} H_2SO_4, a stock solution of rutin in ethanol, acetaminophen in pH 7.00 PBS and tryptophan in 0.1 mol L^{-1} NaOH were freshly prepared. The $CoCl_2$ solution were prepared in 0.025 mol L^{-1}

NH_4Cl. The Britton- Robinson buffer solutions were prepared in the pH range of 2.25 – 7.0 from an equal mixture of 0.04 mol L^{-1} acetic acid, 0.04 mol L^{-1} boric acid and 0.04 mol L^{-1} phosphoric acid. The pH value was adjusted by titrating with 0.2 mol L^{-1} NaOH solution. A suspension of MWCNT, graphene oxide (GO) and hybrid materials was prepared by distributin each compound in DMF. All electrochemical studies were carried out at room temperature with a continuous flow of high-purity nitrogen over the solution.

2.2.1 Pretreatment of GCE

Various grades of Al_2O_3 slurry (0.05–3 micron) were used to mechanically cleaning the GCE, on a synthetic cloth. After thoroughly cleaning the electrodes with pure water, the electrodes ultrasonicated for 3 minutes treatment in a solution of ultra pure water and ethanol (1:1). Additionally, GCE was electrochemically cleaned by maintaining 1.0 V at constant potential for 10 minutes.

2.2.2 Preparation of Polyphenosafranine (PPSF) Modified GCE

Electrochemical polymerization of 0.1 mmol L^{-1} phenosafranine monomer in 0.05 mmol L^{-1} H_2SO_4 solution was carried out by CV for five cycles between -0.80 V to 1.80 V (vs. Ag/AgCl) with 0.05 V s^{-1} scan rate. The polymer coated electrode represent as PPSF/GCE.

2.2.3 Pretreatment of multiwalled carbon nanotubes

MWCNT is treated with concentrated HNO_3 (65 % ; d:1.42 g mL^{-1}). A 0.1 g MWCNT was boiled in almost 4.0 mL concentrated HNO_3 and then washed with ultrapure water. A black suspension was obtained by dispersing acid-treated MWCNT in DMF.

2.2.4 Preparation of various metal nanoparticles modified MWCNT/PPSF/GCE

Metal nanoparticles were electrochemically modified on MWCNT/PPSF/GCE using CV. CV deposition of Co, Au, Cu, and Ni nanoparticles

on modified electrode surfaces was performed at 50 mV s^{-1} scan rate for 10 cycles at a specific potential window using $CoCl_2$ containing 0.1 mol L^{-1} NH_4Cl, $HAuCl_4$ containing 0.1 mol L^{-1} HCl, $CuSO_4$ containing 0.1 mol L^{-1} H_2SO_4, and $NiSO_4$ containing 0.1 mol L^{-1} H_2SO_4.

2.2.5 Preparation of graphene oxide

The Brodie Method, which has been described in prior research, is used in order to obtain GO (Brodie, 1879; Dreyer, 2010). A beaker was used to combine 2.0 grams of spectroscopically grade pure graphite and 17.0 grams of $NaClO_3$ for this procedure. After that, 50.0 mL of HNO_3 was progressively added to the mixture while it was being chilled in the ice bath. The obtained mixture was stirred constantly at room temperature for a period of twenty-four hours. Following the completion of this procedure, decante was given an additional 500 mL of water that had been distilled. The process of washing with distilled water is repeated until the pH of the washing water reaches to 7.0 value. At last, it is dried in an incubator at a temperature of 90 degree. After measuring out a particular quantity of graphene oxide, it is then subjected to a treatment with N,N-dimethyl formamide (DMF). As a consequence of this, a suspense combination with a dark color is produced.

2.2.6 Preparation of MnO_2/h-MoO_3 Nanocomposite

The preparation of the nanocomposites involved a chemical precipitation process. The reaction process was given as follow steps: A 10.0 mL of pure water was used to dissolve a 1.23 g amount of ammonia heptamolybdate tetrahydrate (AHM), and 2.5 mL of concentrated HNO_3 were added dropwise to the mixture. A precipitation was observed after addition 0.5 mL HNO_3 resulting in the solution becoming colorless. An suitable quantity of MnO_2 was added to the aforementioned mixture-after 15 minutes of stirring. Stirring was then maintained for an additional 10 minutes, followed by 1 hour at 120 °C in an oil bath. The mixture was separated by centrifugation and then rinsed with water and ethanol after cooling to room temperature. Finally, the product was dried in a oven for 9 hours at 70 °C. The prepared materials are identified as MnO_2:MoO_3 (1:1), MnO_2:MoO_3 (2:1), MnO_2:MoO_3 (3:1), and MnO_2:MoO_3 (4:1), respectively. The composites were prepared in various weight ratios of -MnO_2/h-MoO_3 (1:1, 2:1, 3:1, and 4:1) (Shafi, 2017)

2.2.7 Synthesis of Nickel Molybdate ($NiMoO_4$)

2.90 g amount of $Ni(NO_3)_2.6H_2O$ and 0.50 g Na_2MoO_4 were added in 20 mL pure waster while continuous stirring to form a homogeneous solution for the usual synthesis of $NiMoO_4$. The precursor solution's pH was kept constant about 8.0 by aqueous ammonia solution. The resulting mixture was autoclaved for 2 hours at 180 °C. The sample was collected after it had cooled naturally and centrifuged several times. The solide part grinding in an agate mortar and then the finished product was dried in an oven at 60 °C for further characterization (Senthilkumar and Selvan, 2014) (Fig. 2.1).

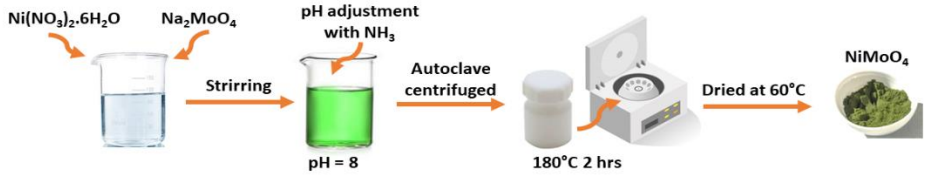

Figure 2.1 Synthesis of $NiMoO_4$

2.2.8 Synthesis of Nickel Vanadate ($Ni_3V_2O_8$)

$Ni_3V_2O_8$ particles were synthesized using the co-precipitation method. Firstly, 6.0 mmol L^{-1} V_2O_5 was dissolved in 10.0 mL of water and 30 mL of boiled 0.036 M NaOH was added. A color change from yellow to colorless was observed in the reaction mixture. Then 1.0 mL of concentrated HNO_3 was added until the pH of the mixture was 8.0 and stirred until a homogeneous suspension was obtained (solution 1). On the other hand, 6.0 mmol L^{-1} $NiCl_2.6H_2O$ was dissolved in 10.0 mL of water in another beaker and stirred for 5 minutes (solution 2). Finally, solution 2 was slowly added to solution 1 and mixed. After the mixture was stirred continuously for 3 hours, the resulting precipitate was collected. After filtration, it was washed several times with ethanol and water to remove impurities (Liu et.al, 2014).

2.2.9 Preparation of Ce/Zr Binary Oxide Nanoparticles

Ce/Zr binary oxide nanoparticles were prepared using the solvothermal method. First, 0.8 mmol L^{-1} moles (0.3473 g) of $Ce(NO_3)_36H_2O$ and 1.2 mmol L^{-1} moles of $ZrOCl_28H_2O$ (0.3867 g) were dissolved in 40.0 mL of CH_3CH_2OH to

obtain a mixture of cerium nitrate and zirconium oxychloride solution. 0.32 g of NaOH is dissolved in 40.0 mL of ethanol and added to the mixture of zirconium oxychloride and cerium nitrate to oxidize. The solution color changes from brown to yellow when the Ce^{3+} ion was completely oxidized to Ce^{4+}. The mixture was mixed for 10 minutes and taken into a 100 mL Teflon-lined autoclave. The mixture maintained at 180 ºC for 5 hours. The precipitate was then filtered and washed and dried at 80 °C. (Su et.al, 2015)

2.2.10 Preparation of real samples

In order to investigate the pharmaceutical sample application of the developed modified electrode, two rutin tablets were weighed and powdered in an agate mortar and dissolved in ethanol. The suspention was separated by filtration. After the residue was washed with ethanol, the clear filtered solution was diluted with ethanol to a volume of 100 mL.

To prepare a Parol film table solution, ten tablets were accurately weighed and then was powdered using an agate mortar and dissolved in pH 6.60 phosphate buffer solution (PBS). After separating the suspension using filtering, the clear solution was collected in a volumetric flask and then diluted to the desired volume using pH 6.60 PBS.

The synthetic urine sample was prepared in a 25 mL volumetric flask by addition of the following reagents: A 0.04 g amounth of KCl, 0.07 g amounth of NaCl, 0.04 g amounth of KH_2PO_4, 0.03 g amounth of $CaCl_2$, 0.025 g amounth of NH_4Cl, and 0.6 g amount of urea. The remaining flask volume was completed with ultra-pure water (Norbert, 2001; Wong, 2017).

3. RESULT AND DISCUSSION

3.1 Voltammetric Determination of Rutin

3.1.1 Preparation of poly (phenosafranine) film modified GCE

Electrochemical polymerization of 0.1 mmol L^{-1} phenosafranine monomer on GCE surface was performed in 0.05 mol L^{-1} H_2SO_4 solution in the potential range between -0.8 V to 1.8 V vs. Ag / AgCl (sat. KCl) at a scan rate of 0.05 V s^{-1} for 5 cycles (Fig. 3.1). The obtained CVs have shown a good agreement with previous work (Komura, 2000). During the phenosafranine electrochemical polymerization, two irreversible oxidation peaks were appeared at 1.100 V and 1.500 V without the corresponding cathodic processes for this peaks in the reverse scan. The height of both anodic peaks decraesed depending on current potential scan number. It is thought to be related to the oxidation of $-NH_2$ groups present in PSF (possibly to cation radicals (Gao et al. 2003), which indicates that $-NH_2$ groups participate in the polymerization as in other aromatic compounds containing $-NH_2$ groups (Oksaha et al. 1991; Saleh et al. 2011). Morever, a reduction peak at -0.400 V and a pair of redox peaks of the monomer were observed at about +0.100 V and 0.0 V, respectively. The peaks at +0.100 V and 0.0 V demostrates corresponds to the reversible two electron oxidation and reduction of the monomer 5-hydro-phenazine species could be formed during the reduction reaction.

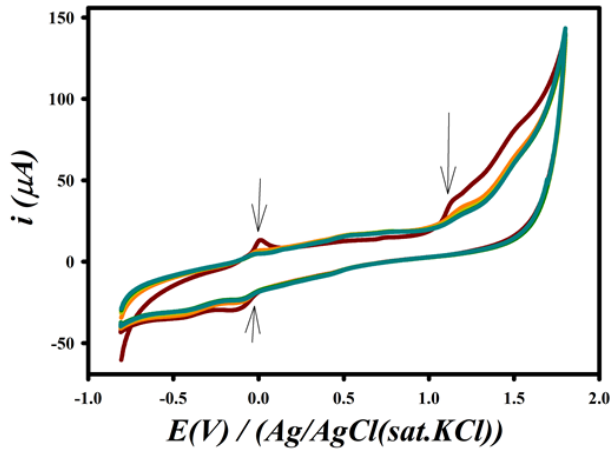

Figure 3.1 CVs for electrochemical polymerization for 0.1 mM phenosafranine in 0.05 mol L^{-1} H_2SO_4 on bare GCE at 0.05 V s^{-1} scan rate with 5 cycles

As the cycling number increased, it was clear that electropolymerization was performed on the GCE surface, as confirmed by an increase in the oxidation current. The presence of polymer on the GCE surface (as proved–by the electrode characterization) was also supported by SEM images and XPS data.

3.1.2 Preparation of MWCNT Modified PPSF/GCE

A 10 µL of MWCNT suspension was dropped on the poly(phenosafranine)-modified GCE surface. To remove the DMF from the GCE surface, the electrode was kept at 60 °C for over an hour.

3.1.3 Preparation of various metal nanoparticles modified MWCNT/GCE

The unique features of metal nanoparticles, which are distinct from their bulk forms and can improve electron transport rate and catalyze a process, led to their widespread use as an electrode material. The more catalytic electrode surfaces toward analytes were achieved by using metal nanoparticles as part of a composite electrode material, which was used extensively in this thesis.

The electrochemical deposition of gold, copper, and cobalt metal/ or metal oxide nanoparticles on MWCNT/PPSF/GC electrode surfaces were carried out in their acidic solutions by consecutive currrent potential scan with CV (Fig. 3.2).

Additionaly, a chronoamperometric technique was used to Ni/NiO particles on MWCNT/PPSF/GCE.

In Fig. 3.2A, the repitetive cyclic voltammograms of MWCNT/PPSF were acquired in the presence 1.0 mmol L^{-1} $HAuCl_4$ containing 0.1 mol L^{-1} HCl in potential range between 0.9 V to -0.9 V at a scan rate of 50 mV s^{-1}. Two reduction peaks were appeared at -0.05 V and -0.45 V which corresponds to the reduction of Au^{3+} during the potential cycles for cathodic way. An anodic peak was observed at 0.30V for Au metal particles re-oxidation.

The process of electrochemically deposition of Cu metal nanoparticles onto the surface of MWCNT/PPPSF/GCE was carried out by CV in the potential range from -1.20 V to +0.50 V in the presence of 1.0 mmol L^{-1} $CuSO_4$ + 0.1 mol L^{-1} H_2SO_4 (Fig. 3.2 B). This deposition process was repeated by five consecutive current potential scan. with 50 mV s^{-1} scan rate. In the case of first current potential scan, the main reduction and oxidation peaks were observed at -0.78 V and -0.52 V respevtively due to Cu^{2+} ions reduction to Cu and reoxidation of Cu metal particles oxidation. In the second and repitetive scans, another Cu^{2+} reduction peak was appeared at -0.25 V due to the formation of Cu metal particles containing layer on the MWCNT/PPPSF/GCE with first current potential scan.

Co_3O_4 particles were deposited on MWCNT/PPSF/GCE from 3.0 mmol L^{-1} $CoCl_2$ containing 0.1 mol L^{-1} NH_4Cl with in potential range between 1.0 V to -1.50 V by CV at a scan rate of 50 mV s^{-1}(Fig. 3.2 C). A small reduction peak was formed at about -0.85 V related with Co^{2+} reduction and three oxidation peaks -0.55 V, 0.0V and 0.70 V were observed due to the formation of both Co(II) and Co(III) species. The increase in all oxidation peak currents shows the growing the amount of Co_3O_4 on the MWCNT/PPSF/GCE.

Fig. 3.2 D indicates the chronoamperometric deposition of Ni/NiO nanoparticles on the MWCNT/PPSF/GCE surface at -1.30 V constant potential for 60 s in presence of 1.0 mmol L^{-1} $NiSO_4$ + 0.1 mol L^{-1} H_2SO_4.

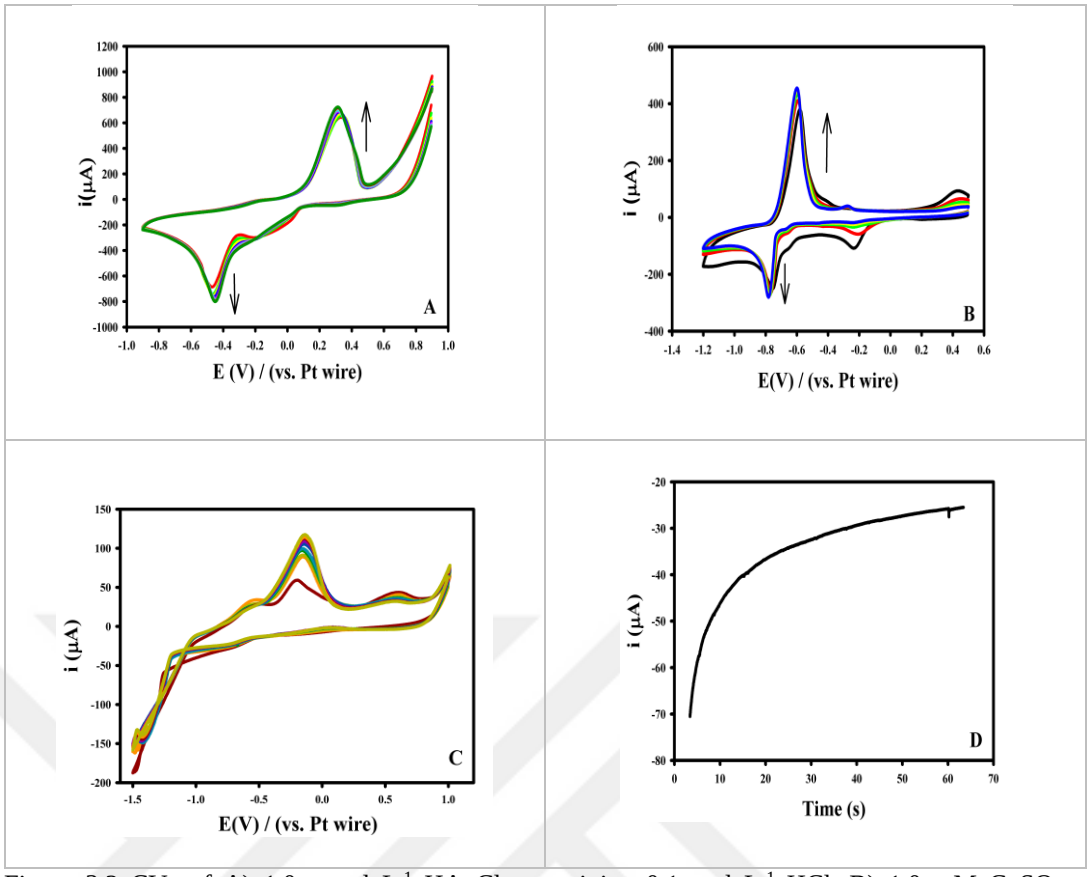

Figure 3.2 CVs of A) 1.0 mmol L^{-1} $HAuCl_4$ containing 0.1 mol L^{-1} HCl, B) 1.0 mM $CuSO_4$ containing 0.1 M H_2SO_4 and C) 3.0 mM $CoCl_2$ containing 0.1 mol L^{-1} NH_4Cl deposition on MWCNT/PPSF/GCE

3.1.4 Surface Characterization of Modified Electrodes

Techniques for surface characterization were important tools for understanding the morphology and demonstrating the presence of prepared modifiers on electrode surface. In this respect, bare GCE and modified electrodes surfaces were investigated using SEM, EDX, EIS and XPS tecniques. Fig. 3.3 indicates the SEM images of PPSF/GCE (A), MWCNT/PPSF/GCE (B) and Co_3O_4/MWCNT/PPSF/GCE (C) respectively. As could be seen in Fig. 3.3 A, a numerous non-uniform particles of PPSF were formed at GCE surface. It demostrated completely different image when compared with the MWCNT/PPSF/GCE (B) and Co_3O_4/MWCNT/PPSF/GCE (C), indicating the successful electrodeposition of PPSF on GCE. When the polymer surface is incorporated by dropping the MWCNT (Fig. 3.3 B), a composite structure is obtained, so that the polymer component is ostensible in the depths of the tubular MWCNT coated surface. In the SEM images of the Co_3O_4/MWCNT/PPSF/GCE, some Co_3O_4 nanoparticles as almost nanocubes shape that produced into small sizes (mean diameter of 189 nm) and irregular forms grow on the MWCNT/PPSF/GCE can be seen clearly with different magnitude in Fig. 3.3 C and D. In the existance of the carboxyl functional groups on MWCNTs facilitates ionically bonded to metal ions or covalently coupled through various metal oxides (Chu, 2010); (Al-Kadhi, 2022). To confirm the composition of Co_3O_4/MWCNT/PPSF/GCE, the EDX elemental analyses were showed the existance of Co, C and O atoms on the composite structure.

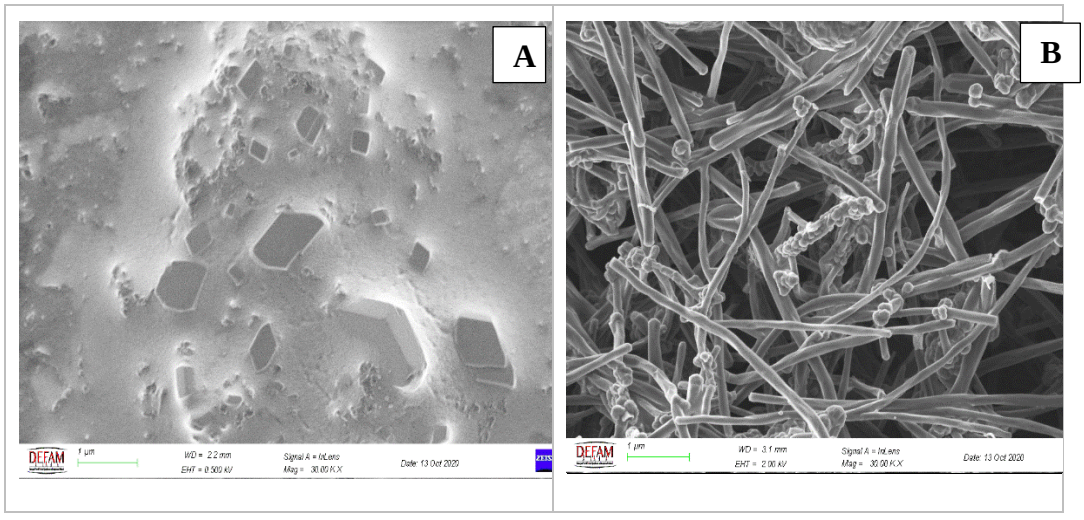

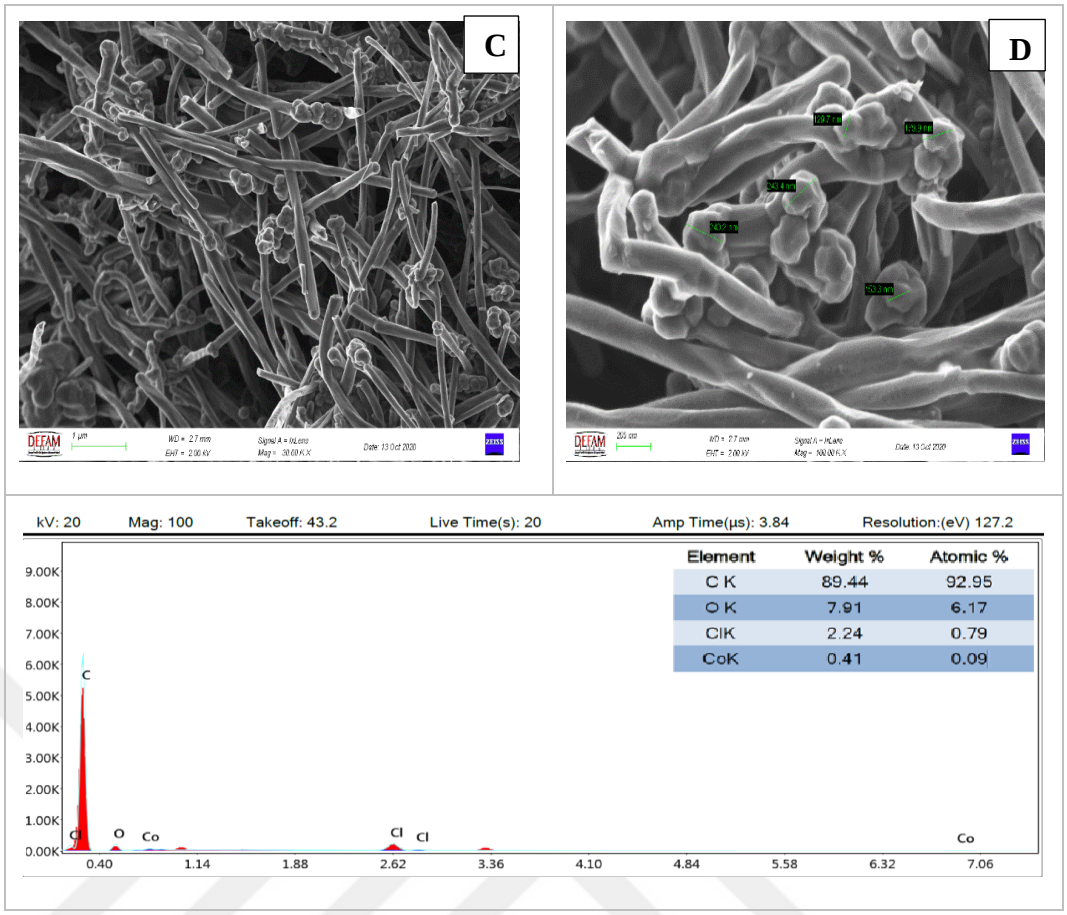

Figure 3.3 Scanning electron micrographs of (A) PPSF/GCE, (B) MWCNT/PPSF/GCE, (C) Co_3O_4/MWCNT/PPSF/GCE with 30000 magnitude (D) Co_3O4/MWCNT/PPSF/GCE with 50000 magnitude.

The voltammetric behaviour of GCE, PPSF/GCE, MWCNT/PPSF/GCE and Co_3O_4/MWCNT/PPSF/GCE were examined with CV in the 0.1 mol L^{-1} KCl + 5.0 mmol L^{-1} $K_3[Fe(CN)_6]/K_4[Fe(CN)_6]$ solution at scan rate of 0.05 V s^{-1}. A pair of redox peaks were appeared for each electrode (Fig. 3.4 A). The difference of the peak potential; ΔEp (Epa-Epc) were 213, 215, 186 and 217 mV at bare GCE, PPSF/GCE, MWCNT/PPSF/GCE and Co_3O_4/MWCNT/PPSF/GCE, respectively. The maximum peak current was obtained at Co_3O_4/MWCNT/PPSF/GCE due to the its most electroactive surface area when compared the other electrodes. The Randles-Sevcik equation (eq.1) was used to calculate the electroactive surface areas (EASA) for all electrodes with data obatinated into 1.0 mmol L^{-1} $K_3[Fe(CN)_6]/K_4[Fe(CN)_6]$ in 0.1 mol L^{-1} KCl solution (Song et al., 2010).

$$Ip= (2.69\ 10^5)\ n^{3/2}\ A\ D^{1/2}\ C\ v^{1/2} \quad \text{..... (eq.1)}$$

n is the number of electrons transferred, A is the electroactive surface area (cm^2), D is the diffusion coefficient ($cm^2\ s^{-1}$), C is the concentration of concentration of

$K_4Fe(CN)_6$ (mol cm^{-3}), and v is the scan rate value (V s^{-1}). The EASA of the electrodes was calculated from the slope of Ip vs $v^{1/2}$ plot since D (6.7×10^{-6} cm^2 s^{-1} at 25 °C) , n (n = 1) and C (1.0 mmol L^{-1}) are known values. The EASA values were 0.086, 0.100, 0.287 and 0.431 cm^2 for the bare GCE, PPSF/GCE, MWCNT/PPSF/GCE and Co_3O_4/MWCNT/PPSF/GCE, respectively. These data indicate a considerable improving the surface properties of MWCNT/PPSF/GCE after the deposition of Co_3O_4 species.

To investigate the electron transfer rate of the developed electrodes, EIS behaviour of bare GCE, PPSF/GCE, MWCNT/PPSF/GCE and Co_3O_4/MWCNT/PPSF/GCE were tested (Fig. 3.4 B) in 5.0 mmol L^{-1} $K_3[Fe(CN)_6]/K_4[Fe(CN)_6]$ in 0.1 mol L^{-1} KCl solution at the frequencies range 0.05 to 75,000 Hz and 0.05 V of amplitude. The Rs (Cdl(RctW)) equivalent circuit was used fitting the EIS data; circuit charge transfer resistance (Rct), electrolyte resistance (Rs), Warburg impedance (W) and the double layer capacitance (Cdl). It was obviously seen in Fig. 3.4 B that GCE shows a large electron transfer resistance of about 576 ohm. The lowest Rct value (72.4 Ω) for the Co_3O_4/MWCNT/PPSF/GCE reflects a relatively fast charge transfer taking place compared with the MWCNT/PPSF/GCE (269 Ω), PPSF/GCE (328 Ω) and bare GCE (576 Ω). These results show that the existence of PPSF, MWCNT and Co_3O_4 on composite structure was improved the charge transfer between probe and electrode. Therefore the highest charge transfer rate and the smallest electron transfer resistance was obtained at the Co_3O_4/MWCNT/PPSF GCE.

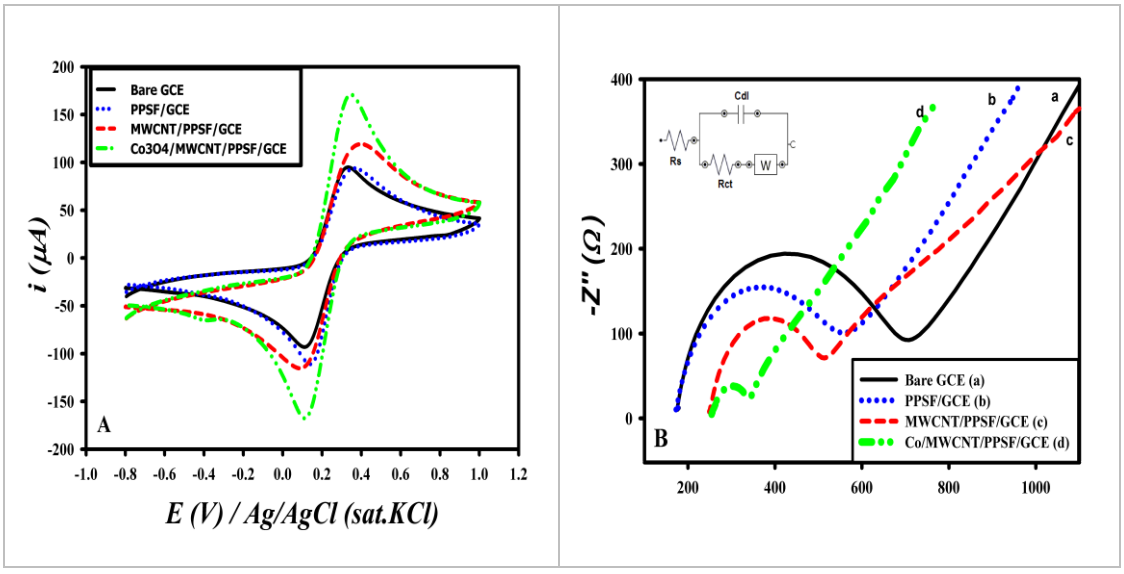

Figure 3.4 A) CVs of bare and modified GCEs in 0.1 mol L^{-1} KCl solution + 5.0 mmol L^{-1} $K_3[Fe(CN)_6]/K_4[Fe(CN)_6]$ at 50 mV s^{-1}. scan rate. (B) the bare and modified electrodes Nyquist plots.

XPS studies were performed to idenfy the surface composition of Co_3O_4/MWCNT/PPSF/GC electrode and the oxidation state of Co atoms (Fig. 3.5).

The survey spectrum of the Co_3O_4/MWCNT/PPSF indicate the presence C, O and Co on the composite electrode (Fig. 3.5 A). Fig. 3.5 B C1s spectrum which showed that the main peak at a binding energy of 284.4 eV could be deconvoluted into three characteristic peaks corresponding to C-C (284.4 eV, peak 1), C-C (285.1 eV, peak 2), (C-O/ C-N) (285.9 eV, peak 3), O-C-O (286.5 eV, peak 4), C-NHx/C-O (287.5 eV, peak 5) groups. The N1 spectrum confirmed the MWCNT and polymer in the composite structure. In similarly, the XPS spectrum of the N1s electrons (Fig. 3.5 C) showed that the main peak may be deconvoluted into three peaks at binding energies (BE) 401.37 eV (peak 1) and 402.35 eV (peak 2) and 402.85 eV (peak 3) ascribed to the imine (–N=), amine (–NH–) and positively charged nitrogen groups (N^+) formed species, respectively (Abdulla et al., 2015). It is likely that the PPS contains -NH- linked fenosafranin units. As the polymerization progresses, the amine groups become nitrogen bridges and these bridges become electroactive similar within polyaniline (Komura et al., 2000) The O 1s XPS spectrum of Co_3O_4/MWCNT/PPSF/ GC electrode was shown in Fig. 3.5 D. It showed three peaks and the first at 531.3 eV specify to lattice oxygen (O1), 532.6 eV specified to the adsorbed oxygen species on to the surface vacancy (O2) and 533.5 eV specified to the adsorbed hydrated species on the surface (O3). Fig. 3.5 E demostrate the XPS spectrum of the Co 2p electrons in Co_3O_4/MWCNT/PPSF composite. Two core-level signals were consisted: the first peak was located about 781.7 eV corresponded to the Co $2p_{3/2}$ electrons and the second peak located at 797.1 eV corresponded to the $Co2p_{1/2}$ electrons. On the other hand, two satellite peaks were appeared at 787.3 eV and 803.7 eV. The Co 2p core level spectrum indicates the existence of two different cobalt species as Co^{2+} and Co^{3+} (Fig. 3.5 D). Especially, the binding energies of 781.7 eV and 797.1 eV in the spectrum represent $2p_{3/2}$ and $2p_{1/2}$, respectively, for Co^{2+}; while the binding energies of 788.2 and 803.6 show $2p_{3/2}$ and $2p_{1/2}$, respectively, for Co^{3+} (Xia et al., 2013; Yan et al., 2012; Li et al., 2009). In addition, the Co $2p_{3/2}$ peak heigth was meaningful higher than the Co $2p_{1/2}$ peak heigth, it can be also concluted that Co mainly consisted of both Co^{2+} and

Co^{3+} in Co_3O_4/MWCNT/PPSF. Also another data calculated as 15.4 eV from two main peaks bindig energies (781.7 and 797.1 eV) separation correspond to the spin-orbit doublet of the Co 2p (Menezes et al., 2015; Huang et al., 2012).

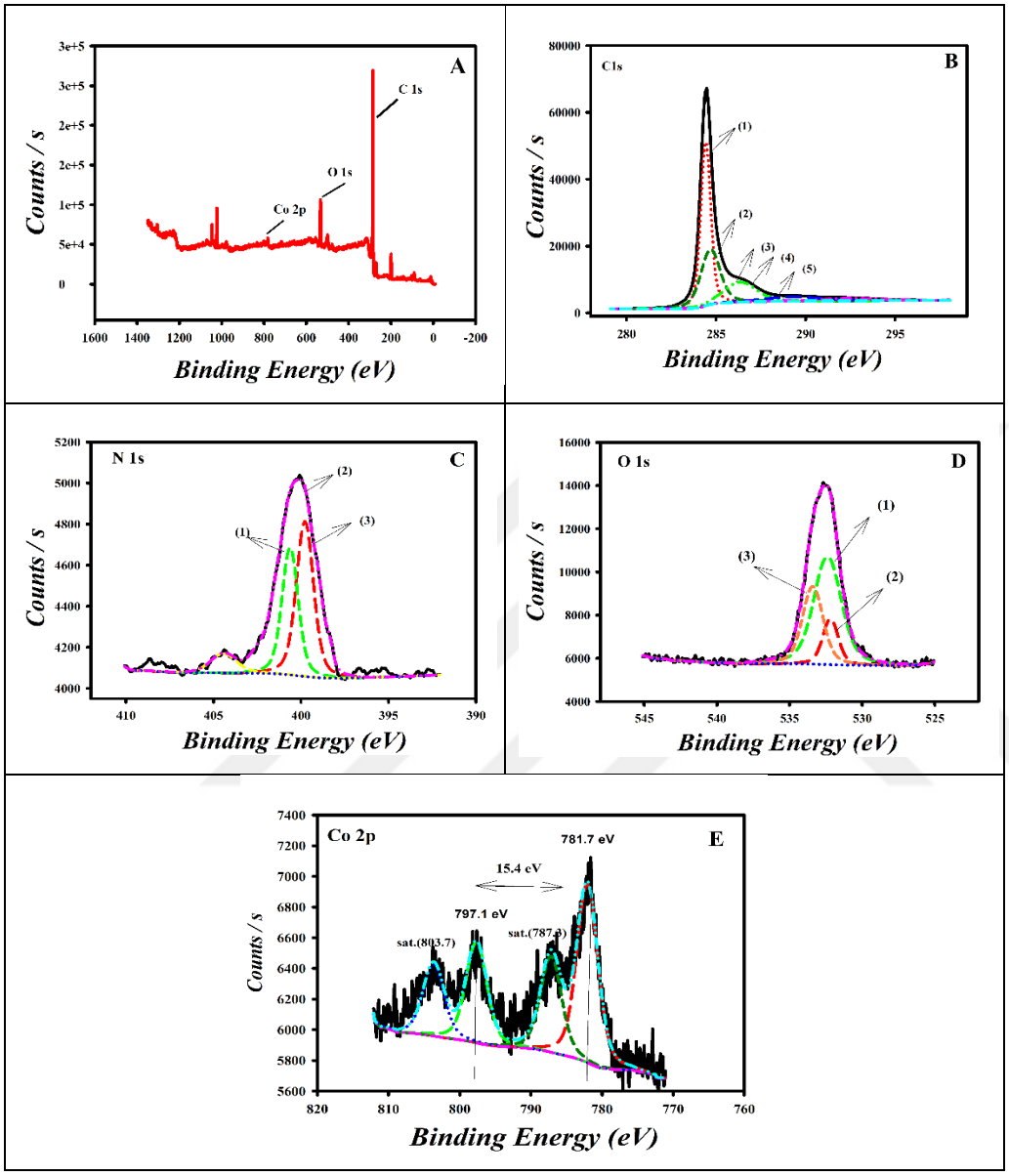

Figure 3.5 XPS spectrums A) survey B) core level C 1s C) N1s, D) O 1s E) Co 2p spectra of Co_3O_4/MWCNT/PPSF modified GCE.

3.1.5 Electrochemical Behaviour of Rutin at Bare and Modified GC Electrodes

The electrochemical behavior of bare GCE and various metal nanoparticles (Co, Cu, Ni, Au, Au and Cu) modified MWCNT-polymer composite electrodes were studied in the absence and presence of 10.0 μmol L^{-1} rutin in pH 3.0 BR buffer

solution by CV in potential range from - 0.40 V to 1.20 V with 50 mVs^{-1} scan rate (Fig. 3.6).

The CVs of all electrodes in pH 3.0 BR buffer solution were demonstrated in Fig. 3.6 A that no oxdidation and reduction peaks except Au-Cu and Au modified MWCNT-polymer composite electrodes. As shown in Fig. 3.6 B, a quasi-reversible electrochemical behavior was observed for at bare and various metal nanoparticles (Co, Cu, Ni, Au, Au and Cu) modified MWCNT-polymer composite electrodes (except the PPSF/GCE), verfying the electrochemical oxidation and reduction reactions of rutin were consisted on almost all electrodes (except the PPSF/GCE). The peak potential and peak current of rutin on all electrodes (except the PPSF/GCE) were given in Table 3.1.

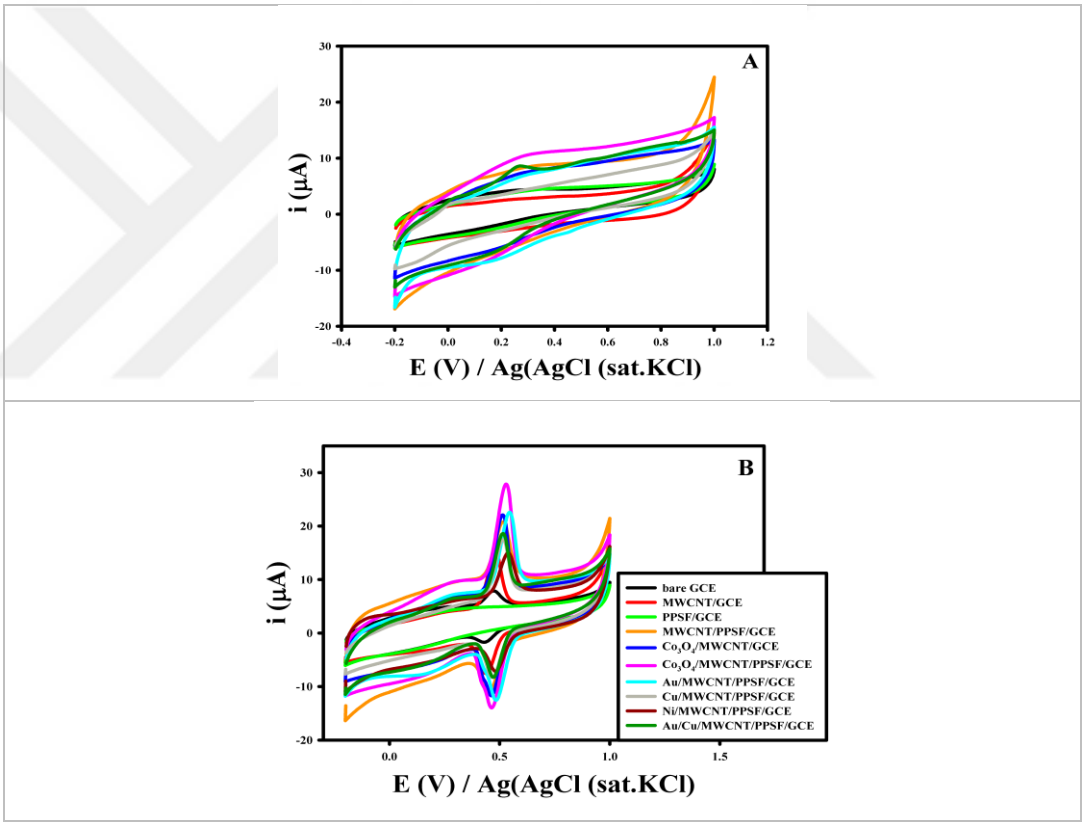

Figure 3.6 CV plots A) absence B) presence of 10.0 µM rutin oxidation in pH 3.0 BRbuffer solution at bare GCE and metal nanoparticle modified electrodes.

From the voltammograms in Fig. 3.7; it was observed that while the oxidation and reduction peak currents related to the rutin increase at all modified electrodes, the peak potentials also slightly were shifted to positive potentials. On the other hand, the highest peak current was obtained at Co_3O_4/MWCNT/PPSF/GC electrode. The peak currents and peak potentials for 10.0 µmol L^{-1} rutin were summarized in Table

3.1. Therefore Co_3O_4/MWCNT/PPSF/GCE was choosen as optimum working electrode for future studies.

Table 3.1 The peak rutin oxidation values at bare and modified electrodes.

Electrode	i_a(µA)	E_a(V)	i_c(µA)	E_c(V)
Bare GCE	2.53	0.470	-1.799	0.435
PPSF/GCE	-	-	-	-
MWCNT/GCE	9.99	0.482	-6.75	0.441
Co_3O_4/MWCNT/GCE	14.17	0.514	-15.85	0.449
Co_3O_4/MWCNT/PPSF/GCE	**17.31**	**0.529**	**-12.20**	**0.464**
Au/MWCNT/PPSF/GCE	13.84	0.546	-10.31	0.484
Cu/MWCNT/PPSF/GCE	10.58	0.516	-7.58	0.468
Ni/MWCNT/PPSF/GCE	7.68	0.538	-5.67	0.484
Cu/Au/MWCNT/PPSF/GCE	8.71	0.528	-6.49	0.479
Au/Cu/MWCNT/PPSF/GCE	10.58	0.514	-7.75	0.472

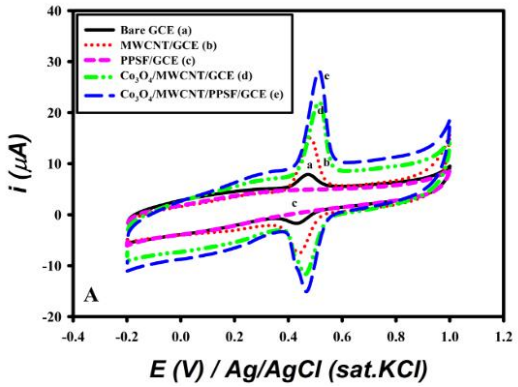

Figure 3.7 CVs for bare and modified electrodes in the presence of 10.0 µmol L^{-1} rutin pH 3.0 BR.

<u>Optimization of poly(phenosafranine) concentration for preparation of Co_3O_4/MWCNT/PPSF/GCE by monitoring the rutin electrochemical response</u>

The effect of phenosafranine monomer concentration in the range from 0.05 mmol L^{-1} - 1.00 mmol L^{-1} to prepare the polyphenosafranine component in Co_3O_4/MWCNT/PPSF/GCE was also optimized by monitoring the rutin electrochemical response in pH 3.0 BR buffer solution. Fig. 3.8 shows the current and potential variation of rutin oxidationmand reduction peaks depending on phenosafranine monomer concentration. The highest peak currents for both

oxidation and reduction of rutin were obtained at Co_3O_4/MWCNT/PPSF/GCE which was prepared in the presence of 0.1 mmol L^{-1} phenosafranine concentration (Fig. 3.9 and Table 3.2). Therefore the optimum monomer concentration for future studies was prepared as 0.1 mmol L^{-1} of phenosafranine.

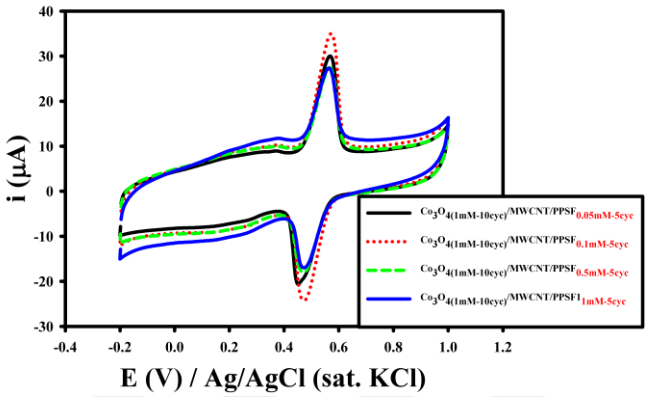

Figure 3.8 CVs of Co_3O_4//MWCNT/PPSF/GCE which prepared various monomer concentration presence of 10.0 µmol L^{-1} rutin in pH 3.0 BR, with scan rate was 50 mV s^{-1}

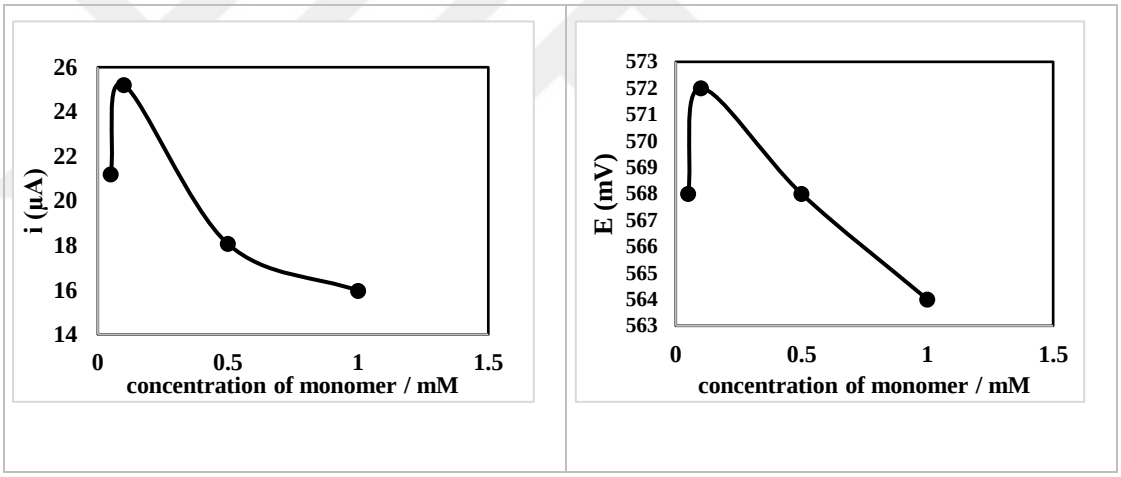

Figure 3.9 A) Peak current vs. phenosafranine concentration and B) Peak potential vs. phenosafranine concentration for rutin oxidation at 10 mM on Co_3O_4/MWCNT/PPSF/GCE.

Table 3.2 The influence of PSF monomer concentration on the electrochemical behavior of rutin

Concentration of monomer (mM)	**i_{pa} (µA)**	**E_{pa} (V)**	**i_{pc} (µA)**	**E_{pc} (V)**
0.05	21.18	0.568	17.34	0.453
0.1	**25.19**	**0.572**	**20.84**	**0.474**
0.5	18.06	0.568	14.59	0.472
1	15.96	0.564	12.84	0.476

Effect of polymerization cycle number on rutin response at Co_3O_4 modified MWCNT/PPSF/GCE

To investigate of polymerization cycle number effect on 10.0 μmol L^{-1} rutin electrochemical response in pH 3.0 BR buffer solution, the PPSF constituent in Co_3O_4/MWCNT/PPSF/GCE was formed with different cycle number (3,5,7 and 10 cycle) by CV. Fig. 3.10 demonstrated to phenosafranine monomer electrochemical polymerization cycle number on the response of 10.0 μmol L^{-1} rutin in pH 3.0 BR buffer solution. Fig. 3.10-inset shows the electrochemical behavior of Co_3O_4 (10 cycles)/MWCNT/PPSF/GC electrodes which prepared with various electrochemical polymerization cycle number of phenosafranine in pH 3.0 BR buffer solution. In Fig. 3.10, a quasi reversible electrochemical behaviour of rutin was obtained at all Co_3O_4 (10 cycles)/MWCNT/PPSF/GCE electrodes which prepared with various cycle number of phenosafranine.

Although the oxidation and reduction peak potentials of the rutin were almost constant as 0.52 V and 0.48 V, the peak currents varied as the number of cycles changed, and the highest peak currents were obtained by 5 cycles of PPSF coating for both oxidation and reduction process.

In the evaluation of the electrochemical behaviour of rutin, the oxidation peak properties were considered. Fig. 3.11A-B shows the effect of polymerization cycle number on the oxidation behavior of rutin in pH 3.0 BR buffer solution. The peak currents change with polymerization cycle number. Among the all modified electrodes, the maximum peak current was obtained for 10.0 μmol L^{-1} rutin at Co_3O_4 (10 cycles)/MWCNT/PPSF/GCE which was prepared after 5 cycle polymerization process. Therefore, 5 cycles number was chosen for phenosafranine electropolymerization process.

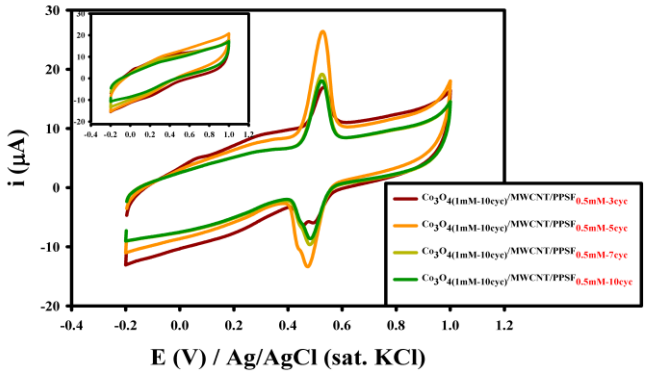

Figure 3.10 CVs of Co_3O_4//MWCNT/PPSF/GCE which prepared various monomer cycle number presence of 10.0 µmol L^{-1} rutin in pH 3.0 BR, with scan rate was 50 mV s^{-1} (inset: absence of rutin)

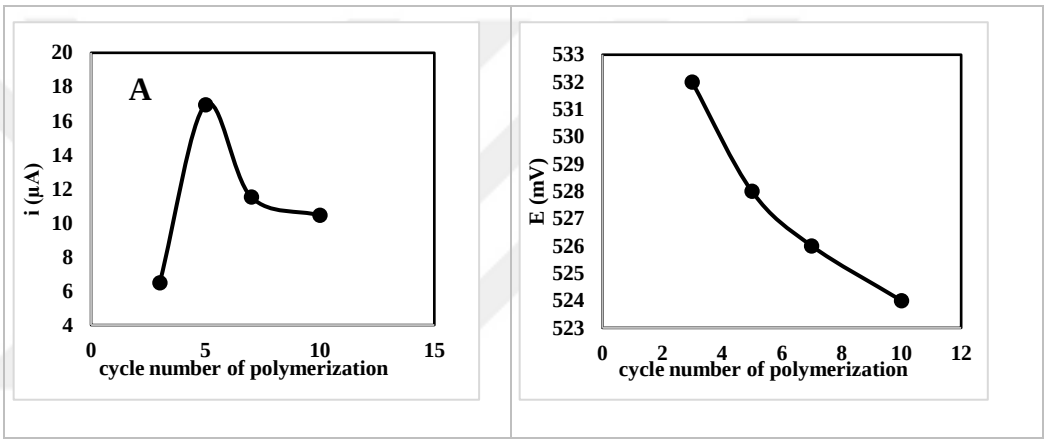

Figure 3.11 Plots for the effect of phenosafranine polymerization cycle number on A) i_{rutin} and B) E_{rutin} at Co_3O_4/MWCNT/PPSF/GCE.

Table 3.3 The effect of PSF cycle number on electrochemical behaviour of rutin

Cycle number	i_{pa} (µA)	E_{pa} (V)	i_{pc} (µA)	E_{pc} (V)
3	6.48	0.532	4.12	0.474
5	**16.95**	**0.528**	**12.43**	**0.443**
7	11.52	0.526	8.70	0.480
10	10.45	0.524	10.69	0.453

Optimization of NH_4Cl concentration for preparation of Co_3O_4 ***component at*** Co_3O_4/MWCNT/PPSF/GCE.

The $CoCl_2$ solution was prepared in different concentration of aqueous NH_4Cl solution in the range 0.025 $molL^{-1}$ – 0.1 $molL^{-1}$. The effect of NH_4Cl concentration during Co_3O_4 ***component formation on the*** MWCNT/PPSF/GCE was studied by

CV while monitoring the electrochemical response of 10.0 µmol L^{-1} rutin (Fig. 3.12). The highest oxidation and reduction peak currents were obtained at Co_3O_4/MWCNT/PPSF/GCE which Co_3O_4 componenet deposited in the presence of 0.025 mol L^{-1} aqueous NH_4Cl 1.0 mmol L^{-1} $CoCl_2$ solution.

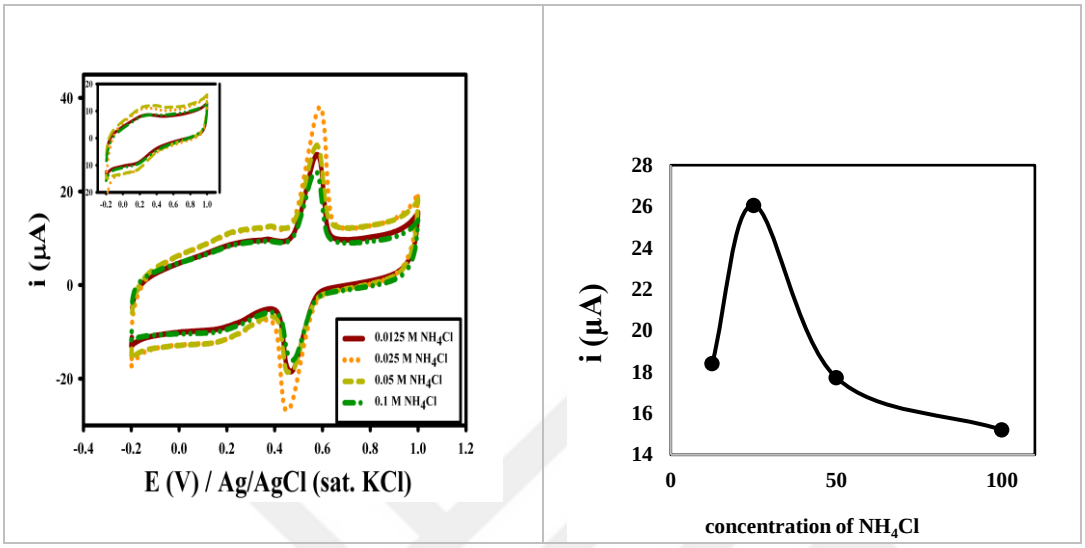

Figure 3.12 CVs of Co_3O_4//MWCNT/PPSF/GCE which prepared various NH_4Cl concentration presence of 10 µmol L^{-1} rutin in pH 3.0 BR, with scan rate was 50 mV s^{-1} (inset: absence of rutin)

Optimization of $CoCl_2$ concentration for preparation of Co_3O_4 nanoparticles on MWCNT/PPSF/GCE

To increase the electrochemical activity of the composite electrodes, the metal oxide content is significant. By altering the concentration of the metal ion solution and the number of cycles, the electrochemical method offers a chance to manage the formation of nanoparticles. In this respect, Co_3O_4 nanoparticles were deposited on MWCNT/PPSF/GCE in the presence of different $CoCl_2$ concentrations (0.1, 0.5, 1.0, 3.0, 5.0 mmol L^{-1}). The electrochemical behaviour of 10.0 µmol L^{-1} rutin was investigated on Co_3O_4/MWCNT/PPSF/GCE in which the Co_3O_4 component formed MWCNT/PPSF/GCE with different $CoCl_2$ concentrations (Fig. 3.13-3.14).

Table 3.4 have shown a comparison of the electrode responses to rutin oxidation, including the peak characteristics of the modified electrodes. Peak current value of rutin oxidation in pH 3.0 BR solution was first almost same currents were obtained for 0.1 and 0.5 mmol L^{-1} $CoCl_2$ solution. When used to more than 5.0 mmol L^{-1} $CoCl_2$ solution to prepare the Co_3O_4/MWCNT/PPSF/GCE, the peak currents of 10.0 µmol L^{-1} rutin was decreased. However, the highest peak currents were obtained at

Co_3O_4/MWCNT/PPSF/GCE which the Co_3O_4 component deposited in the presence of 0.025 mol L^{-1} aqueous NH_4Cl 5.0 mmol L^{-1} $CoCl_2$ solution, a stability issue encountered during the experimetal studies were performed as fall off the small pieces of Co_3O_4/MWCNTs componenets from suraface, due to the increase in the amount of Co_3O_4 that the surface cannot hold. Thus the concentration of $CoCl_2$ was selected 3.0 mmol L^{-1} for future studies.

This surface shows that the bulk structure is formed and that this bulk structure is heavy on the surface. Therefore, it is observed that the MWCNT on the surface is falling off the surface in small pieces. For this reason, 3.0 mmol L^{-1} as optimum concentration was selected and the studies were continued.

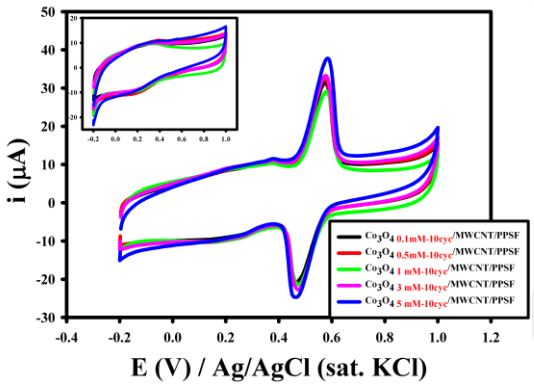

Figure 3.13 CVs of Co_3O_4//MWCNT/PPSF/GCE which prepared various $CoCl_2$ concentration presence of 10 µmol L^{-1} rutin in pH 3.0 BR, with scan rate was 50 mV s^{-1} (inset: absence of rutin)

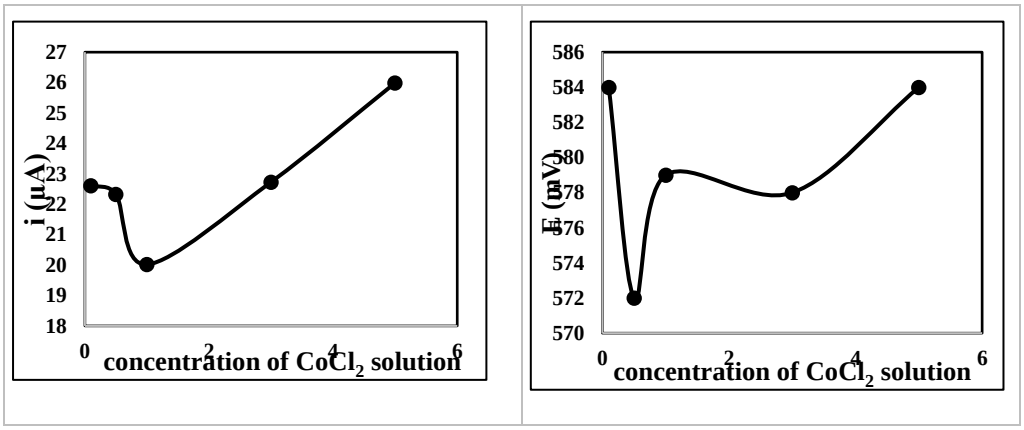

Figure 3.14 Plots for the effect of $CoCl_2$ concentration on A) peak current and B) peak potential of 10 µmol L^{-1} rutin oxidation at Co_3O_4/MWCNT/PPSF/GCE.

Table 3.4 The effect of $CoCl_2$ concentartion on electrochemical behaviour of rutin

c (mM)	I_a(µA)	E_a(V)	I_c(µA)	E_c(V)

0.1	22.61	0.584	19.29	0.461
0.5	22.33	0.572	17.09	0.480
1	20.02	0.579	16.45	0.476
3	22.73	0.578	18.72	0.476
5	25.99	0.584	21.27	0.468

Optimization of cycle number for preparation of Co_3O_4 nanoparticles on MWCNT/PPSF/GCE from $CoCl_2$ solution

The effect of cycle numbers (5, 10, 15, and 20) on Co_3O_4 nanoparticles formation at MWCNT/PPSF/GCE were studied with 3.0 $mmolL^{-1}$ $CoCl_2$ solution by monitoring the electrochemical behaviour of 10.0 µmol L^{-1} rutin in pH 3.0 BR buffer solution (Fig. 3.15). A quasi-reversible electrochemical behaviour was observed at Co_3O_4/MWCNT/PPSF/GCE which prepared by different cycle numbers at close oxidation and reduction potentials. The peak currents were incraesed until 10 cycle numbers deposition of Co_3O_4 and then decreased at more cycle numbers.

In a pH 3.0 BR solution, the higher electrochemical activity towards rutin was found by 10 cycles of Co_3O_4 deposition. The optimum electrode was choosen for further study as Co_3O_4(10cyc)/MWCNT/PPSF/GCE.

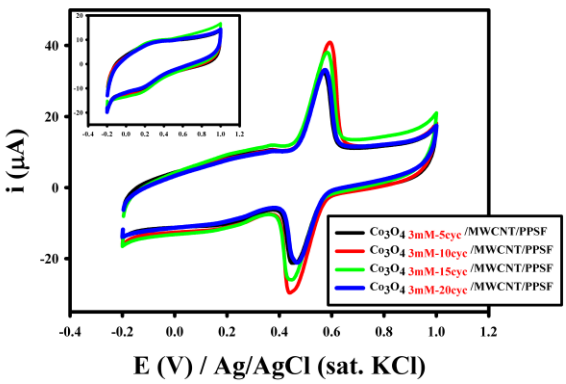

Figure 3.15 Cyclic voltamograms of Co_3O_4/MWCNT/PPSF/GCE which prepared 3.0 $mmolL^{-1}$ $CoCl_2$ various cycle number (5, 10, 15, 20) presence of 10 µmol L^{-1} rutin in pH 3.0 BR, with scan rate was 50 mV s^{-1} (inset: absence of rutin)

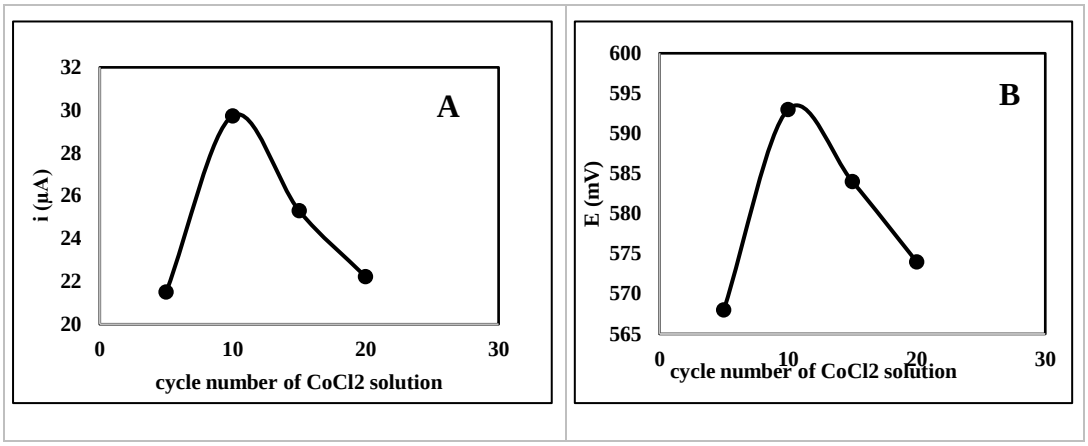

Figure 3.16 Plots for the effect of Co_3O_4 nanoparticles cycle number on A) peak current and B) peak potential of 10.0 µM rutin oxidation at Co_3O_4(10cyc)/MWCNT/PPSF/GCE.

Table 3.5 The effect of Co_3O_4 cycle number on electrochemical behaviour of rutin.

Cycle number	**i_a(µA)**	**E_a(V)**	**i_c(µA)**	**E_c(V)**
5 cycles	21.51	0.568	-16.79	0.461
10 cycles	**29.74**	**0.593**	**-23.84**	**0.441**
15 cycles	25.30	0.584	-20.55	0.449
20 cycles	22.22	0.574	-17.59	0.470

Effect of supporting electrolyte pH on rutin oxidation

The effect of supporting electrolyte pH on the electrochemical behaviour of 10 µmol L^{-1} rutin at Co_3O_4/MWCNT/PPSF/GCE was examined in the pH range from 2.25 to 7.00 BR buffer solution. As can be seen in Fig. 17 A, oxidation peak potential (E_{pa}) of rutin shifted toward negative values by increasing the pH value, indicating hydrogen ions were involved in the electrode reaction. Fig. 17 B. shows that a good linear relationship between E_{pa} and pH. The linear equation was E_{pa} = -0.0595 pH + 0.7089 (R^2 = 0.9944). A slop of -0.0595 mV pH^{-1} displayed the ratio of electrons and protons involves in the electrode reaction was 1:1. The higher peak currents was observed at pH 3.0. Thus, pH 3.0 was choosen for future studies.

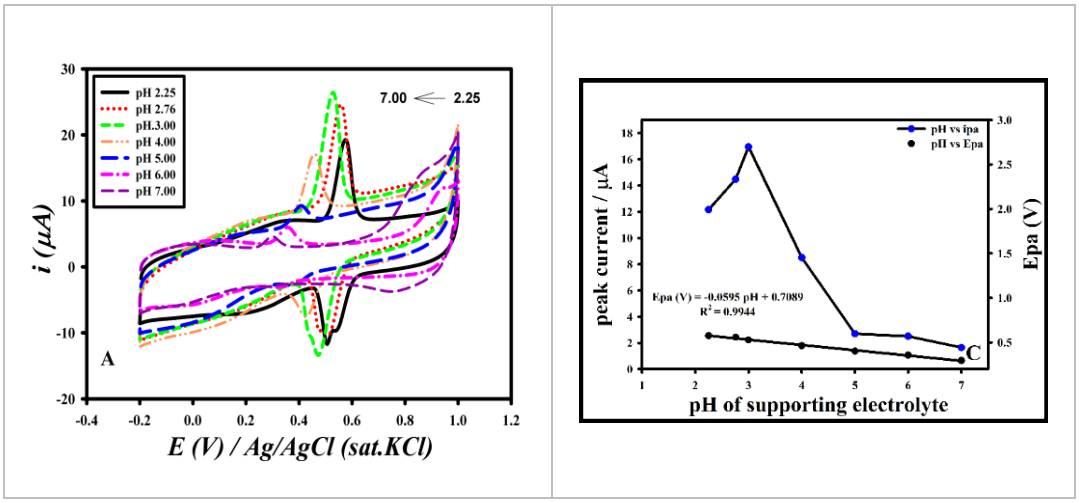

Figure 3.17 (A) CVs of 10 µmol L^{-1} RT at different pH values of BR buffer solution on Co_3O_4/MWCNT/PPSF/GCE; (B) The influence of pH on the peak characteristic of rutin.

Scan Rate Studies of Rutin at Co_3O_4/MWCNT/PPSF/GCE

The influence of scan rate on the oxidation and reduction of rutin at Co_3O_4/MWCNT/PPSF/GCE was investigated by CV at various scan rate in the range between 10 mV s^{-1} and 500 mV s^{-1} in pH 3.0 BR buffer solution (Fig. 3.18A). The oxidation and reduction peak currents (I_{pa} and I_{pc}) of 10 µmol L^{-1} rutin were increased linearly with the square root of scan rate ($v^{1/2}$) and the equations can be showed as Ip_a= 3.0892 $v^{1/2}$ – 9.6856 (R^2=0.9958) and Ip_c=−2.6901 $v^{1/2}$+ 9.762 (R^2=0.992) (Fig. 3.18B). Almost the same tendency, the linearity was also obtanined for log Ipa and log Ipc vs log ν (Fig. 3.18C). A linear change was acquired from the *log* I_{pa} and *log* I_{pc} vs log ν plots and the slopes were found as 0.8144 and 0.8320 (Figure 3.18C). Since the slope values were between 0.5 and 1.0, the electrochemical process could be both adsorption and diffusion-controlled electrode process.

As can be seen in Fig. 3.18D, the redox potential (E_{pa} and E_{pc}) also had a linear relationship with the *In v* and the regression equations being $E_{pa}(V)$ = 0.0751 *Inv (V/s)* + 0.2529 and $E_{pc}(V)$ = 0.0696 *Inv (V/s)* + 0.7584 with R^2 = 0.9874 and 0.9849, respectively.

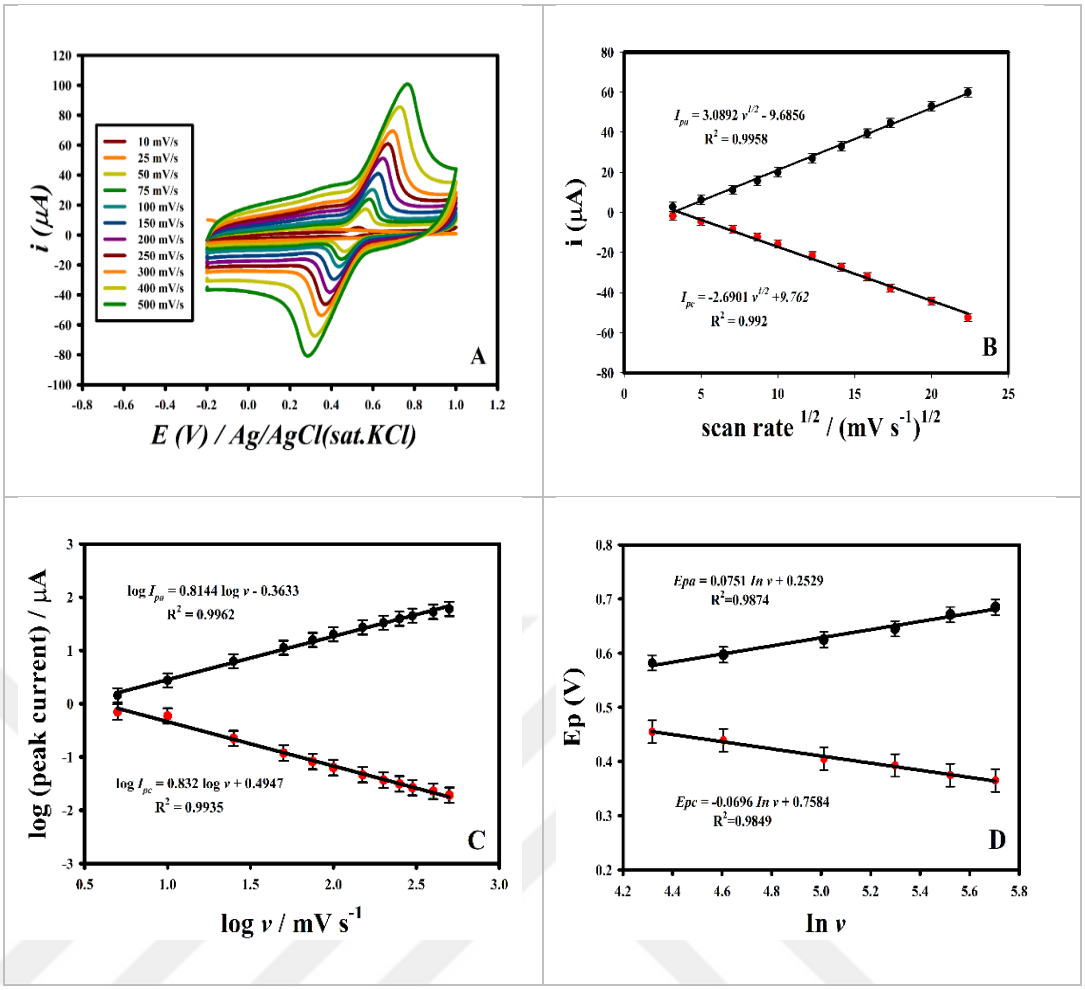

Figure 3.18 (A) CVs of the Co_3O_4/MWCNT/PPSF/GCE in pH 3.0 BR buffer solution in the presence of 10μmol L^{-1} RT at various scan rates (10–500 mV s^{-1}), (B) the plots of oxidation and reduction peak current of RTversus the square root of scan rate and (C) the plots of log v vs log I_{pa} and log I_{pc}.

According to Laviron's model (Eq. 2 and Eq. 3), the slopes of the line for Epa and Epc can be expressed as RT/(1 − α)nF and − RT/αnF, respectively.

$$Epa = E^{0'} + RT/(1 - \alpha)nF \, Inv \qquad \text{eq (2)}$$

$$Epc = E^{0'} - RT/\alpha nF \, Inv \qquad \text{eq (3)}$$

In these equations, R, T and F represent their usual meaning and α is the electron transfer coefficient, n is the number of transferred electrons in the electrode reaction and v is the scan rate of the applied potential range. The Laviron equation was used to calculate the number of electrons participating in the oxidation of rutin.

$$i_p = nFQ\upsilon/4RT \qquad \text{eq (4)}$$

where Q is the amount of charge integrated from the area of cyclic voltammetric peak, i_p represents the anodic or cathodic peak current, T is the temperature in Kelvin (298 K), R is the gas constant (8.314 $Jmol^{-1}$ K^{-1}), F is the Faraday constant (96500 C mol^{-1}) and n is the number of electrons transferred. From the slope of ip vs. υ, n was calculated to be 1.73 (≈ 2), which was in accordance with the expected theoretical value (Karabiberoğlu, Ş. U. and Dursun, Z., 2018). A possible mechanism for the oxidation of rutin (Fig. 3.19) is via the oxidation of the 3',4'-dihydroxy substituent on the rutin ring along with the transfer of two electrons and protons depicted in Scheme 1. In addition, the electron transfer rate constant between the modifier and GCE can be calculated using the equation below (Mazloum-Ardakani, M. Et.al., 2010 ; Tajik Et.al., 2013).

$$log\ ks = \alpha\ log(1 - \alpha) + (1 - \alpha)log\ \alpha - log(RT/nFv) - \alpha\ (1 - a)n\ \alpha\ FDE_p/2.3RT$$ eq (5)

Using the equations mentioned above, the values of α and k_s for the Co_3O_4/MWCNT/PPSF/GCE were calculated as 0.5 and 0.048 s^{-1}, respectively.

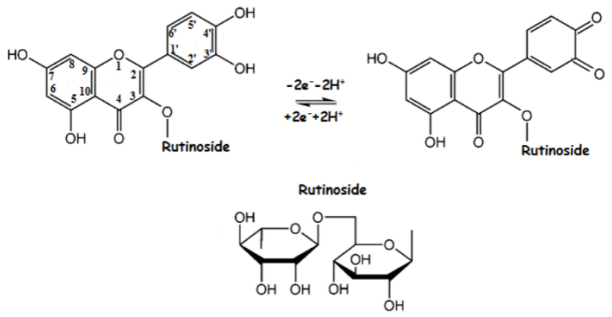

Figure 3.19 Possible mechanism of the electrochemical oxidation of rutin at Co_3O_4/MWCNT/PPSF/GCE.

<u>Square wave Voltammetric Behaviour of Rutin</u>

Square wave voltammetry (SWV) is one of the most common technique to examine the electrochemical performance of the new fabricated nanocomposite containing electrodes. The SWV technique was prefered for future studies to detection of rutin due to the higher current sensitivity than cyclic voltammetry. The SWV parameters including amplitude and frequency were optimized by monitoring $1.0x10^{-7}$ mol L^{-1} rutin oxidation in pH 3.0 BR buffer solution (Fig. 3.20 A and B;

Fig. 21 A and B). The effect of SW amplitude and frequency on oxidation peak were investigated in the range from 5 mV to 95 mV and from 1.0 Hz to 10.0 Hz respectively. The highest peak current was obtained with 5.0 Hz frequency and 55mV amplitude values. Therefore these values were choosen for following studies.

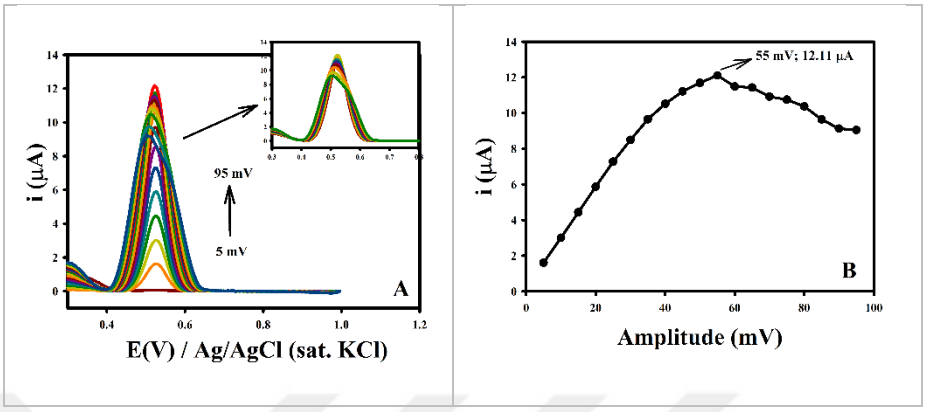

Figure 3.20 A) SW voltammograms of 0.1 µmol L^{-1} Rutin at Co_3O_4/MWCNT/PPSF/GCE in pH 3.0 BR buffer solution with amplitude 5.0 - 95.0 mV B) The influence of amplitude on the peak current of Rutin.

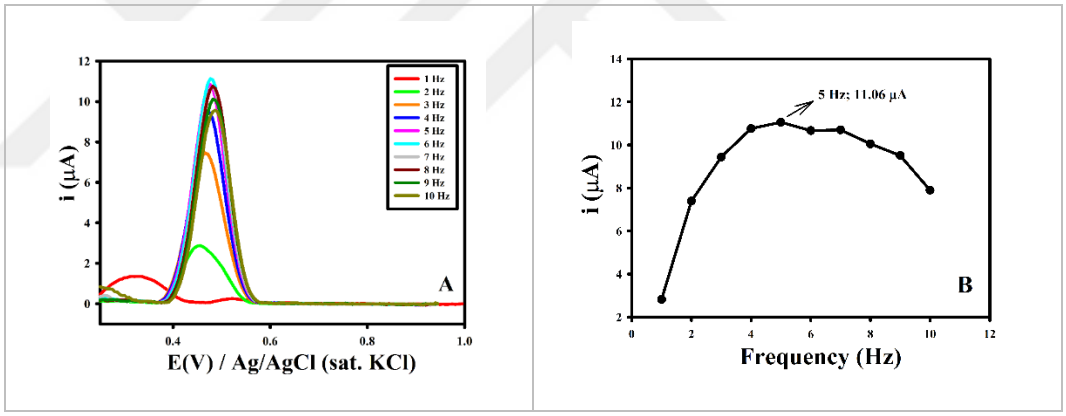

Figure 3.21 A) SW voltammograms of 0.1 µmol L-1 Rutin at Co_3O_4/MWCNT/PPSF/GCE in pH 3.0 BR buffer solution with frequencies 1-10 Hz; B) The influence of frequency on the peak current of Rutin.

Fig. 3.22 shows that square wave voltammetric response of bare GCE in pH 3.0 BR buffer solution in the absence and presence of increasing concentrations of rutin. The oxidation peak current of rutin was monitored by increasing rutin concentration in the range from 0.4- 100 µmol L^{-1}. The dynamic concentration range was obtained from 0.4 µ mol L^{-1} to 10 µmol $L^{-1}$with an equation of Ip=0.4647 c_{rutin} + 0.2386 (R^2=0.9914) (Fig. 3.23A-B).

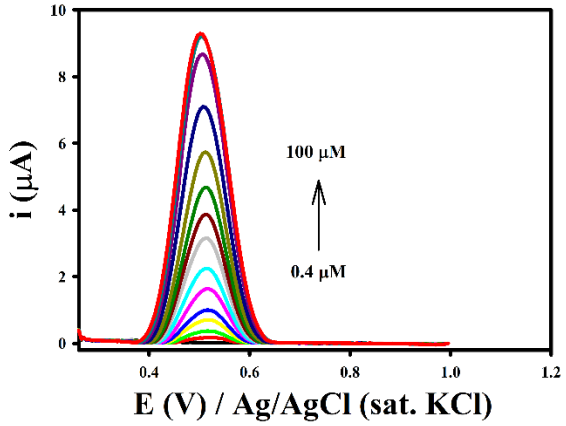

Figure 3.22 SWV of different concentrations of rutin (0.4; 0.6; 0.8: 1.0; 2.0; 4.0; 6.0; 8.0; 10.0; 20.0; 40.0; 60.0; 80.0 and 100.0 µmol L^{-1}) at bare GCE in the pH 3.0 BR buffer solution.

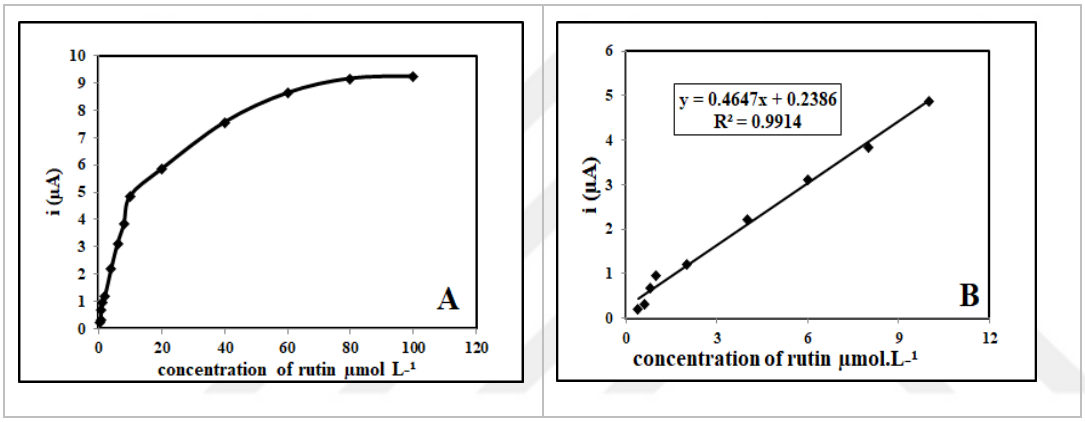

Figure 3.23 Plot of i_{rutin} vs. c_{rutin}. (A) dynamic range (0.4; 0.6; 0.8: 1.0; 2.0; 4.0; 6.0; 8.0; 10.0; 20.0; 40.0; 60.0; 80.0 and 100.0 µmol L^{-1}) and (B) lineer calibration range with 0.4-10.0 µmol L^{-1} rutin concentration in pH 3.0 BR buffer solution on bare GCE.

The oxidation peak current dependency on rutin concentration was studied in the concentration range from 0.01 µmol L^{-1} to 15.0 µmol L^{-1} at MWCNT/PPSF/GCE (Fig. 3.24). On the other hand, the calibration curves for the anodic peak height versus rutin concentrations were constituted with two different linear parts at MWCNT/PPSF/GCE (Fig. 3.25 A-B): the first linearity was provided in the range from 0.01 µmol L^{-1} to 0.8 µmol L^{-1} with linear regression equation of ipa(µA) = 8.155 C_{rutin} (µmolL-1) + 0.0767 (R^2=0.9903) and second linearity was establihed from 1.0 µmol L^{-1} to 8.0 µmol L^{-1} with a linear regression equation of ipa(µA)= 1.4517 C_{rutin} (µmolL^{-1}) + 8.023 (R^2=0.9936).

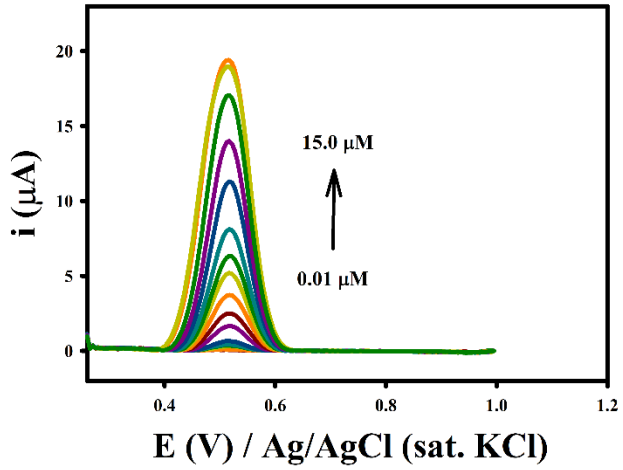

Figure 3.24 SWV of different concentrations of rutin (0.01; 0.02; 0.04; 0.06; 0.08; 0.1; 0.2; 0.4; 0.6; 0.8: 1.0; 2.0; 4.0; 6.0; 8.0; 10.0 and 15.0 µmol L^{-1}) at MWCNT/PPSF/GCE in the pH 3.0 BR buffer solution.

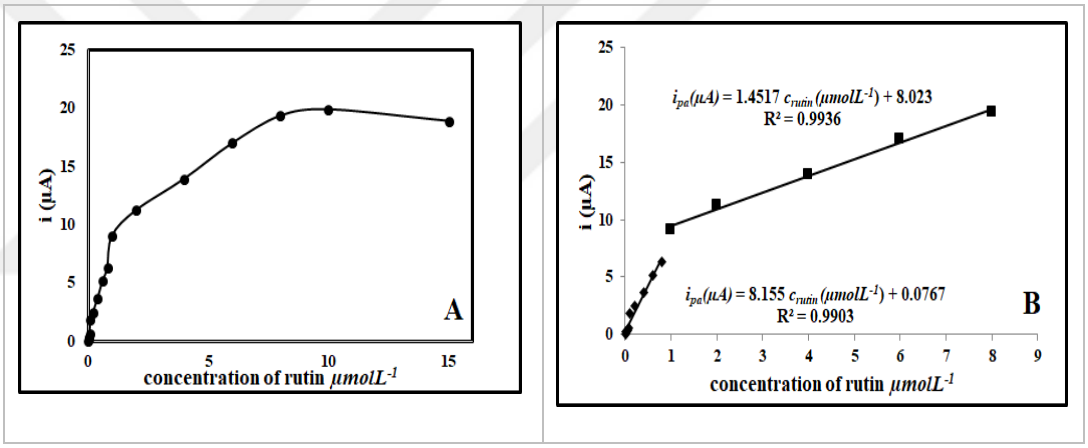

Figure 3.25 the plots of i_{rutin} vs. c_{rutin}. A) dynamic range (0.01; 0.02; 0.04; 0.06; 0.08; 0.1; 0.2; 0.4; 0.6; 0.8: 1.0; 2.0; 4.0; 6.0; 8.0; 10.0 and 15.0 µmol L^{-1}); B) lineer range (0.01 µmol L^{-1} to 8.0 µmol L^{-1}).

Under the ideal SWV conditions, the oxidation peak current dependency on rutin concentration was studied in the concentration range from 0.008 µmol L^{-1} to 40.0 µmol L^{-1} Co_3O_4/MWCNT/PPSF/GCE (Fig. 3.26). The oxidation peak current of rutin was also increased by inceasing of its concentration range from 0.008 µmol L^{-1} to 10.0 µmol L^{-1} (Fig. 3.26). The peak current linearity on rutin concentarion was deviated after addition of 8.0 µmol L^{-1} rutin (Fig. 3.27 A). On the other hand, the calibration curves for the oxidation peak height versus rutin concentrations were constituted with two different linear parts at Co_3O_4/MWCNT/PPSF/GCE (Fig. 3.27 B): the first linearity was provided in the range from 0.008 µmol L^{-1} to 0.6 µmol L^{-1} with linear regression equation of

$i_{pa}(\mu A)$= 5.1657 C_{rutin} $(\mu molL^{-1})$ + 0.1533 (R^2=0.9908) and second linearity was establihed from 0.8 µmol L^{-1} to 6.0 µmol L^{-1} with a linear regression equation of $i_{pa}(\mu A)$= 1.0469 C_{rutin} $(\mu molL^{-1})$ + 5.9123 (R^2=0.9938). The detection limit (LOD) was obtained as 0.00379 µmol L^{-1} (3.79 nmol L^{-1}), which calculated by using the LOD=3.3s/m. In this equation, m is the slope of the calibration graph and σ is the standard deviation of the response for blank solution.

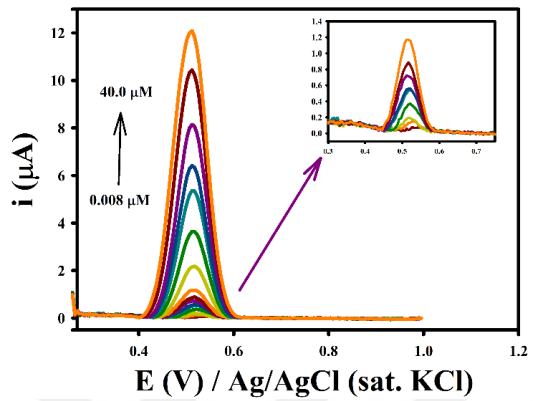

Figure 3.26 SWV of different concentrations of rutin (0.008; 0.01; 0.02; 0.04; 0.06; 0.08; 0.1; 0.2; 0.4; 0.6; 0.8; 1.0; 2.0; 4.0; 6.0; 8.0; 10.0; 20.0 and 40.0 µmol L^{-1}) in the pH 3.0 BR buffer solution.

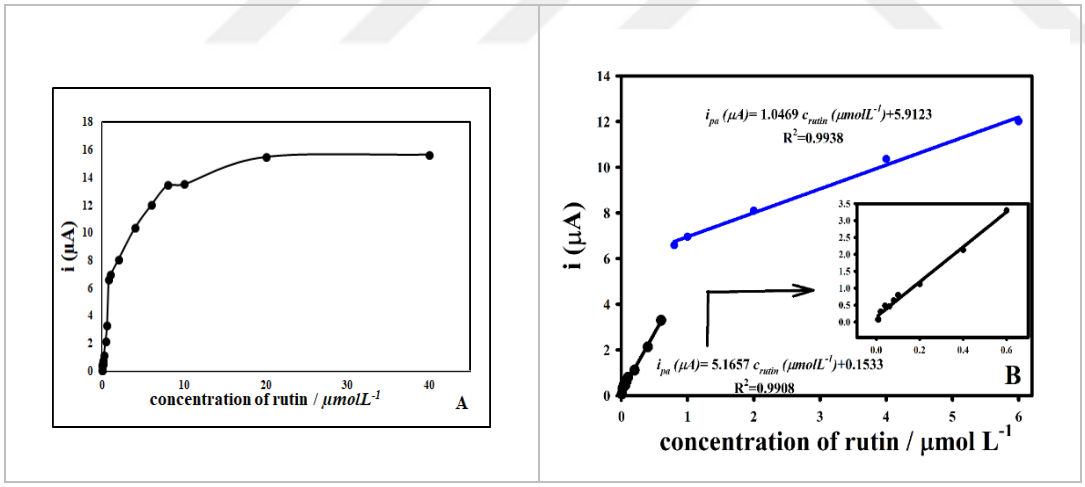

Figure 3.27 the plots of i_{rutin} vs. c_{rutin}. A) dynamic range (0.008; 0.01; 0.02; 0.04; 0.06; 0.08; 0.1; 0.2; 0.4; 0.6; 0.8; 1.0; 2.0; 4.0; 6.0; 8.0; 10.0; 20.0 and 40.0 µmol L^{-1}); B) lineer dynamic range (0.008 µmol L^{-1} to 6.0 µmol L^{-1}).

Table 3.6 Analytical characteristics for determination of rutin under optimum conditions.

Bare GCE	
Calibration Equation	i_{pa} = 0.4647 c_{rutin} + 0.2386
Lineer Range	4.0x10^{-7} M – 1.0x10^{-5}M
LOD	1.25x10^{-7} mol L^{-1}
R^2	0.9914
MWCNT/PPSF/GCE	
Calibration Equation	i_{pa} = 1.4517 c_{rutin} + 8.023 i_{pa} = 8.155 c_{rutin} + 0.0767
Lineer Range	1.0x10^{-8} M – 8.0x10^{-7} M 1.0x10^{-6} M – 6.0x10^{-6} M
LOD	9.72x10^{-9} mol L^{-1}
R^2	0.9903; 0.9936
Co_3O_4/MWCNT/PPSF/GCE	
Calibration Equation	i_{pa}= 1.0469c_{rutin}+ 5.9123 i_{pa} = 5.1657c_{rutin}+ 0.1533
Lineer Range	8.0x10^{-9} M – 6.0x10^{-7} M 8.0x10^{-7} M – 6.0x0x10^{-6} M
LOD	3.79x10^{-9} mol L^{-1}
R^2	0.9908 ; 0.9938

Table 3.7 indicates the comparative analytical performances of the purposed and recent published papers for the detection of rutin. The developed composite electrode in present study has a lower LOD and a wider linearity for rutin detection compare to recent studies.

Table 3.7 LOD values and lineer dynamic ranges of different modified electrodes for rutin detection

Electrodes	**LR (µmol L^{-1})**	**LOD (µmol L^{-1})**	**Reference**
NH_2-Fe_3O_4 NPs ErGO/GCE	0.006-0.1; 0.1-8.0;8.0-80	0.0040	He, Q, et al. 2019
Cu–CS/MWCNT/GCE	0.05 - 100	0.0100	Gholivand, M. Et al., 2016
CTAC-Gr-PdNPs/GCE	0.02 – 1.0	0.0050	Sheng, K et al., 2020
β-CD/MWNTs/GCE	0.4-100.0	0.2000	He, J. L et al., 2006
$Fe_{2.5}Cr_{0.2}Ce_{0.3}O_4$-rGO/GCE	0.075-12.0	0.0520	Şenocak, A. Et al., 2022
Nafion/ZIF-67@3D rGA/CILE	0.05 – 200.0	0.0280	Luo, G et al., 2020
AuNPs-MoS_2-GN/GCE	0.01 - 45	0.0040	Wang, Y et al., 2021

Co_3O_4/MWCNT/PPSF/GCE	**0.008 - 0.6; 0.8 – 6.0**	**0.0038**	**This work**

Reproducibility, repeatability, stability

To approve the possibility of the composite electrode in application use, the reproducibility, repeatability, stability of the Co_3O_4/MWCNT/PPSF/GC were studied in detail by monitoring the oxidation peak current of 0.1 µmol L^{-1} rutin in pH 3.0 BR buffer at optimum conditions.

The relative standart deviation (RSD) values were found with the SWV studies on inter-day (n=5) and intra-day (n=5) with Co_3O_4/MWCNT/PPSF/GC composite electrode for 0.10 µmol L^{-1} of rutin in pH 3.0 BR buffer solution. The inter-day and intra-day RSD values for 0.1 µmol L^{-1} rutin were 1.62 % and 2.63 % respectively (Fig. 3.28 A-B). These RSD values indicate that the Co_3O_4/MWCNT/PPSF modified GCE have high reproducibility. Moreover, the repeatability of the developed Co_3O_4/MWCNT/PPSF/GCE was used for recording of 50 consecutive measurements of oxidation reaction of 0.10 µmol L^{-1} rutin in pH 3.0 BR buffer solution and the RSD of the anodic peak height were found as 2.88 % which demostrate that the developed composite electrode has well repeatability. To prove the stability of the Co_3O_4/MWCNT/PPSF/GCE, it was used after stored in the supporting electrolyte during the experiments at room temperature for 10 days. At the end of 10 days, the response of the electrode towards 0.10 µmol L^{-1} rutin, was reduced by 3.8% displaying the good stability of the composite electrode.

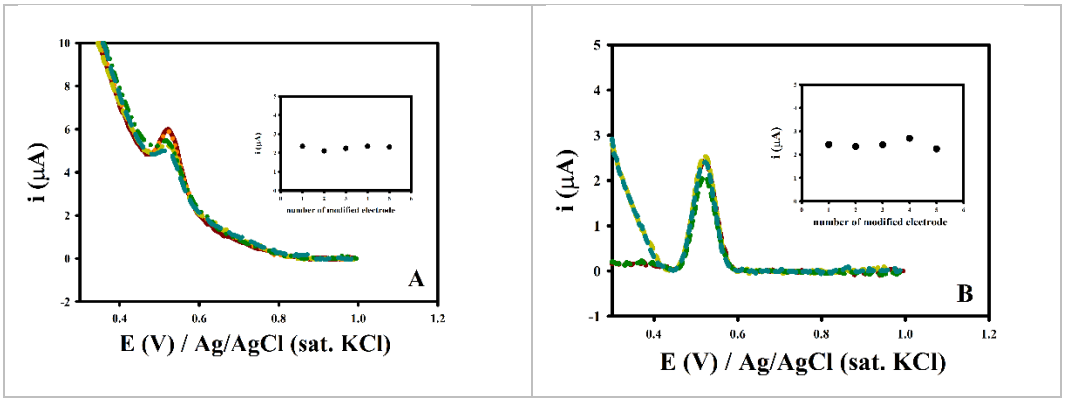

Figure 3.28 SWV studies on inter-day (n=5) and intra-day (n=5) with Co_3O_4/MWCNT/PPSF/GCE for 0.1 mM rutin.

Interference studies

The potential interference inorganic and organic compounds were studied in pH 3.0 BR buffer solution in the presense of 2.0 µmol L^{-1} rutin at the

Co_3O_4/MWCNT/PPSF/GCE. The results show that the anodic peak heigth of rutin was not significantly change in the presence of Na^+, Ni^{+2}, Ca^{+2}, SO_4^{2-}, CO_3^{2-} and NO_3^- until to 1000-fold excess amount. The electroactive organic interferences such as theophylline, caffeine, cysteine, glucose, fructose, sucrose, and quercetin, which may present in pharmaceutical samples were also investigated. There was no significant change in the oxidation peak current of rutin under conditions where the concentration ratio of organic compounds were reached 100-folds. As expected, the significant peak current difference was observed more then 100-fold amount of ascorbic acid, dopamine and quercetin (Fig. 3.29).

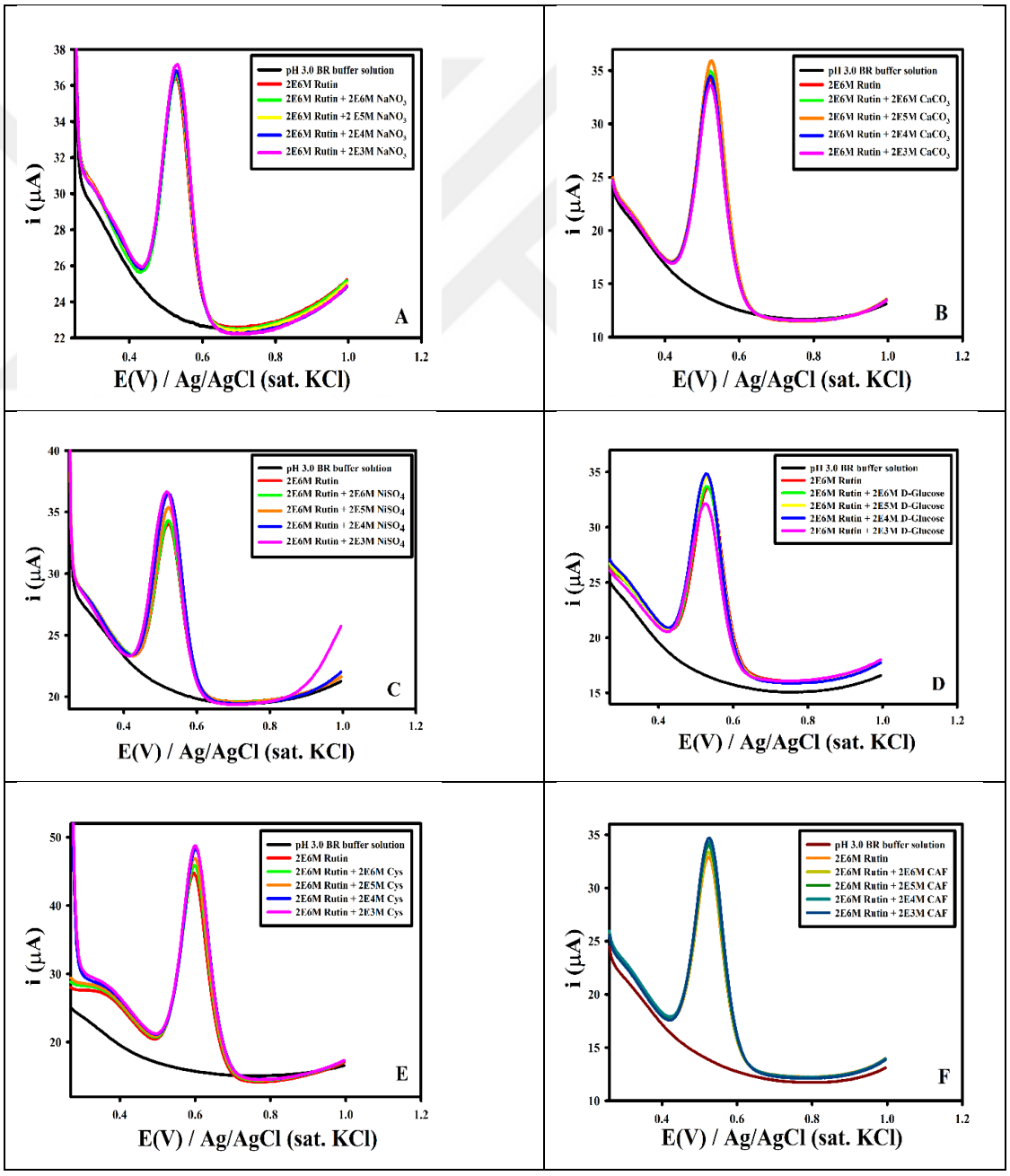

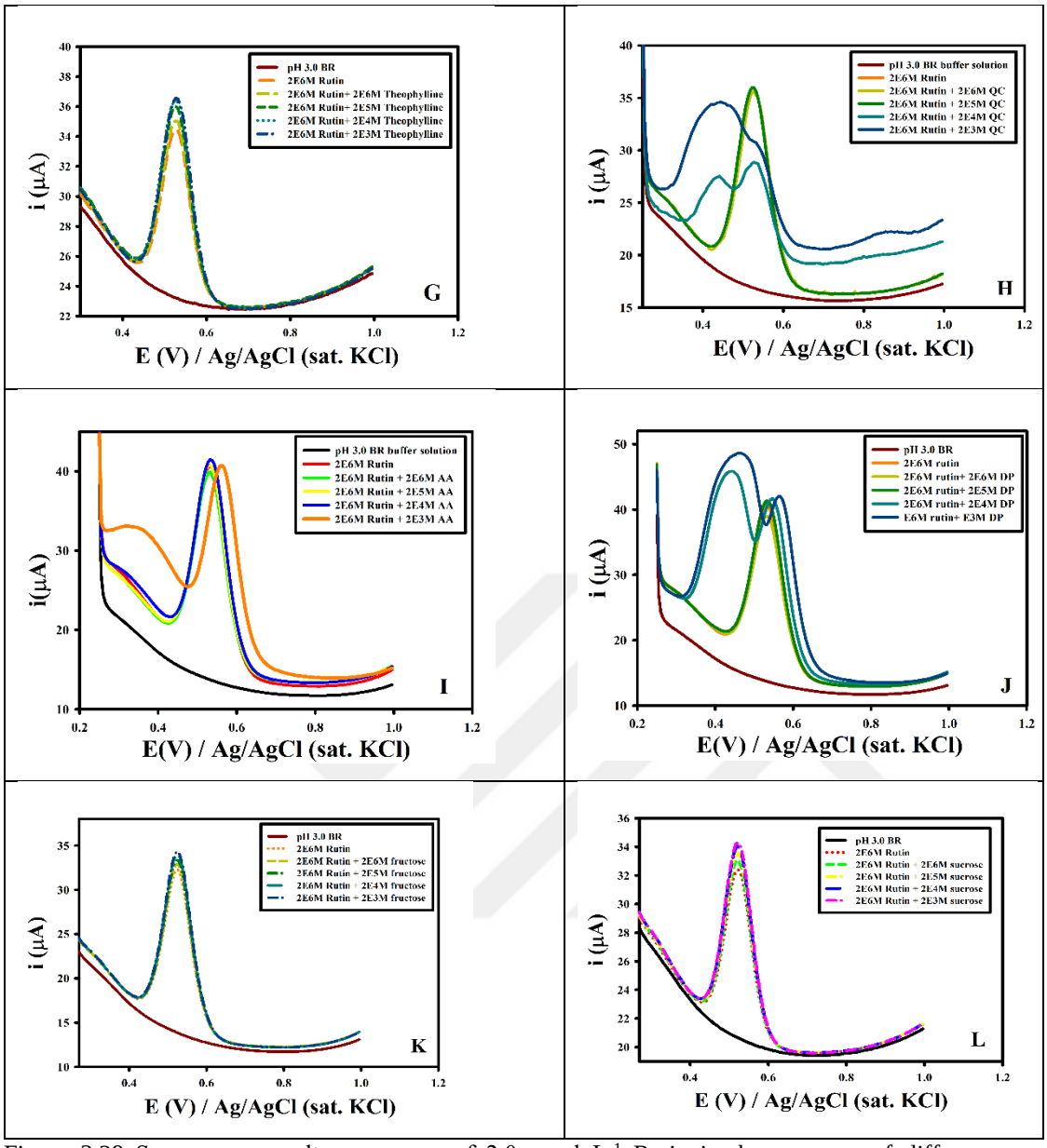

Figure 3.29 Square wave voltammograms of 2.0 µmol L^{-1} Rutin in the presence of different interfering species. A) $NaNO_3$, B) $CaCO_3$, C) $NiSO_4$, D) D-glucose, E) Cysteine (Cys), F) Caffeine (CAF), G) Theophylline H) Quercetin (QC), I) Ascorbic Acid (AA), J) Dopamine (DP), K) Fructose and L) Sucrose at various concentration ratios on Co_3O_4/MWCNT/PPSF/GCE.

Table 3.8 Relative (%) change of the analytical signal of rutin (2.0 µM) in the pH 3.0 BR buffer solution.

Interfering species	**Molar ratio ([Interferingspecies]/[rutin])**	**Change on the analytical signal of Rutin (%)**
Ascorbic acid	10	+3.28
	100	+63.14
	1000	-3.25
Dopamine	10	+2.36
	100	-41.64
	1000	-50.13
Quercetin	10	+2.87
	100	-
	1000	-
Glucose	10	+1.53

	100	+5.33
	1000	-25.7
Fructose	10	+3.76
	100	+6.41
	1000	+11.77
Sucrose	10	+5.88
	100	+10.08
	1000	+16.49
Theophylline	10	+4.59
	100	+13.01
	1000	+20.461
Caffeine	10	+.2.59
	100	+6.18
	1000	+7.85
Cysteine	10	+3.11
	100	+6.39
	1000	+4.13
Na^+	10	+3.72
	100	+3.66
	1000	+6.92
Ca^{2+}	10	+3.50
	100	+5.40
	1000	-2.91
Ni^{2+}	10	+3.12
	100	+6.39
	1000	+12.49
NO_3^-	10	+3.72
	100	+3.66
	1000	+6.92
CO_3^{2-}	10	+3.50
	100	+5.40
	1000	-2.91
SO_4^{2-}	10	+3.12
	100	+6.39
	1000	+12.49

Real sample analysis with Co_3O_4/MWCNT/PPSF/GCE

In order to investigate the pharmaceutical sample application of the developed modified electrode, two tablets were weighed and powdered in agate mortar and dissolved in ethanol. The suspention was separated by filtration. After the residue was washed with ethanol, the clear filtered solution was diluted with ethanol to a volume of 100 mL. The standard addition method was used to evaluate the performance of Co_3O_4/MWCNT/PPSF/GCE (Figure 3.30). The results were given in Table 3.9. The recovery values were obtained between 96.3 - 97.5 % for the rutin tablets. The relative standard deviation (RSD) was less than 5.0%. The obtained data indicate that Co_3O_4/MWCNT/PPSF/GC electrode could be applied for the detection of rutin content in pharmaceutical samples.

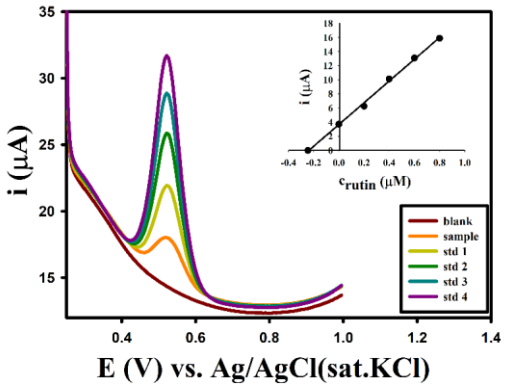

Figure 3.30 SWs for standart addition method of rutin determination in rutin tablet sample. Inset: Related calibration curve for rutin.

Table 3.9 Detection of rutin in pharmaceutical samples by SWV.

sample	Added (µM)	Found (µM)	Recovery(%)	RSD (n=3)
tablet	0.40	0.385	96.3	2.3
	0.60	0.586	97.7	3.2
	0.80	0.780	97.5	4.6

3.2 Electrochemical behavior of of Acetaminophen

3.2.1 Preparation of graphene oxide Modified GCE

In order to prepare 0.05 g of graphene oxide, 3.0 mL of N,N-dimethyl formamide (DMF) was used. As a consequence of this, a suspense combination with a dark color is formed. A 10 µL of GO suspension were injected on the surface of the pre-conditioned bare GCE. The solvent, dimethylformamide (DMF), used in the suspension was evaporated on the surface of the glassy carbon electrode (GCE) at a temperature of 70˚C for one hour.

3.2.2 Preparation of GO and MnO_2/h-MoO_3 Modified GCE

MnO_2/h-MoO_3 hybrid metal oxide materials with different ratios were successfully synthesized. Then composite material suspentions were prepared with GO and MnO_2/h-MoO_3 in different ratios (1:1, 2:1, 3:1 and 4:1) by dispesing in DMF. A 10 µL of the suspension was dropped on the bare GCE surface and then the solvent of the suspention was evapotrated at 70°C for more than an hour in an oven.

3.2.3 Surface Characterizations of Modified Electrodes

The prepared nanomaterials was characterized using various techniques such as SEM, CV, EIS, XPS and XRD to identify the surface morphology chemistry and electron transfer rate of the electrodes. The morphology of the electrodes was identified by SEM and the image of each electrode was given in Fig. 3.31 for h-MoO_3 (A), (3:1)(MnO_2:h-MoO_3) (B), GO/GCE (C) and (3:1)(MnO_2:h-MoO_3)(5%)+GO(95%)/GCE (D) respectively. Fig. 3.31 A and B show that the synthesized h-MoO_3 rods exhibited a hexagonal cross section which formed in flower-like structures. It can be observed that the graphene oxide in Fig. 3.31 C has a homogeneous layered structure. Fig. 3.31 D indicate that both layered structure of graphene oxide and MnO_2:h-MoO_3 mixture. To confirm the composition of (3:1)(MnO_2:h-MoO_3)(5%)+GO(95%)/GCE nanocomposites, the EDX elemental analyses were diplayed the presence of Mn, Mo, C and O elements on the composite electrodes surface (Fig 3.31E).

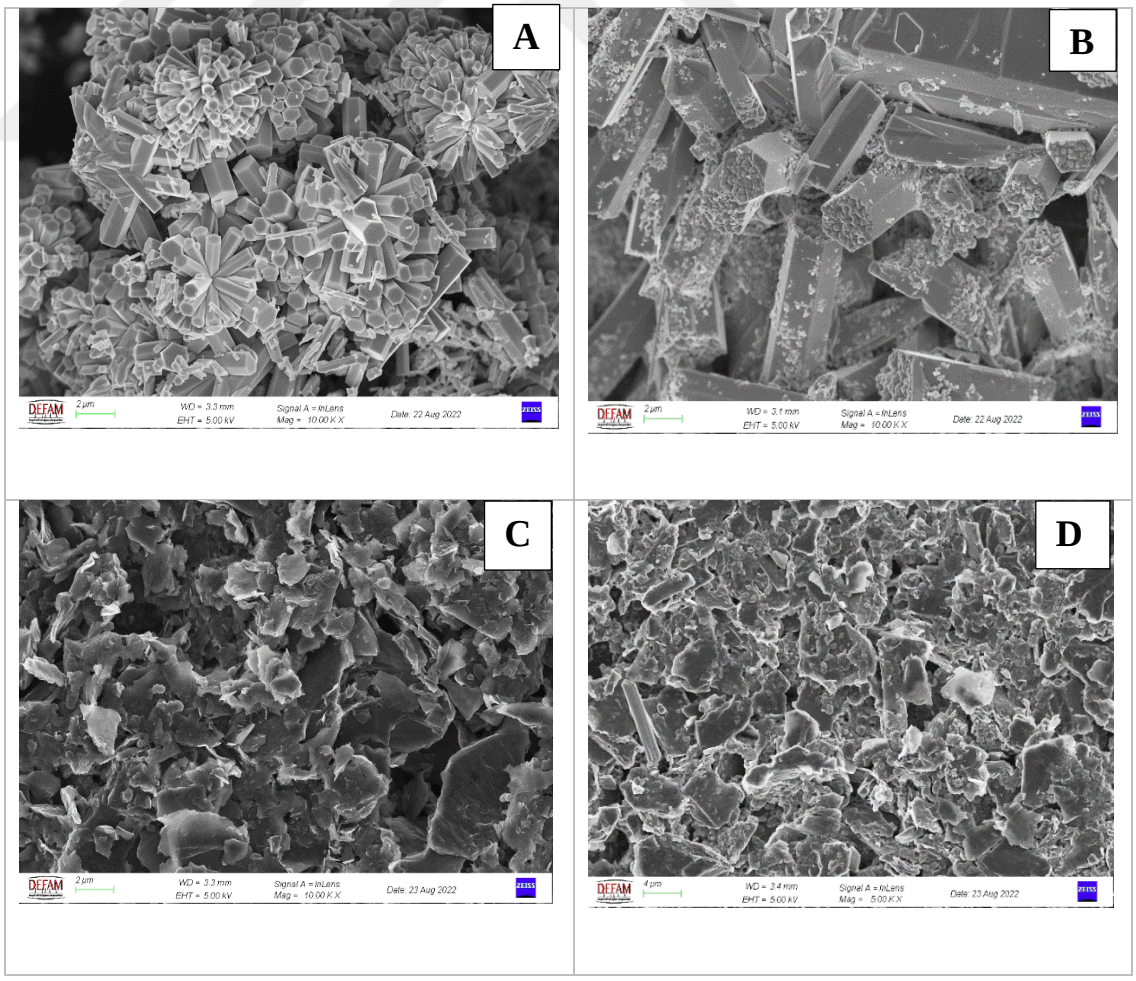

Element	Weight %	Atomic %
C	78.72	87.85
O	12.38	10.38
Mo	7.07	0.99
Mn	0.39	0.9 (E)

Figure 3.31 SEM images of (A) h-MoO_3, (B) (3:1)(MnO_2/h-MoO_3), (C) GO/GCE with 10000 magnitude and (D)(3:1)(MnO_2/h-MoO_3)(5%)+GO(95%)/GCE with 5000 magnitude. E) EDX results of the (3:1)(MnO_2/h-MoO_3)(5%)+GO(95%)/GCE.

The detailed surface chemical composition and oxidation state of (3:1)(MnO_2:h-MoO_3)(5%)+GO(95%)/GCE nanocomposite were performed by XPS. The survey spectrum of the (3:1)(MnO_2:h-MoO_3)(5%)+GO(95%)/GCE indicate the presence C, O, Mn and Mo on the composite electrode (Fig. 3.32A). Fig. 3.32B represents of the Mn 2p XPS spectra of (3:1)(MnO_2:h-MoO_3)(5%)+GO(95%)/GCE surfaces. The spectra signfy two main peaks at 642.8 eV 654.8 eV for Mn^{4+} $2p_{1/2}$ and $2p_{3/2}$ respectively (Nesbitt and Banerjee, 1998). In Fig. 3.32C, Mo 3d consist of two peaks located at 236.4 eV and 233.4 eV regarding to the Mo^{6+} $3d_{3/2}$ and Mo^{6+} $3d5_{/2}$ respectively (Sun et.al., 2011). The XPS spectrum of C1s for GO (Fig. 3.32D) was shown that the main peak could be deconvoluted into five peaks at 284.0 eV (sp^2 hybridized carbon, C-C), 285.2 eV (sp^3 hybridized carbon C=C), 286.6 eV (C-O), 287.7 eV (C=O), and 288.9 eV (O - C=O) (Muralikrishna et.al, 2014) the functional groups could be formed on the GO sheets during the synthesis of graphene oxide.

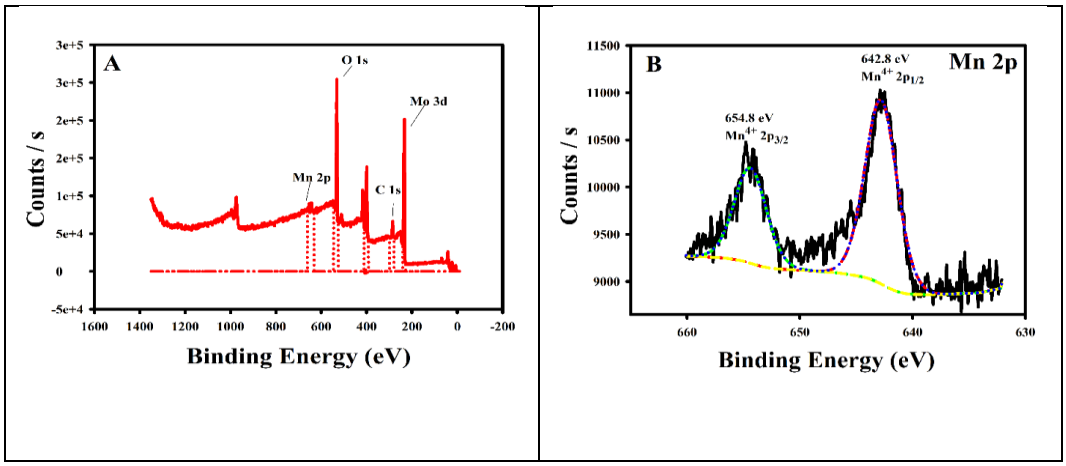

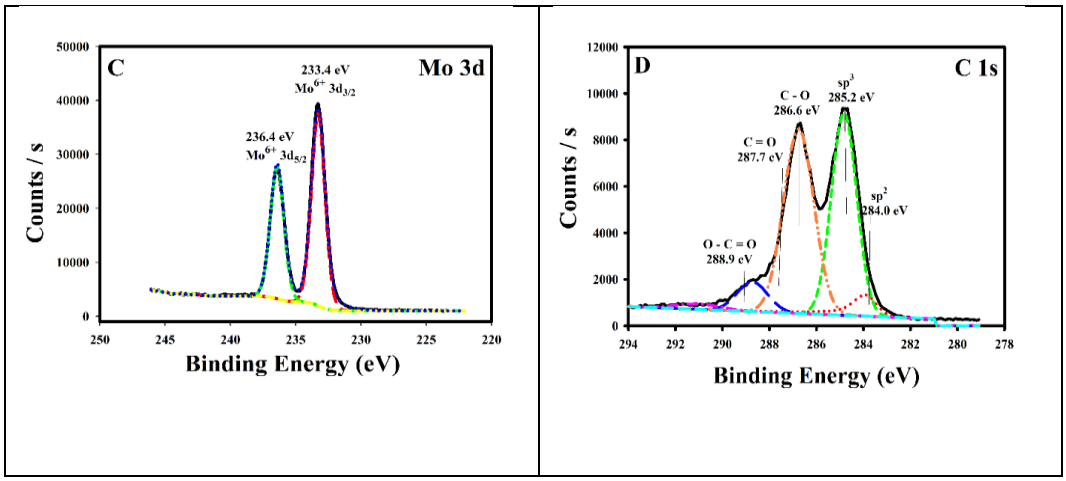

Figure 3.32 XPS spectrum (A) survey spectrum (B) Mn 2p, (C) Mo 3d, (D) C 1s spectra of (3:1)(MnO2:h-MoO3)(5%)+GO(95%) modified GCE.

Fig. 3.33A reveals the XRD patterns of (3:1)(MnO_2:h-MoO_3), displayed the diffraction peaks located at 2Θ = 9.60, 16.81, 19.68, 25.99, 29.59, 35.54 and 45.26 respectively. These well-defined peaks demostrated to (100), (110), (200), (210), (300), (310), and (400) crystal planes of h-MoO_3, which are consistent with the standard spectrum (JCPDF:21-0569), and these data were in relevance with the published hexagonal crystal h-MoO_3 (Shafi et. al., 2017; Sun Y. et. al., 2011).

Fig. 3.33B have shown XRD patterns of MnO_2 and (3:1) MnO_2:h-MoO_3. The peaks of MnO_2 (in Fig. 3.33B) corresponded to (100), (101) and (102) which are also formed in the XRD spectrum of (3:1) MnO_2;h-MoO_3. The fact that these peaks are broad and weak indicates that the crystallinity of MnO_2 particles is relatively poor (Zhou et.al., 2021; Kumar et.al. 2020)..

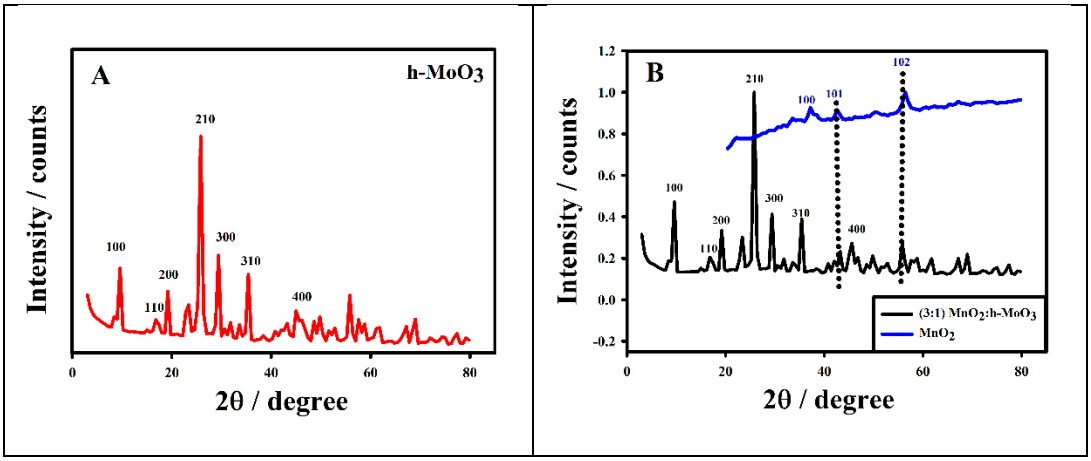

Figure 3.33 (A) The XRD spectra of synthesized h-MoO_3. (B) The XRD spectra of (3:1)(MnO_2:h-MoO_3) and MnO_2.

EIS experiments were performed at all electrodes as specified in order to investigate the rate of electron transfer at all electrodes (Fig. 3.34) in a 5.0 mmol

L^{-1} $[Fe(CN)_6]^{3-/4-}$ containing 0.1 mol L^{-1} KCl solution. In general, all electrodes showed a semi-circular Nyquist curve at higher frequencies, demonstrating an electron transfer-limited process, and a linear part at lower frequencies, indicating an electron diffusion-limited process. Table 3.10 demostrates the results of an equivalent circuit fit to the EIS data consisting of the charge transfer resistance (Rct), electrolyte resistance (Rs), Warburg impedance (W), and the double layer capacitance (Cdl). As expected, the bare GCE has the maximum electron transter Rct as 217 Ω, whereas the GO/GCE, (5%)(MnO_2)+(95%)GO/GCE, (5%)(h-MoO_3)+(95%)GO/GCE and (3:1)(MnO_2/h-MoO_3)(5%)+GO(95%)/GCE have Rcts of 36.8 nΩ, 2.79 μΩ , 1.96 μΩ and 76.2 nΩ, respectively. The Rct value of GO/GCE and (3:1)(MnO_2/h-MoO_3)(5%)+GO(95%)/GCE have lower than bare GCE. On the other hand, the Rct value of (3:1)(MnO_2/h-MoO_3)(5%)+GO(95%)/GCE was higher then the Rct value of GO/GCE, because the (3:1)(MnO_2/h-MoO_3)(5%)+GO(95%) composite structure has more oxide components then GO. The results shows that the composite electrodes have higer electron rate compare with bare GCE.

The CV behaviour of bare GC, GO/GC, MnO_2(5%)+GO(95%)/GC, MoO_3(5%)+GO(95%)/GC and (3:1)(MnO_2/h-MoO_3)(5%)+GO(95%)/GC electrodes were performed in presence of 0.1 M KCl + 1.0 mM $[Fe(CN)_6]^{3-/4-}$ at 0.05 V s^{-1} scan rate. Fig. 3.34 shows that a well-defined redox behaviour was proved for bare and composite electrodes. Although high peak currents were obtained at electrodes GO/GCE and (3:1)(MnO_2/h-MoO_3)(5%)+GO(95%)/GCE, the oxidation and reduction peak potentials remained unchanged for all the electrode, which can be clarified with increase in the electroactive surface area . The electroactive surface areas of all electrodes were calculated by Randles-Sevcik equation (eq.1) (Song et al., 2010).

$$Ip= (2.69\ 10^5)\ n^{3/2}\ A\ D^{1/2}\ C\ \nu^{1/2} \quad \text{..... (eq.1)}$$

n is the number of electrons transferred, A is the electroactive surface area (cm^2), D is the diffusion coefficient ($cm^2\ s^{-1}$), C is the concentration of $K_4Fe(CN)_6$ (mol cm^{-3}) and v is the scan rate (V s^{-1}). The $[Fe(CN)_6]^{3-/4-}$ system is transfered one electron (n=1), D was accepted as 6.70×10^{-6} $cm^2\ s^{-1}$, ferro-ferricyanide concentration (C) was taken 1.0 mmol L^{-1}.

The active surface area was calculated according to Randles-Sevcik equation (eq.1) mentioned in section 3.1.4 above, from the slope of I_p vs $v^{1/2}$, the EASA values of the bare GC, MnO_2(5%)+GO(95%)/GC, MoO_3(5%)+GO(95%)/GC, GO/GC and (3:1)(MnO_2/h-MoO_3)(5%)+GO(95%)/GC electrodes were calculated 0.086, 0.103, 0.344, 0.380 and 0.387 cm^2 respectively. These results show a significant improvement in surface area after modification with (3:1)(MnO_2/h-MoO_3)(5%)+GO(95%) nano composite.

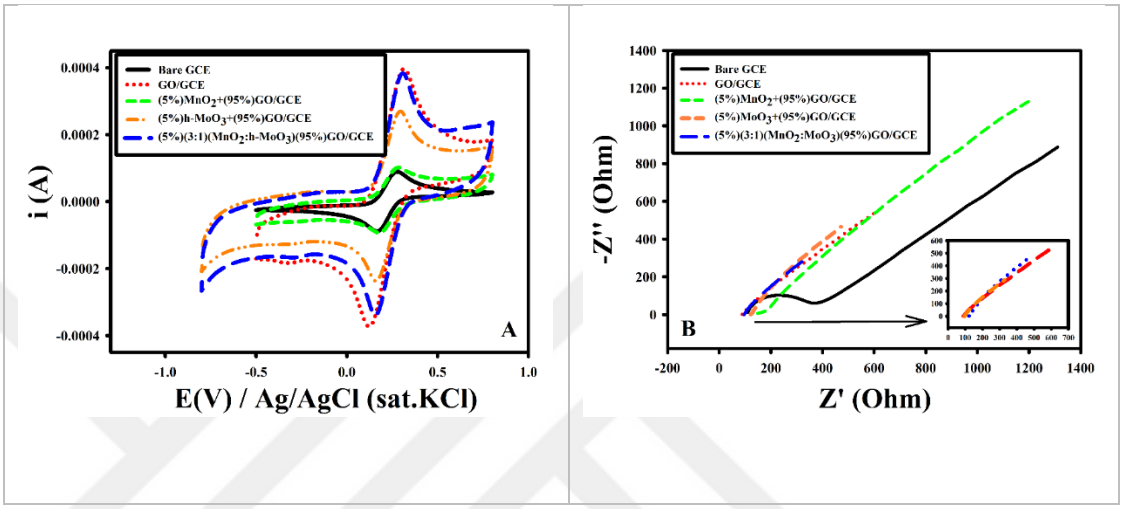

Figure 3.34 A) Cyclic voltammograms of bare and modified GCE in with 5.0 mmol L^{-1} $K_3[Fe(CN)_6]/K_4[Fe(CN)_6]$ / 0.1 mol L^{-1} KCl with 0.05 V s^{-1} scan rate. B) Nyquist plots of the bare GCE, GO/GCE, (MnO_2)(5%)+GO(95%)/GCE, (h-MoO_3)(5%)+GO(95%)/GCE and (3:1)(MnO_2/h-MoO_3)(5%)+GO(95%)/GCE. The frequencies at the formal potential range from 0.05 to 75000 Hz. For the modified electrodes, the Randles circuit model is shown inset.

Table 3.10 The values of Rs, Rct, CdI and W for bare and modified electrodes.

ELECTRODE	Rs	Rct	CdI	W(mMho)
Bare GCE	115Ω	**217 Ω**	1.83 mF	1.41
(5%)(MnO_2)+(95%)GO/GCE	143 Ω	**2.79 µΩ**	145 µF	1.22
(5%)(h-MoO_3)+(95%)GO/GCE	124 Ω	**1.96 µΩ**	1.37 mF	2.68
GO/GCE	91.4Ω	**36.8nΩ**	1.75 mF	5.16
(5%)(3:1)(MnO_2:h-MoO_3)+(95%)GO/GCE	97.4 Ω	**76.2 nΩ**	1.74 mF	4.39

3.2.4 Electrochemical Behaviour of ACP on bare GCE and modified electrodes

To investigate the electrochemical behavior of bare and modified electrodes, the cyclic voltammograms of bare GC, GO/GC, (5%)(MnO_2)+(95%)GO/GCE, (5%)(h-MoO_3)+(95%)GO/GCE and (5%)(3:1)(MnO_2:h-MoO_3)+(95%)GO/GCE

electrodes in pH 6.60 PBS containing $1.0x10^{-5}$ mol L^{-1} ACP are shown in Fig. 3.35. The CVs were recorded from 0.0 V to 1.20 V potential ranges with 0.05 Vs^{-1} scan rate. On all electrodes, a quasi-reversible electrode reaction was observed. The peak potential and calculated peak current of ACP on all electrodes were given in Table 3.11. While the oxidation peak value shifted more positive, the reduction peak value shifted negative values (Table 3.11).

From the voltammograms in Fig. 3.35B, the oxidation and reduction peak currents of ACP were increased at composite electrodes compare with bare GCE while the peak potentials slightly were shifted to more positive potentials for oxidation reaction and to low positive potentials for reduction reaction. In addition, oxidation peak current of ACP on (3:1)(MnO_2:h-MoO_3)(%5)+GO(95%)/GCE was increased compared to bare GCE, GO/GCE, (MnO_2)(5%)+GO(95%)/GCE and (h-MoO_3)(5%)+GO(95%)/GCE as 17.58; 2.60 and 1.786 times, respectively. Furthermore, additional oxidation and reduction peaks were observed at 0.65 V and at 0.39 V respectively and in the presence of 0.1 mmol L^{-1} ACP in PBS buffer solution for only MnO_2 particles containing electrodes. The additional peaks can be explained by oxidation of Mn^{4+} to Mn^{6+} and reduction of Mn^{6+} to Mn^{4+} on the electrode surfaces. This interpretation was supported with CV's obtained in the supporting electrolyte (absence of ACP) solution at same conditions (Fig. 3.35A), because the the aforementioned peaks also appeared for only MnO_2 particles including electrodes at almost same potentials.

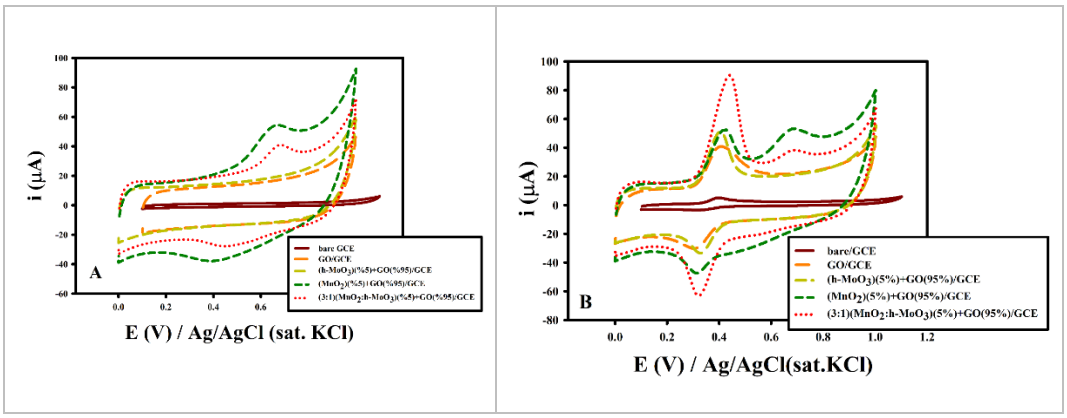

Figure 3.35 CV s of A) in the absence B) in the presence of 0.1 mM ACP in pH 6.60 PBS buffer solution at bare GCE and modified electrodes.

Table 3.11 Comparison of ACP (0.1 mmol L^{-1}) oxidation peak characteristics at modified electrodes in pH 6.60 PBS.

ELECTRODE	Acetaminophen			
	i_a(µA)	E_a (V)	i_c (µA)	E_c (V)
Bare GCE	3.801	0.397	1.680	0.324
GO/GCE	25.654	0.405	14.911	0.309
(MnO_2)(5%)+GO(95%)/GCE	26.215	0.415	13.352	0.311
(h-MoO_3)(5%)+GO(95%)/GCE	35.957	0.405	18.522	0.331
(3:1)(MnO_2:h-MoO_3)(%5)+GO(95%)/GCE	**66.809**	**0.440**	**40.405**	**0.298**

To obtain the optimum parameters to monitore the electrochemical behaviour of ACP on (3:1)(MnO_2:MoO_3)(%5)+GO(95%)/GCE, the major factors that should be considered were MnO_2:h-MoO_3 hybrid metal oxide materials with different ratios and pH of the supporting electrolyte solution. The optimum conditions for voltammetric determination of ACP were found by measuring the peak currents while varying each parameter mentioned above. The detailed studies were explained followed section.

Effect of different ratios of MnO_2-MoO_3 suspension ((1:1), (2:1), (3:1), (4:1)) on cyclic voltammetric behaviour of ACP

Different weight ratios of MnO_2:h-MoO_3 hybrid metal oxide materials were successfully synthesized. The nanocomposite was prepared by incorporate the graphene oxide and MnO_2:h-MoO_3 in different ratios of MnO_2-MoO_3 and then the composite materials were dispersed in DMF to obtain a suspension. A 10 µL of MnO_2-MoO_3(%5) and graphene oxide containing suspension was dropped on the pre-conditioned bare GCE surface. The electrochemical behavour of ACP was investigated in pH 7.0 PBS at all electrodes which were prepared with graphene oxide and MnO_2:h-MoO_3 in different ratios of MnO_2-MoO_3 (Fig. 3.36). The highest peak currents were obtained on (3:1)(MnO_2:h-MoO_3)(%5)+GO/GCE for Acp (Table 3-12).

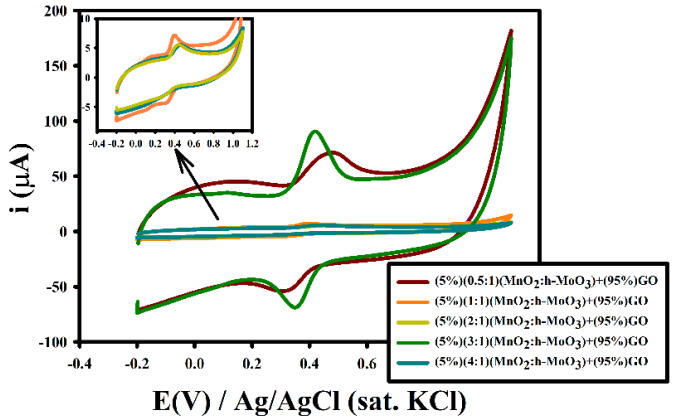

Figure 3.36 Voltammetric behaviour of ACP at different ratios (MnO_2:h-MoO_3) suspension

Table 3.12 Comparison of ACP (0.1 mmol L^{-1}) oxidation peak characteristics at at different ratios (3:1) (MnO_2:h-MoO_3) suspension in pH 6.60 PBS.

Electrode	Acetaminophen			
	I_{pa} (µA)	E_{pa} (V)	I_{pc} (µA)	E_{pc} (V)
(0.5:1)(MnO_2:h-MoO_3)(%5)+GO/GCE	24.888	0.474	17.59	0.322
(1:1)(MnO_2:h-MoO_3)(%5)+GO/GCE	39.505	0.395	11.828	0.319
(2:1)(MnO_2:h-MoO_3)(%5)+GO/GCE	19.048	0.459	-	-
(3:1)(MnO_2:h-MoO_3)(%5)+GO/GCE	**51.976**	**0.417**	**36.049**	**0.351**
(4:1)(MnO_2:h-MoO_3)(%5)+GO/GCE	22.126	0.439	-	-

Optimization of (3:1)(MnO_2:h-MoO_3) / GO ratio

To obtain the best electrochemical activity of nanocomposite surface which prepared from (3:1) MnO_2:h-MoO_3 and graphene oxide suspensions using different ratios from 1% to 10% of (3:1) MnO_2:h-MoO_3.

The electrochemical behaviour of 0.1 mmol L^{-1} ACP on (3:1)(MnO_2:h-MoO_3)(%5)+GO/GCE using different ratios from 1% to 10% of MnO_2:h-MoO_3 in suspentions was studied by cyclic voltammetry (CV) in pH 6.60 PBS. The CVs were recorded from 0.0 V to 1.20 V potential ranges with 0.05 Vs^{-1} scan rate. On all electrodes, a quasi-reversible electrochemical behaviour was observed (Fig. 3.37). On the other hand, the best electrochemical activity activity was observed on (3:1)(MnO_2:h-MoO_3)(5%)+GO(95%)/GCE. The peak potential and measured peak current of ACP at all electrodes were given in Table 3.13. The oxidation and reduction peaks of ACP were located at too close potentials for all

different ratio prepared MnO_2:h-MoO_3 /GO containing electrodes as (3:1) MnO_2:h-MoO_3 (from %1 to %10) +GO (from 99% to 90%)GCE (Table 3.13). From the CV data, the best electrochemical activity activity was observed for electrochemical behaviour of ACP on (3:1)(MnO_2:h-MoO_3)(5%)+GO(95%)/GCE. Therefore, the composite electrode will be used in future studies.

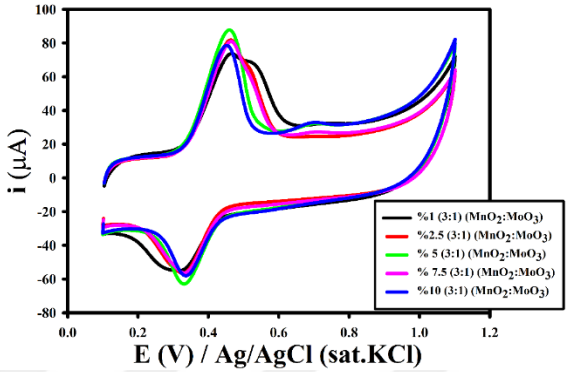

Figure 3.37 Voltammetric behaviour of acetaminophen at different ratios (3:1) (MnO_2:h-MoO_3+GO) suspension (from %1 to %10)

Table 3.13 Comparison of ACP (0.1 mmol L^{-1}) peak characteristics at at different ratios (3:1)(MnO_2-MoO_3)+GO suspension (from %1 to %10) in pH 6.60 PBS.

%(3:1)MnO_2:h-MoO_3+ %GO	**Acetaminophen**			
	I_{pa} (µA)	**E_{pa} (V)**	**I_{pc}(µA)**	**E_{pc}(V)**
% 1(3:1)+%99GO	51.136	0.465	28.731	0.320
%2.5(3:1)+%97.5GO	63.644	0.463	35.031	0.330
% 5(3:1)+%95GO	**66.340**	**0.459**	**38.431**	**0.332**
%7.5(3:1)+%92.5GO	61.504	0.463	32.240	0.334
% 10(3:1)+%90GO	57.865	0.451	34.067	0.338

Effect of supporting electrolyte pH on ACP oxidation

The effect of pH on the peak currents and peak potentials of the electrochemical behavior of 0.1 mmol L^{-1} ACP was investigated using CV technique at a (3:1)(MnO_2:MoO_3)(%5)+GO/GC electrode throughout a range of pH values from 4.00 to 8.00 (Fig. 3.38A). The higher oxidation and reduction peak currents were found at pH 6.60 phosphate buffer solution. The peak current of ACP decreased at pH values greater than 6.0. However, as the pH of the supporting electrolyte solution was increased, a more negative shift occurred in the ACP's peak

potential (Fig. 3.38 A). The linear equation was E_{pa} = 0.0586 pH + 0.8153 (R^2 = 0.9947). A slop of -0.0586 V pH^{-1} in Fig. 3.38 B indicated that the ratio of electrons and protons taking part in the electrode reaction was 1:1. Since the high peak currents of ACP in both oxidation and reduction reactions were obtained at pH 6.6 on (3:1)(MnO_2:MoO_3)(%5)+GO/GC electrode, the optimum pH was chosen as pH 6.6 for future studies.

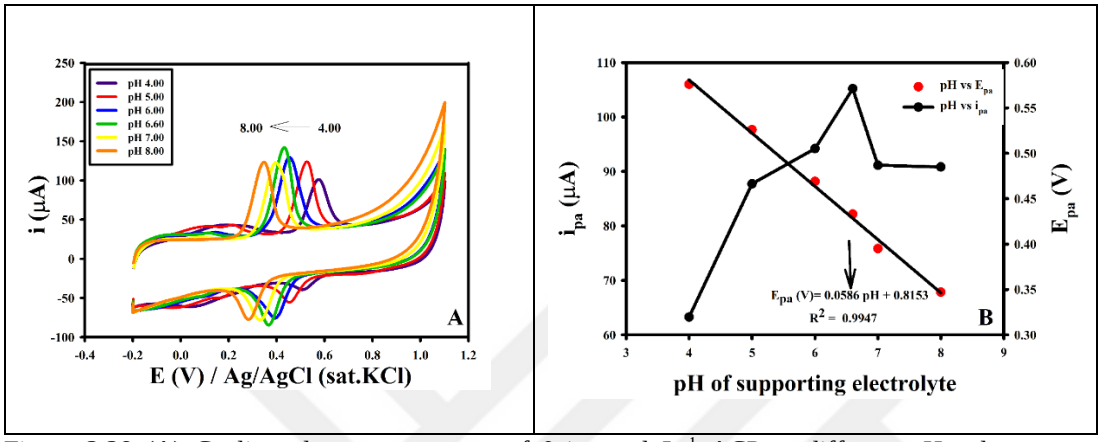

Figure 3.38 (A) Cyclic voltammetry curves of 0.1 mmol L^{-1} ACP at different pH values on (3:1)(MnO_2:h-MoO_3)(5%)+GO(95%)/GCE); (B) The effect of pH on the i_{pa} and E_{pa} of ACP.

Scan Rate Studies of ACP at (3:1)(MnO_2:h-MoO_3)(5%)+GO(95%)/GCE)

To further investigate the characteristics of ACP at (3:1)(MnO_2:h-MoO_3)(5%)+GO(95%)/GCE) the influence of the scan rate on the electrochemical behaviour of ACP was studied by CV (Fig. 3.39A). The influence of the scan rate (v) on the peak currents and peak potentials of 10 μmol L^{-1} ACP, was studied over the range from 5 to 500 mV s^{-1}. In Fig. 3.39B, the anodic and cathodic peaks current were increased linearly with the square root of scan rate ($v^{1/2}$) and the equations were obtained as I_{pa} (μA) = 18.068 $v^{1/2}$ - 31.293 (R^2 = 0.9985) and I_{pc} (μA) = −13.2 $v^{1/2}$ + 35.753 (R^2 = 0.9941). On the other hand, the curve for log *Ipa* and log *Ipc* vs. log *v* shows good linearity and the slopes of *log Ipa* and *log Ipc* vs *log v* were 0.7173 and 0.9277, respectively. The obtained slopes value was between 0.5 and 1.0 therefore the electrode process could be controlled by both diffusion and adsorption processes (Fig. 3.39 C).

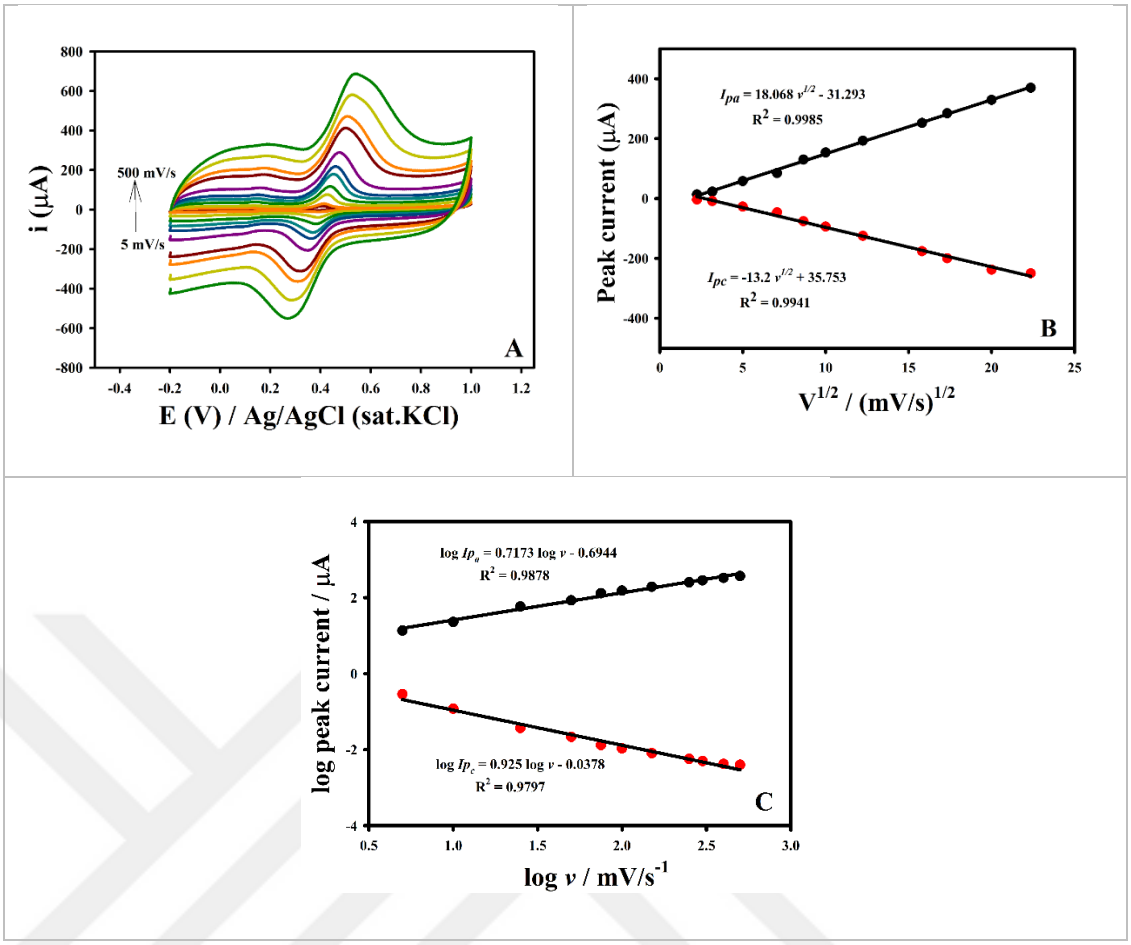

Figure 3.39 (A) CVs of the (3:1)(MnO_2:h-MoO_3)(5%)+GO(95%)/GCE) in pH 6.60 PBS in the presence of 10 μmol L^{-1} ACP at various scan rates (5–500 mV s^{-1}), (B) the plots of oxidation and reduction peak currents of ACP versus the square root of the scan rate, (C) the plots of log v vs log I_{pa} and log I_{pc}.

Square Wave Voltammetric Determination of ACP

The analytical performance of (3:1)(MnO_2:MoO_3)(5%)+GO(95%)/GCE for the voltammetric detection of ACP was investigated by the SWV technique. The influence of SW amplitude and frequency on the oxidation peak current of 2.0 μmol L^{-1} ACP in pH 6.60 PBS were examined in the range from 5mV to 60 mV and from 1.0 Hz to 10.0 Hz respectively (Fig. 3.40 and 3.41). The highest peak current was obtained with 3.0 Hz frequency and 20.0 mV amplitude values. Therefore these values were choosen for future studies.

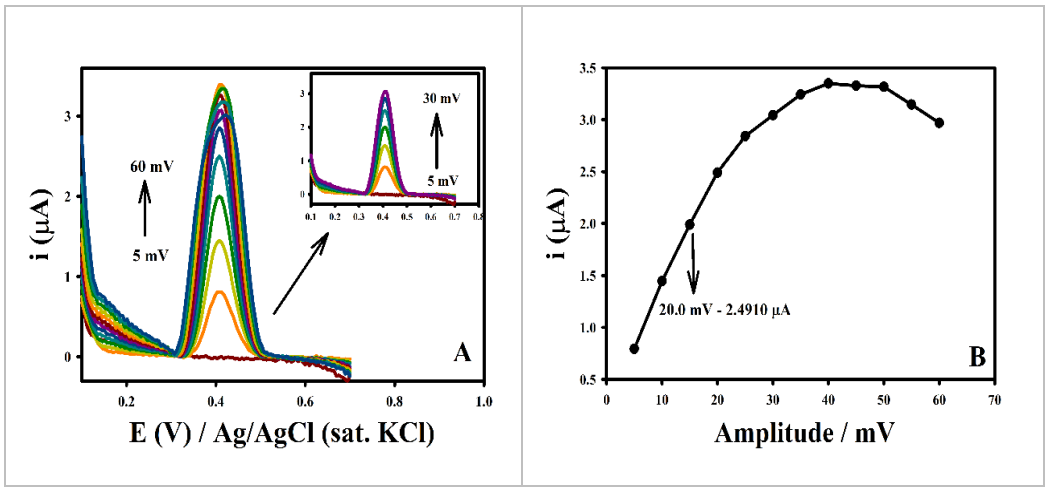

Figure 3.40 A) SWVs of 1.0 µmol L^{-1} ACP at (3:1)(MnO_2:h-MoO_3)(5%)+GO(95%)/GCE) in pH 6.60 PBS with amplitude 5.0 – 60.0 mV/s; B) The influence of amplitude on the peak current of ACP.

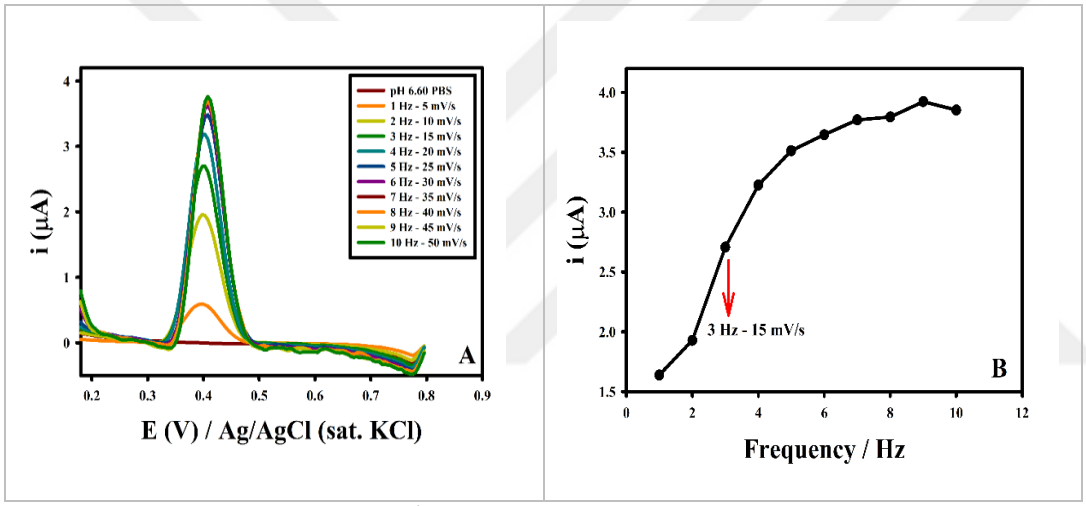

Figure 3.41 A) SWVs of 1.0 µmol L^{-1} ACP at (3:1)(MnO_2:h-MoO_3)(5%)+GO(95%)/GCE) in pH 6.60 PBS with frequency 1.0 – 10.0 Hz; B) The influence of frequency on the peak current of ACP.

The square wave voltammetric response of varied concentrations of ACP was shown in Fig. 3.42 at bare GCE in pH 6.60 PBS. The oxidation peak current was increased by increasing of ACP in the concentration range from 0.6 µmol L^{-1} to 1.0 mmol L^{-1}. The calibration curves were shown in Fig. 3.43. The dynamic range of ACP on bare GCE was 0.6 µmol L^{-1} to 1.0 mmol L^{-1} while the linear dynamic range was 0.6 µmol L^{-1} to 600 µmol L^{-1} with equation $Ip = 0.0192\ c_{ACP} + 0.0427$ (R^2=0.9987) and LOD was 2.29 x 10^{-7} mol L^{-1}.

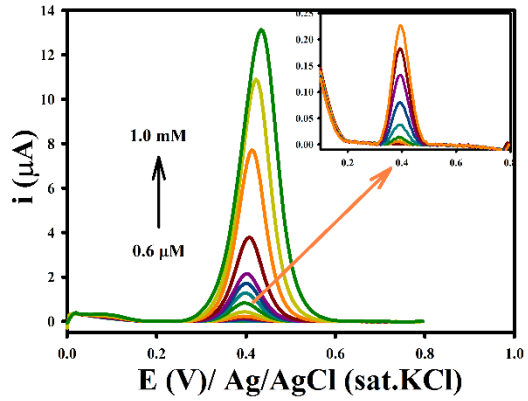

Figure 3.42 SWV of different concentrations of ACP A) dynamic range (0.6; 0.8; 1.0; 2.0; 4.0; 6.0;8.0; 10.0; 20.0; 40.0; 60.0; 80.0; 100.0; 200.0; 400.0; 600.0; 800.0; 1000 µM ACP) and B) linear calibration range (0.6-600 µM ACP) for ACP on bare GCE.

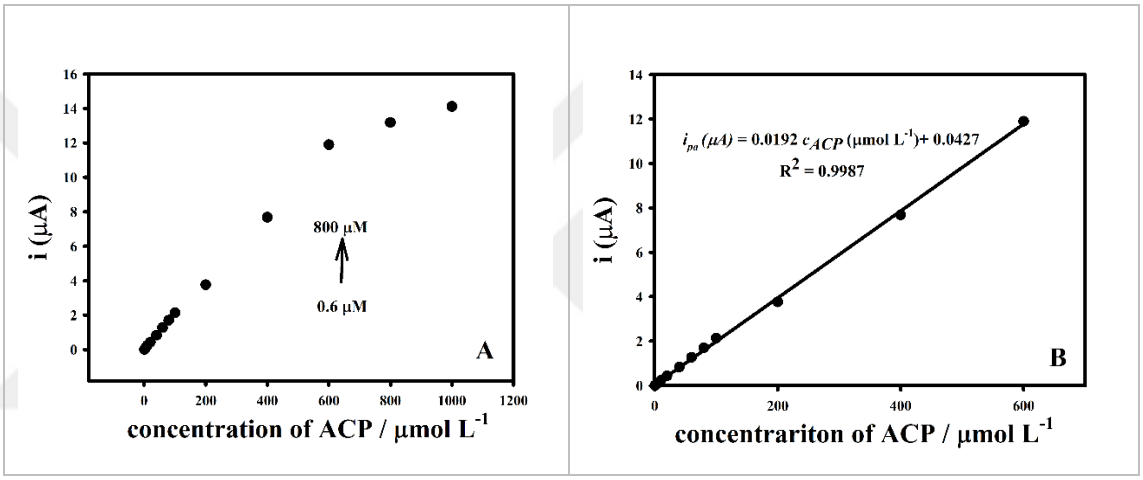

Figure 3.43 Plots for i_{ACP} vs. c_{ACP}. a) dynamic range (0.6; 0.8; 1.0; 2.0; 4.0; 6.0;8.0; 10.0; 20.0; 40.0; 60.0; 80.0; 100.0; 200.0; 400.0; 600.0; 800.0; 1000 µM ACP) and b) linear calibration range (0.6-600 µM ACP) for ACP on bare GCE.

Square wave voltammetric response of GO/GC electrodes in pH 6.60 PBS in absence and presence of various concentrations ACP were shown in Fig. 3.44.

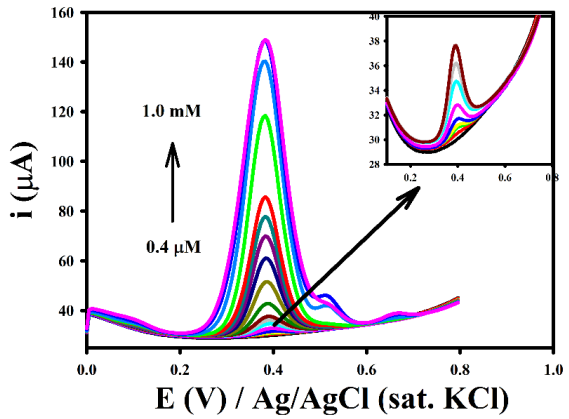

Figure 3.44 SWV of different concentrations of ACP A) dynamic range (0.4; 0.6; 0.8; 1.0; 2.0; 4.0; 6.0;8.0; 10.0; 20.0; 40.0; 60.0; 80.0; 100.0; 200.0; 400.0; 600.0; 800.0; 1000) and B) linear calibration range (0.4-100 µM ACP) for ACP on GO/GCE.

The calibration graphs were shown in Fig. 3.45. The dynamic range of ACP on GO/GCE is ranged from 0.4 µmol L^{-1} to 1.0 mmol L^{-1}. The linear dynamic range of ACP on GO/GCE is 0.4 µmol L^{-1} to 100 µmol $L^{-1}$with equation Ip=0.4682 c_{ACP}+ 0.5691 (R^2=0.9982).

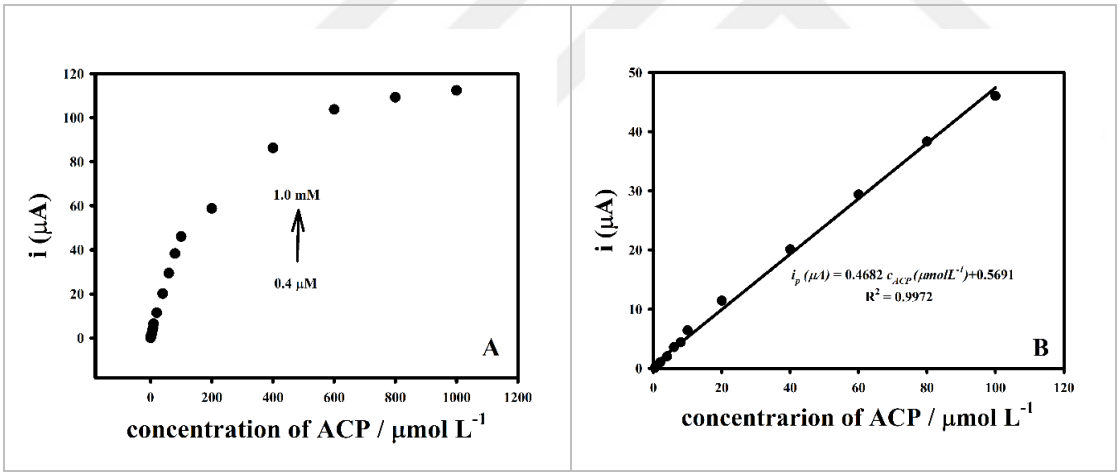

Figure 3.45 Plots for i_{ACP} vs. c_{ACP}. a) dynamic range (0.4, 0.6, 0.8, 1, 2, 4, 6, 8, 10,20,40, 60, 80, 100, 200, 400, 600, 800,1000 µM ACP) and b) linear dynamic calibration range (0.4-100 µM ACP) for ACP on GO/GCE.

Under the optimum SWV conditions, the oxidation peak current of ACP was increased on its concentration in dynamic range from 0.06 µmol L^{-1} to 400.0 µmol L^{-1} (Fig. 3.46). On the other hand, the calibration curves for the oxidation peak current versus the concentrations of ACP were constituted with two different linear parts at (3:1)(MnO_2:MoO_3)(5%)+GO(95%)/GCE (Fig. 3.47B): the first linear part was obtained between 0.06 µmol L^{-1} to 10.0 µmol L^{-1} with linear regression equation of $i_{pa}(\mu A)$= 1.9868 C_{ACP} $(\mu molL^{-1})$ - 0.3217 (R^2=0.9981) and second linear

part was establihed between 20.0 µmol L^{-1} – 80.0 µmol L^{-1} with a linear regression equation of $i_{pa}(\mu A)$= 1.2912 C_{ACP} $(\mu molL^{-1})$ + 11.923 (R^2=0.9947). The LOD) was obtained as 0.0133 µmol L^{-1}, which calculated by using the LOD=3.3S/m. In this equation, m is the slope of the calibration graph and S is the standard deviation of the response for blank solution.

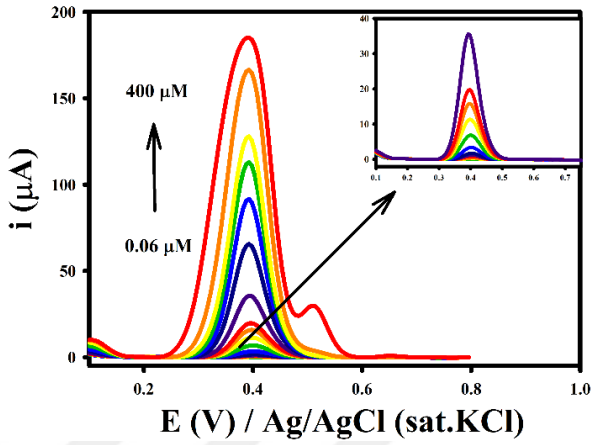

Figure 3.46 SWV of different concentrations of (0.06, 0.08, 0.1, 0.2, 0.4, 0.6, 0.8, 1, 2, 4, 6, 8, 10,20,40, 60, 80, 100, 200, 400 µM ACP) ACP on (3:1)(MnO_2:h-MoO_3)(5%)+GO(95%)/GCE)

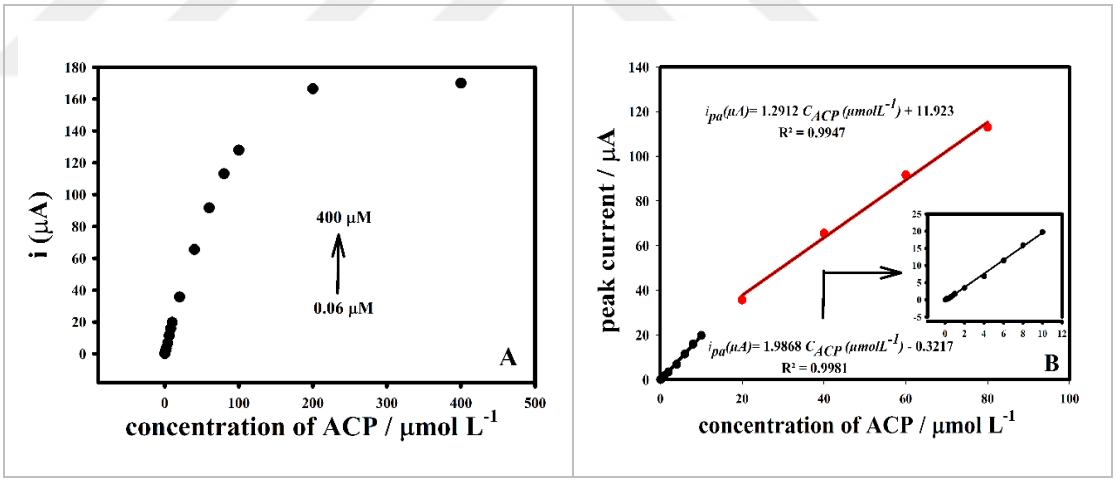

Figure 3.47 Plots for i_{ACP} vs. c_{ACP}. a) dynamic range (0.06, 0.08, 0.1, 0.2, 0.4, 0.6, 0.8, 1, 2, 4, 6, 8, 10,20,40, 60, 80, 100, 200, 400 µM ACP) and b) linear calibration range (0.6-80.0 µM ACP) for ACP on (3:1)(MnO_2:h-MoO_3)(5%)+GO(95%)/GCE)

A comparative calibration curve was formed by following the oxidation peak current depending on ACP concentration at bare GCE, GO/GCE and (3:1)(MnO_2:h-MoO_3)(5%)+GO(95%)/GCE) in Fig. 3.48. As shown in calibration curve, (3:1)(MnO_2:h-MoO_3)(5%)+GO(95%)/GCE have highest activity and sensitivity towords oxidation of ACP, since it has the greatest slope among the obtained calibration curves.

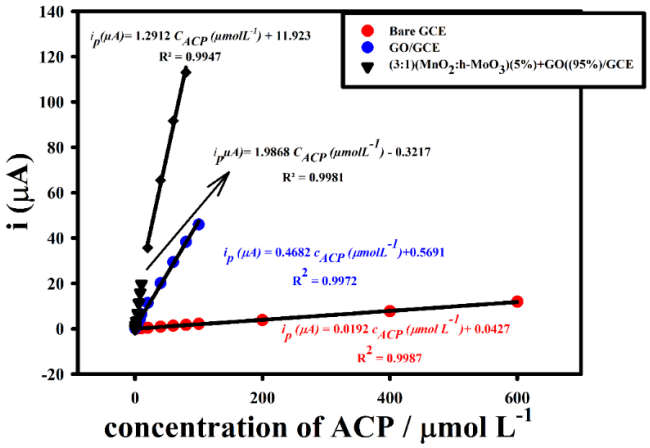

Figure 3.48 ACP oxidation calibration curves and related equations for bare GCE, GO/GCE, and (3:1)(MnO_2:h-MoO_3)(5%)+GO(95%)/GCE

Table 3.14 presents a comparison between the bare and the modified electrodes with regard to sensitivity, LOD, and linear range. For ACP, we were able to get high sensitivity, which was in accordance with the low detection limits. The results show that (3:1) (MnO_2:h-MoO_3)(5%)+GO(95%)/GCE provide sensitive determination of ACP.

Table 3.14 Analytical characteristics for determination of ACP at bare and modified electrodes.

Bare GCE	
Calibration Equation	$i_{pa}\ (\mu A)$ = 0.0192 $c_{ACP}\ (\mu mol\ L^{-1})$+ 0.427
Lineer Range	$6.0x10^{-7}$ M – $4.0x10^{-4}$M
LOD	$2.29x10^{-7}$ molL^{-1}
R^2	0.9987
GO/GCE	
Calibration Equation	$i_{pa}\ (\mu A)$ = 0.4682 $c_{ACP}\ (\mu mol\ L^{-1})$+ 0.5681
Lineer Range	$4.0x10^{-7}$ M – $4.0x10^{-4}$ M
LOD	8.89 $x10^{-8}$ molL^{-1}
R^2	0.9972
(3:1)(MnO_2:h-MoO_3)(5%)+GO(95%)/GCE)	
Calibration Equation	$i_{pa}\ (\mu A)$ = 1.9868 $c_{ACP}\ (\mu mol\ L^{-1})$+ 0.3217 $i_{pa}\ (\mu A)$ = 1.2912 $c_{ACP}(\mu mol\ L^{-1})$+ 11.923
Lineer Range	$6.0x10^{-8}$ M – $1.0x10^{-5}$ M $2.0x10^{-5}$ M – $8.0x10^{-5}$ M
LOD	$1.33x10^{-8}$ mol L^{-1}
R^2	0.9981 ; 0.9947

To compare tha obtained data with published paper in literature, the linear dynamic range and LOD values to detection of ACP were given in Table 3.15. The present work demonstrates that the (3:1)(MnO_2:h-MoO_3)(5%)+GO(95%)/GCE electrode is a highly selective and sensitive alternative for ACP sensor.

Table 3.15 Comparing variously modified electrodes to determine ACP.

Electrodes	**Mode**	**LR (μmol L^{-1})**	**LOD (mol L^{-1})**	**Reference**
Ag/PANI/PW12/CPE	DPV	0.066 – 92.9	$1.60x10^{-8}$	Kiaeefar, A. et. al., 2022
MWCNTs-doped poly (glycine) (p-gly)/ poly (acrylic acid) (PAA)	LSV	0.250-120	$8.00x10^{-8}$	Wei, Z. et al., 2019
Au@Fe-MOF/GCE	DPV	0.500–18	$1.20x10^{-7}$	Kavya, K. V. et. al., 2022
Graphene/polydopamine supported Au@Pt/Au nanoparticle	DPV	1.00 – 30.0	$3.10x10^{-7}$	Shi, L. et.al., 2020
(3:1)(MnO_2:h-MoO_3)(5%)+GO(95%)	**SWV**	**0.060 – 10.0 20.0 – 80.0**	**$3.83x10^{-8}$**	**Present study**

Reproducibility, repeatability, stability

The stability, repeatability, and reproducibility of the (3:1)(MnO_2:h-MoO_3)(5%)+GO(95%)/GCE were thoroughly examined by monitoring the oxidation peak of 2.0 μmolL^{-1} ACP with SWV in optimum conditions. The repeatability of developed (3:1)(MnO_2:h-MoO_3)(5%)+GO(95%)/GCE was studied by running forty successive SWV measurements of 2.0 μmol L^{-1} of ACP in pH 6.60 PBS. The SWV results provided excellent repeatability with 3.67 % of RSD. The RSD of the reproducibility were acquired from the SWV experiments on inter-day (n=5) and intra-day (n=5) with (3:1)(MnO_2:h-MoO_3)(5%)+GO(95%)/GC composite electrode for 2.0 μmol L^{-1} of ACP in pH 6.60 PBS. The inter-day and intra-day RSD values for 2.0 μmol L^{-1} ACP were 3.61 % and 2.65 % respectively (Fig. 3.49). These RSD values represent that the (3:1)(MnO_2:h-MoO_3)(5%)+GO(95%) modified GCE have high reproducibility. To estimate the stability of the (3:1)(MnO_2:h-MoO_3)(5%)+GO(95%)/GCE, it was used after being protected in the space of the

supporting electrolyte at room temperature. At the end of the 4 days, the electrode response maintained 96.2% of the orginal peak current value for 2.0 µmolL^{-1} ACP in pH 6.60 PBS indicating that the composite electrode retains stability over extended time periods.

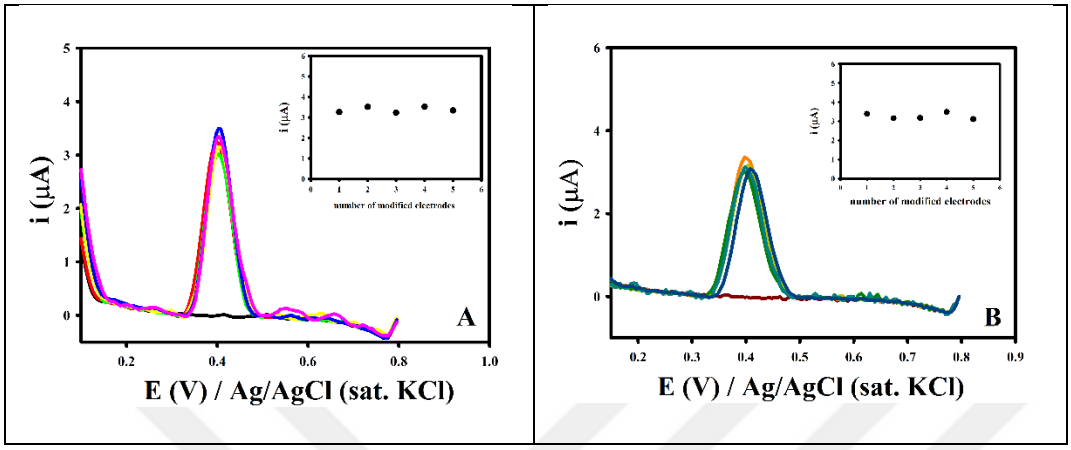

Figure 3.49 SWV studies on A) inter-day (n=5) and B) intra-day (n=5) with (3:1)(MnO_2:h-MoO_3)(5%)+GO(95%) for 2.0 µM ACP.

Interferences studies

The potential interference inorganic and organic compounds were studied in pH 6.60 PBS containing 2.0 µmol L^{-1} ACP at the (3:1)(MnO_2:h-MoO_3)(5%)+GO(95%)/GCE. As can be seen Table 3.16; the results show that the oxidation peak current of ACP was not significantly changed in the presence of Na^+, K^+, Ca^{+2}, Al^{+3}, Cl^-, SO_4^{2-} , CH3COO$^-$ and NO_3^- species when their concentration increased until to 1000-fold excess amount. It can be seen from the obtained results that the effects of 100-fold concentration of dopamine and epinephrine; 10-fold concentration of uric acid on 2.0 µmol L^{-1} ACP oxidation peak current were found to be less than 6% (Fig. 3.50). According to these results, (3:1)(MnO_2:h-MoO_3)(5%)+GO(95%)/GCE can be used to selective detection of ACP contents in real samples (Fig. 3.51).

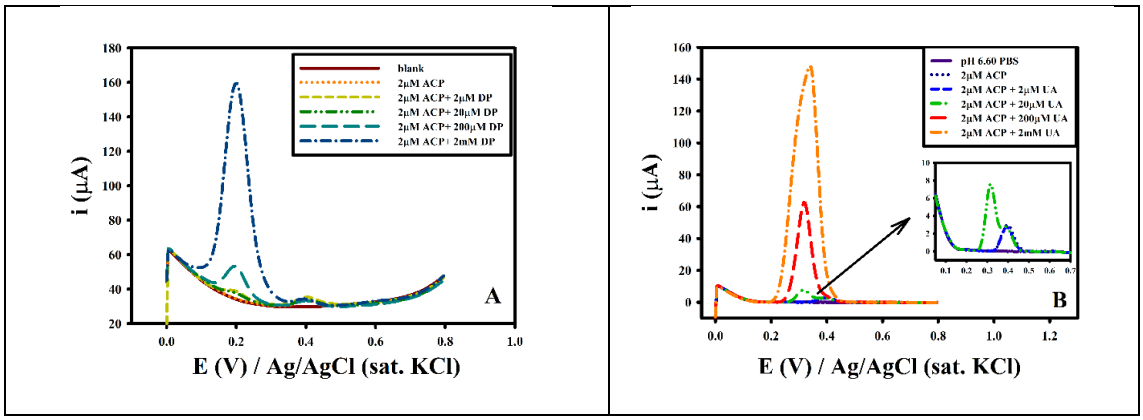

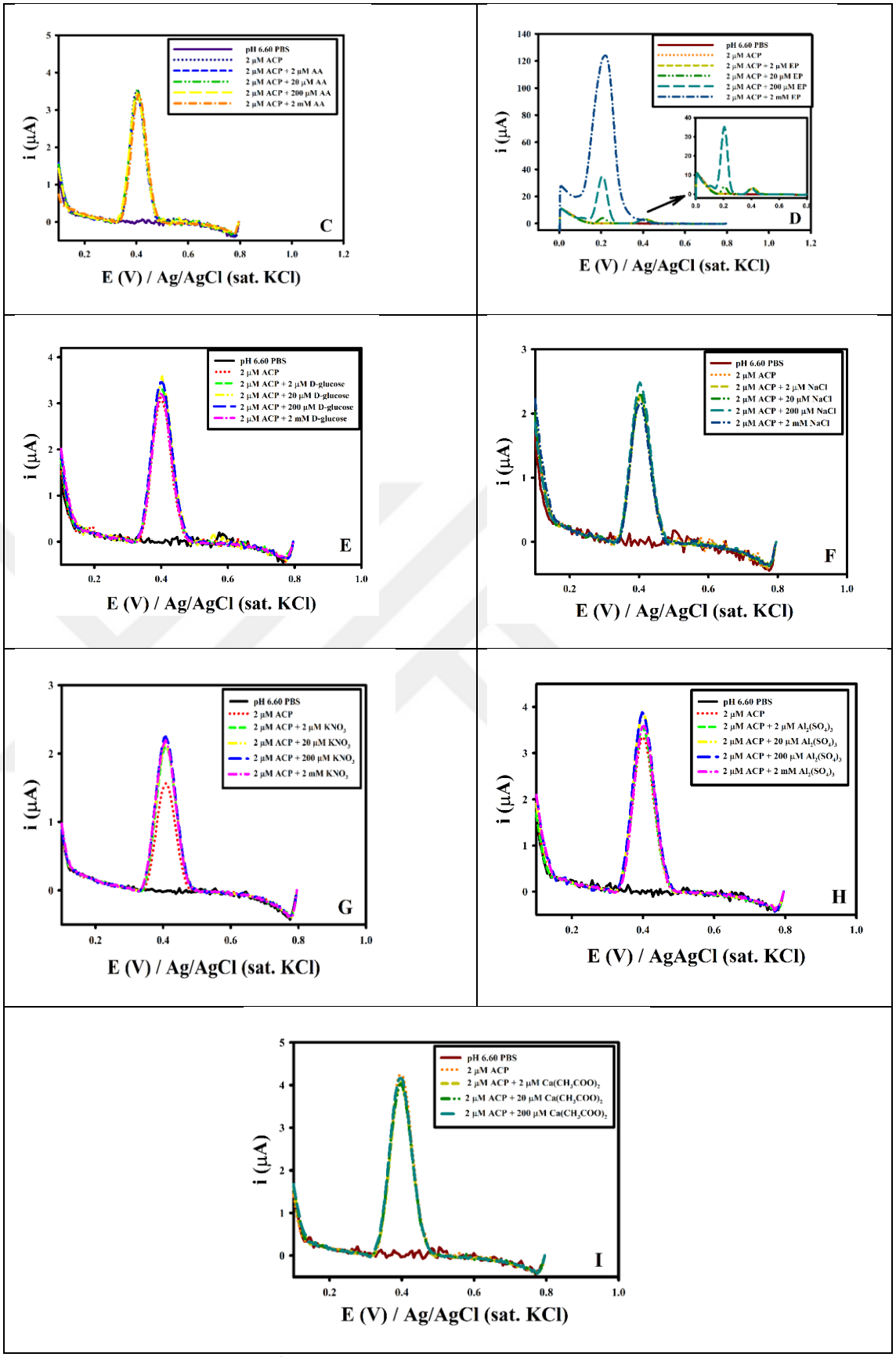

Figure 3.50 SWVs of 2.0 µmol L^{-1} ACP in the presence of different interfering species. A) Dopamine (DP), B) Uric Acid (UA), C) Ascorbic Acid (AA), D) D-glucose, E) Epinephrine (EP), F) NaCl, G) KNO_3, H) $Al_2(SO_4)_3$, I) $Ca(CH_3COO)_2$ at various concentration ratios on $(3:1)(MnO_2:MoO_3)(\%5)+GO(95\%)$/GCE.

Table 3.16 Relative (%) change of the analytical signal of ACP (2.0 μmol L^{-1}) in the pH 6.60 PBS.

Interfering species	Molar ratio ([Interferingspecies]/[ACP])	Change on the analytical signal of ACP (%)
Ascorbic acid	10	+1.95
	100	-1.23
	1000	-2.09
Dopamine	10	-4.56
	100	-25.65
	1000	-78.27
Glucose	10	+4.95
	100	+9.62
	1000	+1.17
Uric Acid	10	-67.36
	100	-
	1000	-
Epinephrine	10	+3.67
	100	-7.95
	1000	-81.39
Na^+	10	+1.27
	100	+5.60
	1000	+12.54
K^+	10	+4.28
	100	+5.89
	1000	+1.79
Ca^{2+}	10	-3.42
	100	-0.22
	1000	-8.03
Al^{3+}	10	+8.61
	100	+8.61
	1000	+6.18
Cl^-	10	+1.27
	100	+5.60
	1000	+12.54
NO_3^-	10	+4.28
	100	+5.89
	1000	+1.79
CH_3COO^-	10	-3.42
	100	-0.22
	1000	-8.03
SO_4^{2-}	10	+8.61
	100	+8.61
	1000	+6.18

Analytical application

To investigate the performance of the developed electrode in pharmaceutical sample applications, certain amount of sample was diluted in pH 6.60 PBS with the assistance of ultrasonication, filtered, and it was diluted in pH 6.60 PBS. The standard addition method was used to evaluate the performance of (3:1)(MnO_2:h-

MoO_3)(5%)+GO(95%)/GCE. The results were given in Table 3.17. The recovery values were obtained 103.4% and 101.3% for the ACP samples. The relative standard deviation (RSD) was less than 5.0%. These results suggest that the application of a (3:1)(MnO_2:h-MoO_3)(5%)+GO(95%)/GC electrode for the determination of ACP concentration in pharmaceutical samples.

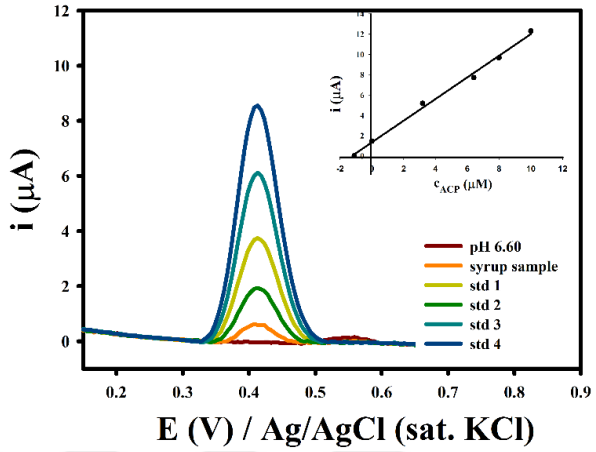

Figure 3.51 SWs for standart addition method of rutin determination in syrup sample. Inset: Related calibration curve for ACP.

Table 3.17 Determination of ACP in syrup by SWV.

Sample	Added (µmol L^{-1})	Found (µmol L^{-1})	Recovery(%)
syrup	3.20	3.31	103.4
	6.40	6.48	101.3

3.3 Simultaneous Determination of Acetaminophen and Tryptophan

3.3.1 Preparation of graphene oxide Modified GCE

Prepared as described in section 3.2.1.

3.3.2 Preparation of GO and $NiMoO_4$ Modified GCE

$NiMoO_4$ hybrid metal oxide materials with different ratios were successfully synthesized. Then GO with including different ratios $NiMoO_4$ suspension was prepared. A 10 µL of suspension was dropped on a GCE surface. At 70 °C for one hour, the solvent (DMF) of the solution on the GCE surface was evaporated.

3.3.3 Surface Characterizations of Modified Electrodes

SEM, EDX and XRD studies of modified electrdodes

The morphology of GO, $NiMoO_4$, and $NiMoO_4$+GO nanocomposite were investigated SEM. The Fig. 3.52A shows that SEM image of GO which wrinkles and folds in exfoliated GO sheets are typical of single-layer sheets. The SEM image of $NiMoO_4$ reveals a the 'cauliflower' like grains are made up of aggregated nano-size particles with numerous pores (Fig. 3.52B) (Jinlong, L. et.al, 2016). $NiMoO_4$+GO nanoparticles have the appearance of clustered structure and can be described as cottony structure (Fig. 3.52C). The higher magnification of nanocomposite shows the consisting of highly interconnected porous of layers that overlap with each other (Fig. 3.52D). In adition, EDX spectrum was demonstrated the presence of C, O, Ni and Mo atoms in structure of $NiMoO_4$+GO nanocomposite Fig. 3.52E.

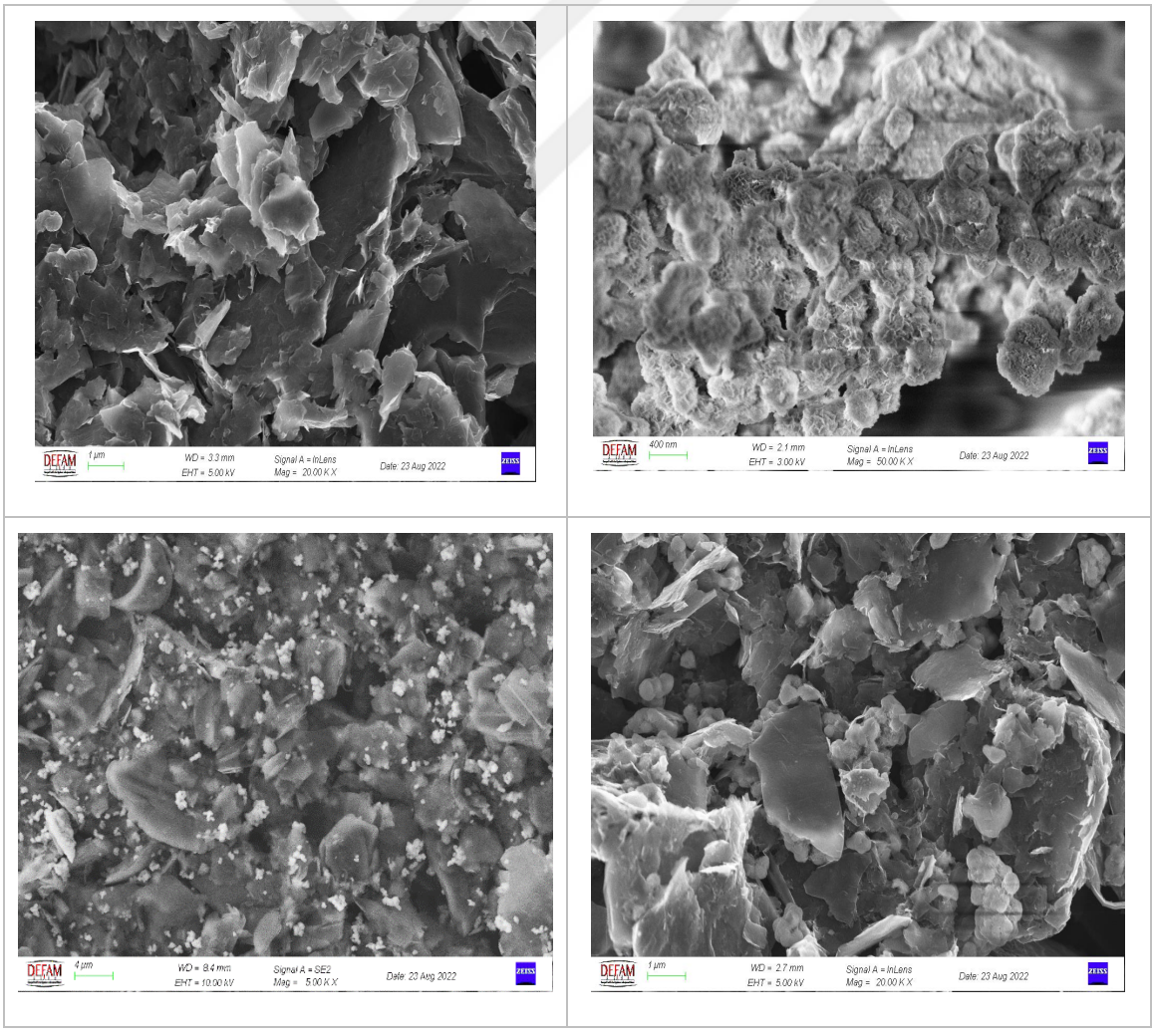

Element	Weight	Atomic %
C	85.6	91.25
O	9.76	7.83
Mo	1.77	0.24
Ni	3.11	0.68

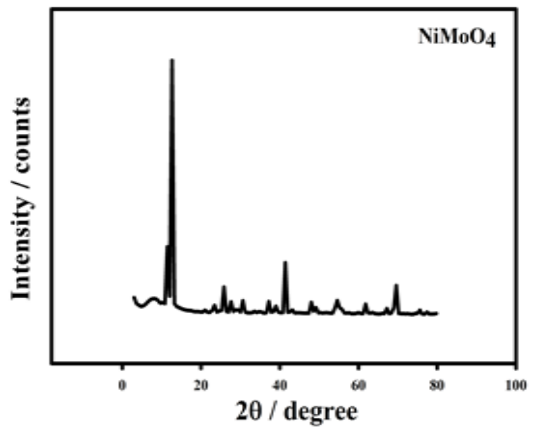

Figure 3.52 SEM images of (A) $NiMoO_4$, (B) GO), (C) NiMoO4(5%)+GO(95%)/GCE with 5000 magnitude, (D) $NiMoO_4$(5%)+GO(95%)/GCE with 20000 magnitude, (E) EDS resulf of $NiMoO_4$(5%)+GO(95%)/GCE and (F) XRD pattern of $NiMoO_4$ nanorods.

The crystal phase and structure of $NiMoO_4$ nanorods were investigated by XRD. Fig. 3.52F shows the diffraction pattern of $NiMoO_4$ nanorods prepared at 180 °C. Strong peaks at 10.72, 27.08 and 29.64 prove the presence of $NiMoO_4$, but the crystal structure is difficult to determine since metal molybdate hydrates tend to precipitate in weakly crystal forms (Liu et.al., 2013; Brito and Barbosa 1997). $NiMoO_4xH_2O$ crystal structure is currently not certain. As a result, the XPS method was utilized to determine the chemical structure of the hybrid material. It was determined that Ni^{2+} and Mo^{6+} in the structure were in the $NiMoO_4$ structure. which is compatible with XRD results.

XPS and EIS Studies of Modified Electrodes

The chemistry of $NiMoO_4$ was revealed by XPS (Fig. 3.53). Fig. 3.53A was shown the survey spectrum and indicate the presence of Ni, Mo and O atoms in the structure of the newly synthesized $NiMoO_4$. The high resolution spectrum of Ni 2p displays two main peaks at 856.2 and 873.9 eV corresponding to Ni $2p_{3/2}$ and Ni $2p_{1/2}$, respectively. These two main peaks are followed by two shakeup satellite peaks, which are indicated as "sat." The 17.7 eV gap between these two major peaks is compatible with the Ni^{2+} oxidation state present in $NiMoO_4$. (Sun P. et.al., 2017) (Fig. 3.53B). Furthermore, the presence of Mo^{6+} in molybdate was demonstrated by the presence of two peaks in the Mo 3d spectra with binding energies of 232.8 and 235.8 eV, corresponding to Mo $3d_{5/2}$ and Mo $3d_{3/2}$, respectively (Fig. 3.53 C) (Zhang, Z. Et.al. 2015). Additionally, a peak at 531.6 eV is observed in the O 1s

spectra, which is characteristic of a metal-oxygen bond (Yao, J. et.al. 2014). The above results were proved the successful synthesis of $NiMoO_4$.

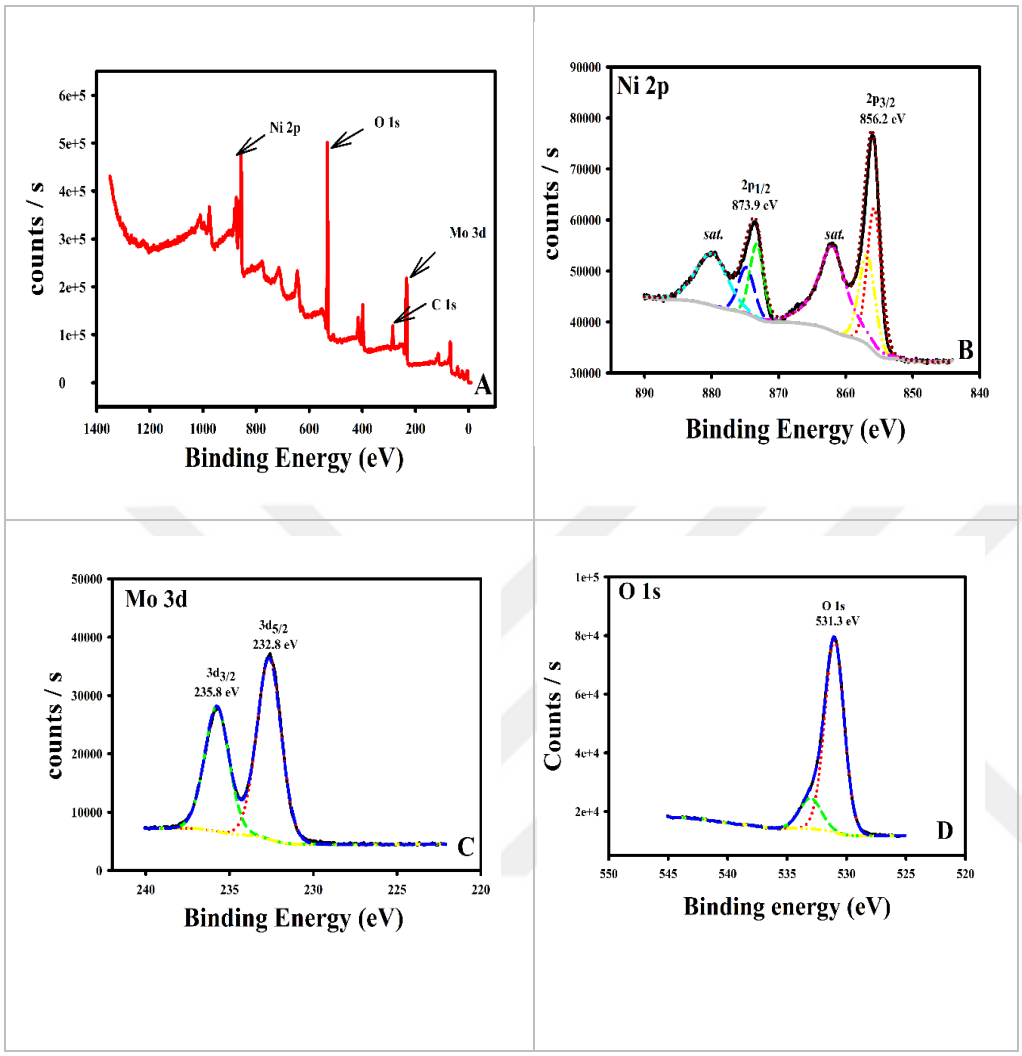

Figure 3.53 XPS spectra of $NiMoO_4$ (A) survey spectrum, (B) Ni 2p spectrum; (C) Mo 3d spectrum and (D) O 1s spectrum.

The results of EIS were obtained in the presence of 5 mM $K_3[Fe(CN)_6]/K_4[Fe(CN)_6]$ containing 0.1 M KCl solution on bare GCE, GO/GCE, (5%)MoO_4+(95%)GO/GCE, and (5%)$NiMoO_4$+(95%)GO/GCE, were shown in Fig. 3.54A . The impedance circuit consists the warburg impedance (W), the solution resistance Rs, the constant phase element (CPE or Q) and the charge transfer resistance Rct. The semicircle region (R_{ct}) is related to the charge transfer resistance in the electrolyte (Yousefipour, K. et.al., 2022). The Rct value that was obtained for the bare GCE was higher than the Rct values that were obtained for the other modified electrodes. These findings indicated that the synergistic impact of

GO with $NiMoO_4$ hybrids efficiently enhanced the electron transfer rate of the electrode.

It was clearly obsrved in Fig. 3.54 B that GCE have a large electron transfer resistance of about 217ohm. The Rct value for the bare GCE is higher than the Rct values obtained with **GO/GCE and ($NiMoO_4$)(5%)+GO(95%)/GCE**. The Rct values of **GO/GCE and ($NiMoO_4$)(5%)+GO(95%)/GCE** were found very close to each other as given in Table 3.18. The composite electrodes Rct data reflects a relatively fast charge transfer taking place compared with the bare GCE.

The active surface area was calculated according to Randles-Sevcik equation (eq.1) mentioned in section 3.1.4 above, from the slope of I_p *vs* $v^{1/2}$, the EASA values of the bare GC, GO/GC and **($NiMoO_4$)(5%)+GO(95%)/GC** electrodes were calculated 0.073, 0.103 and 0.206 cm^2 respectively. These results show a significant improvement in surface area after modification with **($NiMoO_4$)(5%)+GO(95%)/GC** nano composite.

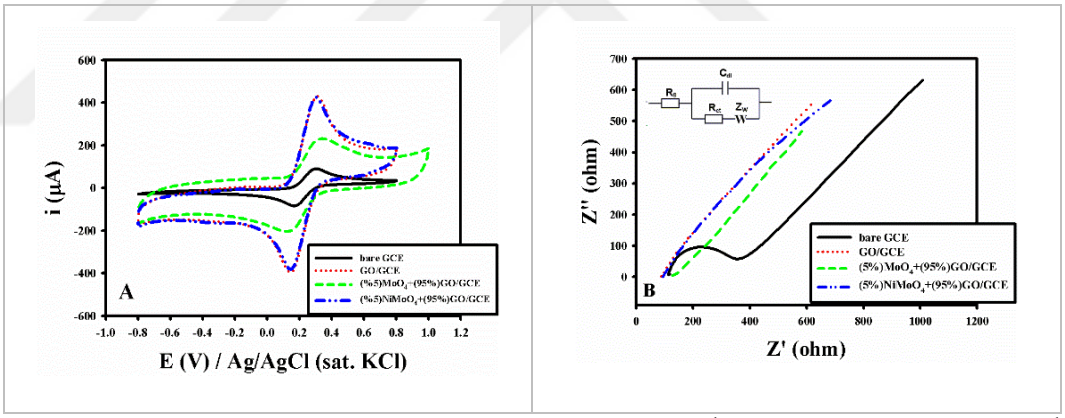

Figure 3.54 A) CVs of bare and modified GCE, in 0.1 mol L^{-1} KCl solution + 5.0 mmol L^{-1} $K_3[Fe(CN)_6]/K_4[Fe(CN)_6]$ at 50 mV s^{-1}. scan rate. (B) the bare and modified electrodes Nyquist plots.

Table 3.18 The Rs, Rct, CdI and W values of bare and modified electrodes.

	Bare GCE	**GO/GCE**	**($NiMoO_4$)(5%)+GO(95%)/GCE**
Rs	115Ω	91.4Ω	96.2 Ω
Rct	217Ω	36.8 nΩ	77.3 nΩ
CdI (mF)	1.83	1.75	1.63
W(mMho)	1.41	5.16	4.93

3.3.4 Voltammetric Behaviour of ACP and TRP at Bare and Modified Elecrodes

The electrochemical behavior of 0.1 mmol.L^{-1} ACP and TRP were investigated in pH 7.0 PBS at bare GCE, GO/GCE, (MoO_4)(5%)+GO(95%)/GCE, ($NiMoO_4$)(5%)+GO(95%)/GCE, (NiV_2O_8)(5%)+GO(95%)/GCE and (ZrO_2+CeO_2)(5%)+GO(95%)/GCE electrodes. Obtained CVs were shown in Fig. 3.55. A quasireversible electrochemical behavior was observed at 415 mV for oxidation and 320 mV for reduction reaction for ACP, while a irreversible electrochemical behavior was observed at about 700 mV for TRP oxidation almost at all composite electrodes. The peak currents and peak potentials were given in Table 3.19 for both ACP and TRP on all electrodes. The peaks current were enhanced by modification of GCE while the peak potentials shifted towards low positive potentials for both oxidation and reduction reactions. The improved peak characteristics were demostrated that an electrocatalytic activity was proved by modification of GCE with only GO and metal oxide species. On the other hand, the best electrocatalytic activity was obtained by monitoring the oxidation peak current at $NiMoO_4$ - GO composite electrode (Table 3.19). Therefore, the composite of $NiMoO_4$ - GO was prefered for future studies and the optimization studies were performed by observing the oxidation peaks of both ACP and TRP.

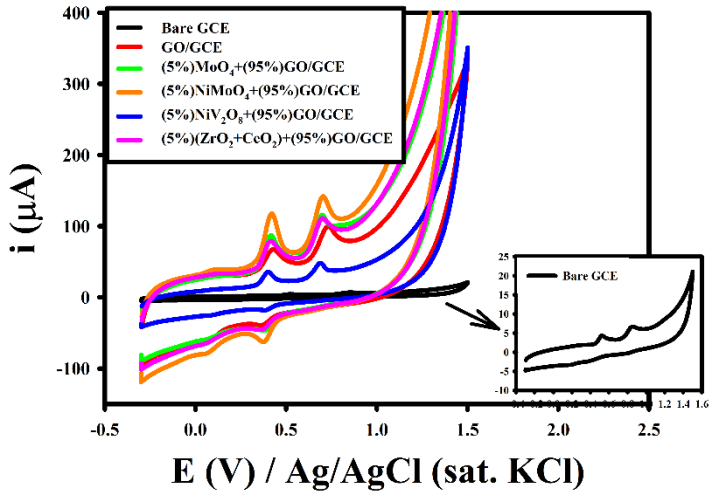

Figure 3.55 CVs of 0.1 mM ACP and TRP oxidation at bare GCE and modified GC elctrodes in pH: 7.00 PBS.

Table 3.19 Peak values of ACP and TRP oxidation at bare and modified electrodes

Electrode	ACP				TRP	
	I_a (µA)	E_a (V)	I_c (µA)	E_c (V)	I_a (µA)	E_a (V)
Bare GCE	1.820	0.521	-	-	2.074	0.847
GO/GCE	27.252	0.428	8.674	0.320	36.493	0.729
(5%)(MoO_4)+(95%)GO/GCE	39.488	0.414	14.212	0.384	35.621	0.694
(5%)($NiMoO_4$)+(95%)GO/GCE	**64.373**	**0.420**	**23.799**	**0.380**	**54.351**	**0.699**
(5%)(NiV_2O_8)+(95%)GO/GCE	16.933	0.400	4.387	0.388	17.037	0.686
(5%)(CeO_2+ZrO_2)+(95%)GO/GCE	32.975	0.412	11.368	0.372	37.55	0.698

Table 3.20 Peak values of ACP and TRP oxidation at bare and modified electrodes

Electrode	ACP				TRP	
	I_a (µA)	E_a (V)	I_c (µA)	E_c (V)	I_a (µA)	E_a (V)
Bare GCE	2.366	0.744	-	-	2.919	1.057
GO/GCE	27.252	0.428	8.674	0.320	36.493	0.729
(5%)(MoO_4)+(95%)GO/GCE	39.488	0.414	14.212	0.384	35.621	0.694
(5%)($NiMoO_4$)+(95%)GO/GCE	**64.373**	**0.420**	**23.799**	**0.380**	**54.351**	**0.699**

Effect of different ratios of nickel molybdate and graphene oxide ($NiMoO_4$+GO) suspension (from %1 to %10) on cyclic voltammetric behaviour of ACP and TRP

To obtain the best electrocatalytic nanocomposite surface which prepared from $NiMoO_4$ and graphene oxide containing suspentions using different ratios from 1% to 10% of $NiMoO_4$. Electrochemical behaviors of ACP and TRP both individual and simultanious were investigated composite electrodes which were prepared in these ratios. The individual and simultaneous CVs of ACP and TRP have shown Figure 3.56, 3.57 and 3.58 respectively. Also peak values of analytes have shown Table 3.21, 3.22 and 3.23. An irreversible oxidation peak was observed at about 0.71 V for 0.1 mmol L^{-1} TRP in pH 5.00 AcH/Ac buffer solution on all composite electrodes, while a quasireversible electrochemical behavior was performed for 0.1

mmol L^{-1} ACP in pH 7.0 PBS. The oxdation peak was appeared at about 0.43 V and reduction peak at about 0.38 V on all composite electrodes for ACP. On the other hand, the higher oxidation peak currents for both TRP and ACP were obatined for both TRP and ACP on 5% $NiMoO_4$ and 95% GO containing composite electrode. Thefore the on 5% $NiMoO_4$ and 95% GO containin composite electrode was choosen as optimum electrode for future studies.

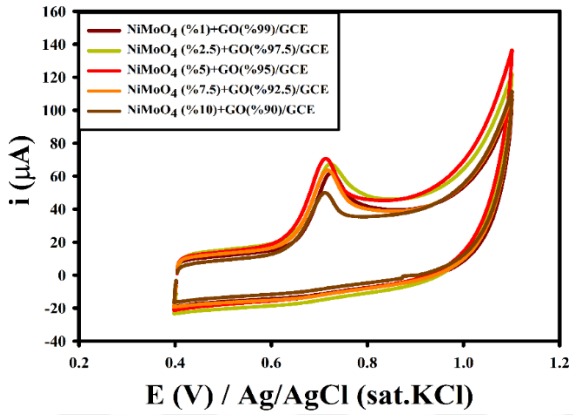

Figure 3.56

Figure 3. 56 Voltammetric behaviour of TRP at different ratios $NiMoO_4$+GO suspension (from %1 to %10)

Table 3-21 Peak current and potentials of TRP at different ratios $NiMoO_4$+GO modified electrodes

ELECTRODE	Tryptophan	
	$İ_a$ (µA)	E_a(V)
(%1)($NiMoO_4$)+(%99)GO/GCE	27.696	0.710
(%2.5)($NiMoO_4$)+(%97.5)GO/GCE	26.284	0.707
(%5)($NiMoO_4$)+(%95)GO/GCE	**43.185**	**0.721**
(%7.5)($NiMoO_4$)+(%92.5)GO/GCE	38.506	0.710
(%10)($NiMoO_4$)+(%90)GO/GCE	21.056	0.706

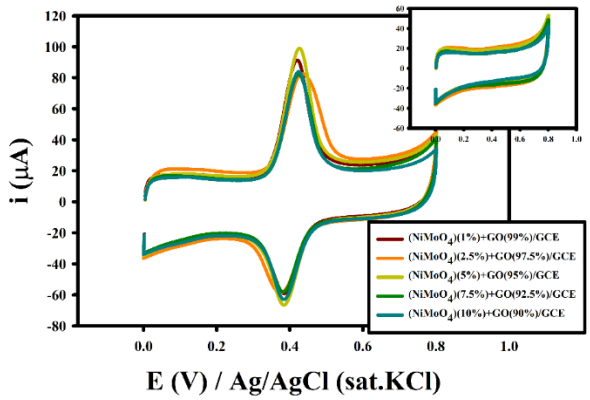

Figure 3.57 Voltammetric behaviour of ACP at different ratios $NiMoO_4$+GO suspension (from %1 to %10)

Table 3-22 Peak current and potentials of ACP at different ratios $NiMoO_4$+GO modified electrodes

ELECTRODE	Acetaminophen			
	$İ_a$ (µA)	E_a(V)	$İ_c$(µA)	E_c(V)
(%1)($NiMoO_4$)+(%99)GO/GCE	72.181	0.435	43.716	0.385
(%2.5)($NiMoO_4$)+(%97.5)GO/GCE	60.123	0.432	40.977	0.377
(%5)($NiMoO_4$)+(%95)GO/GCE	**78.617**	**0.426**	**50.596**	**0.385**
(%7.5)($NiMoO_4$)+(%92.5)GO/GCE	64.719	0.425	42.499	0.383
(%10)($NiMoO_4$)+(%90)GO/GCE	67.22	0.425	46.536	0.385

The simultaneous electrochemical behaviour of 0.1 mmol L^{-1} TRP and 0.1 mmol L^{-1} ACP were also studied on different ration $NiMoO_4$ containing composite electrode in pH 5.00 AcH/Ac buffer solution. A quasireversible electrochemical behaviour was observed for ACP at all composite electrodes whereas an irreversible electrochemical behaviour was occured for TRP at all electrodes. The peak characteristics as peak current and peak potentials for ACP and TRP were given in Table 3.23.

As seen in the Table 3.23, while the peak potentials were almost the same on all composite electrodes for both ACP and TRP, the highest peaks current height were observed in both analytes at the **(%5)($NiMoO_4$)+(%95)GO/GCE.**

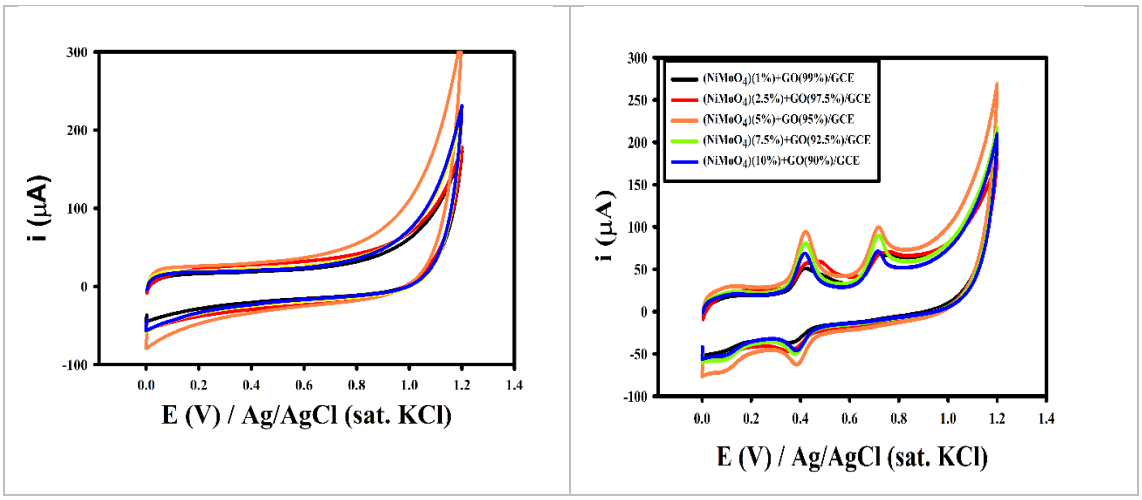

Figure 3.58 Voltammetric behaviour of ACP and TRP at different ratios $NiMoO_4$+GOsuspension (from %1 to %10)

Table 3.213 Peak current and potentials of ACP and TRP at different ratios $NiMoO_4$+GO modified electrodes

Electrode	ACP				TRP	
	I_a (µA)	**E_a (V)**	**I_c (µA)**	**E_c (V)**	**I_a (µA)**	**E_a (V)**
(%1)($NiMoO_4$)+(%99)GO/GCE	25.36	0.419	11.648	0.371	22.634	0.716
(%2.5)($NiMoO_4$)+(%97.5)GO/GCE	25.744	0.430	16.714	0.361	17.983	0.726
(%5)($NiMoO_4$)+(%95)GO/GCE	**59.152**	**0.421**	**29.312**	**0.387**	**45.348**	**0.716**
(%7.5)($NiMoO_4$)+(%92.5)GO/GCE	53.116	0.421	25.556	0.381	43.071	0.716
(%10)($NiMoO_4$)+(%90)GO/GCE	44.259	0.417	22.875	0.385	31.392	0.714

Effect of supporting electrolyte pH on ACP and TRP oxidation

The optimization of certain parameters is required in order to achieve an improved analytical signal for the chemicals. As previously stated in the introduction, protons play a role in the oxidation process of the analytes, and the oxidation behavior of these analytes is influenced by changes in the pH of the supporting electrolyte. As a result, the oxidation of ACP and TRP in supporting electrolytes was studied both individually and simultaneously.

The electrochemical behavior of 0.1 $mmolL^{-1}$ ACP and 0.1 $mmolL^{-1}$ TRP were also investigated in the pH range from 4.00 to 8.00 for both individually and simultaneously analytes containing conditions on **(%5)($NiMoO_4$)+(%95)GO/GCE**. As can be seen in Fig. 3.59 A, the individually electrochemical behaviour of ACP was studied in the pH range of 4.0 - 8.0. The oxidation peak (E_{pa}) and reduction peak potentials of ACP shifted toward negative values by increasing the pH value, indicating hydrogen ions were involved in the electrode reaction. In the Fig. 3.59B, it is seen that there is a linear change between peak potential and pH. The linear equations for both oxidation and reduction peaks of ACP were E_{pa} = - 0.0484 pH + 0.759 (R^2 = 0.9943) and E_{pc}= -0.0522 pH + 0.734 (R^2 = 0.9925) and. A slop of - 0.048 V pH^{-1} for oxidation peak which is close to the Nernstian value of 0.059 V, displayed the ratio of electrons and protons involves in

the electrode reaction could be 1:1. On the other hand, the highest peak current was observed at pH 7.0. Thus, pH 7.0 was choosen for future studies.

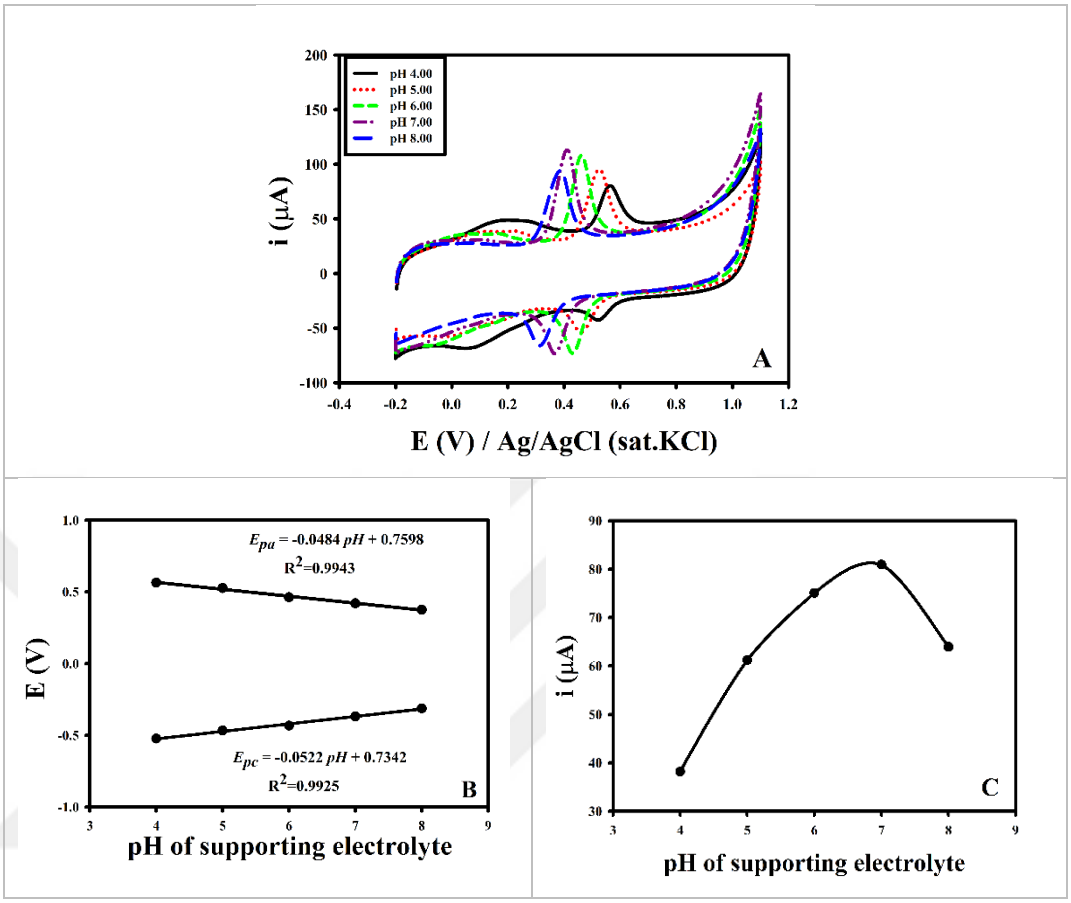

Figure 3.59 A) CVs of oxidation of 0.1 mM ACP at $(NiMoO_4)$(5%)+GO(95%)/GCE in various pH (4.00 to 8.0) at a scan rate of 50 mV/s. B) Plots of potential change versus supporting electrolyte pH for ACP oxidation and reduction. . C) Plots of current change vs. supporting electrolyte pH for ACP oxidation.

Additionally, as can be seen in Fig. 3.60 A, the individually electrochemical behaviour of TRP was studied in the pH range of 4.0- 8.0. The oxidation (Epa) and reduction peak potentials of TRP shifted toward negative values by increasing the pH value, indicating hydrogen ions were involved in the electrode reaction. In the Fig. 3.60 B, it is seen that there is a linear change between peak potential and pH. The linear equations for both oxidation peaks of TRP was Epa = -0.0383 pH + 0.978 (R^2 = 0.9923). The slope was found to be 38.3 mV pH^{-1}, which is quite near to the Nernstian value of 29.5 mV for a two-electron, one-proton reaction (Fig. 3.60 C) (Karimi-Maleh, H., et. al., 2014). On the other hand, the highest peak current was observed at pH 5.0. Thus, pH 5.0 was choosen for future studies.

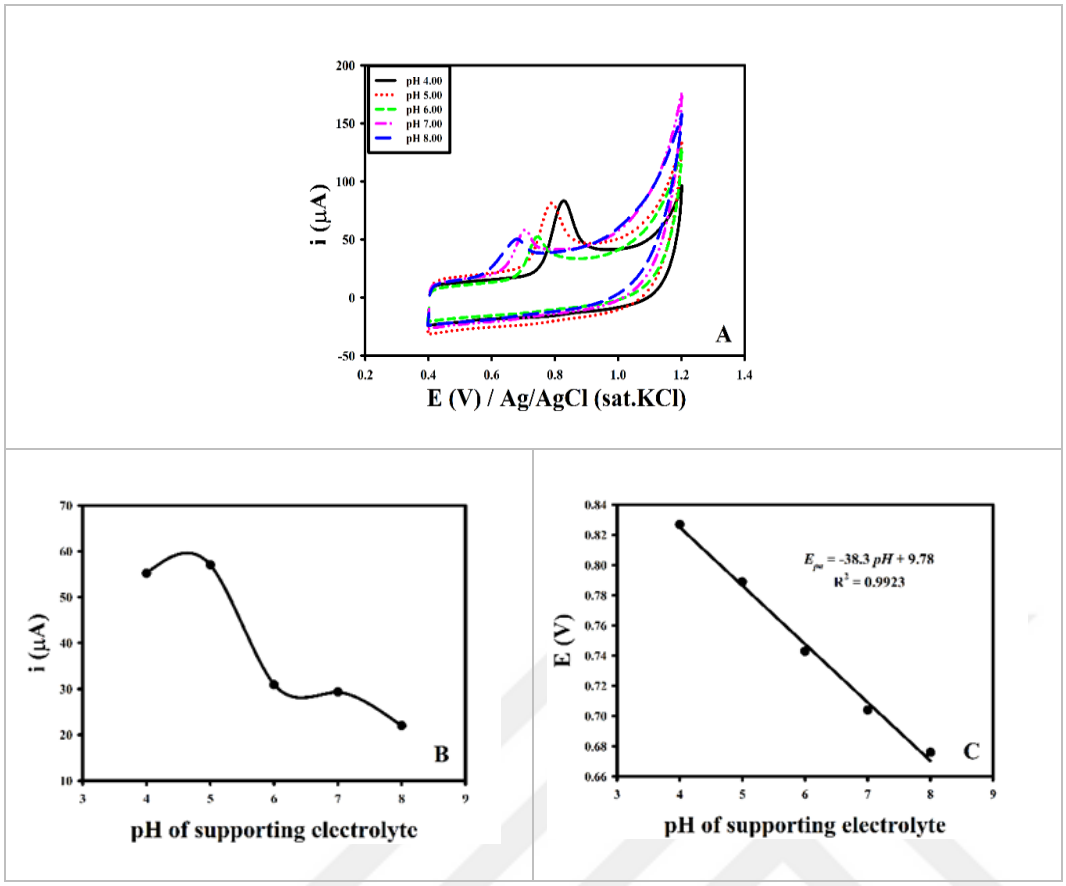

Figure 3.60 A) CVs of oxidation of 0.1 mM TRP at (NiMoO$_4$)(5%)+GO(95%)/GCE in various pH (4.00 to 8.0) at a scan rate of 50 mV/s. B) Plots of current change versus supporting electrolyte pH for TRP oxidation. C) Plots of potential change versus supporting electrolyte pH for TRP oxidation.

As can be seen Fig. 3.61 A the influence of pH on the peak currents and peak potentials of the electrochemical behaviour of 0.1 mmol L^{-1} ACP and 0.1 mmol L^{-1} TRP were investigated at (NiMoO$_4$)(%5)+GO(%95)/GC electrode by CV techniques in the pH range of 4.00 - 8.00. At a pH of 5.00, the AcH/Ac buffer solution reaches its highest peak current. Both the peak current of ACP and that of TRP were shown to decrease at high pH values (pH greater than 5.0) (Fig. 3.61B). On the other hand, when the pH of the supporting electrolyte solution was increased, the peak potential of both analytes shifted toward a more negative potential. That is indicating that the protons take part in the electrode reactions.

The linear relationship was established between the E_{pa} and the *pH* value of the solution with the linear regression equation as: *Epa* = -0.0371 *pH*+ 0.9788 (R^2= 0.9988) and *Epa* = -0.0491 *pH*+ 0.7684 (R2= 0.9964) for ACP and TRP, respectively (Fig. 3.61 C).

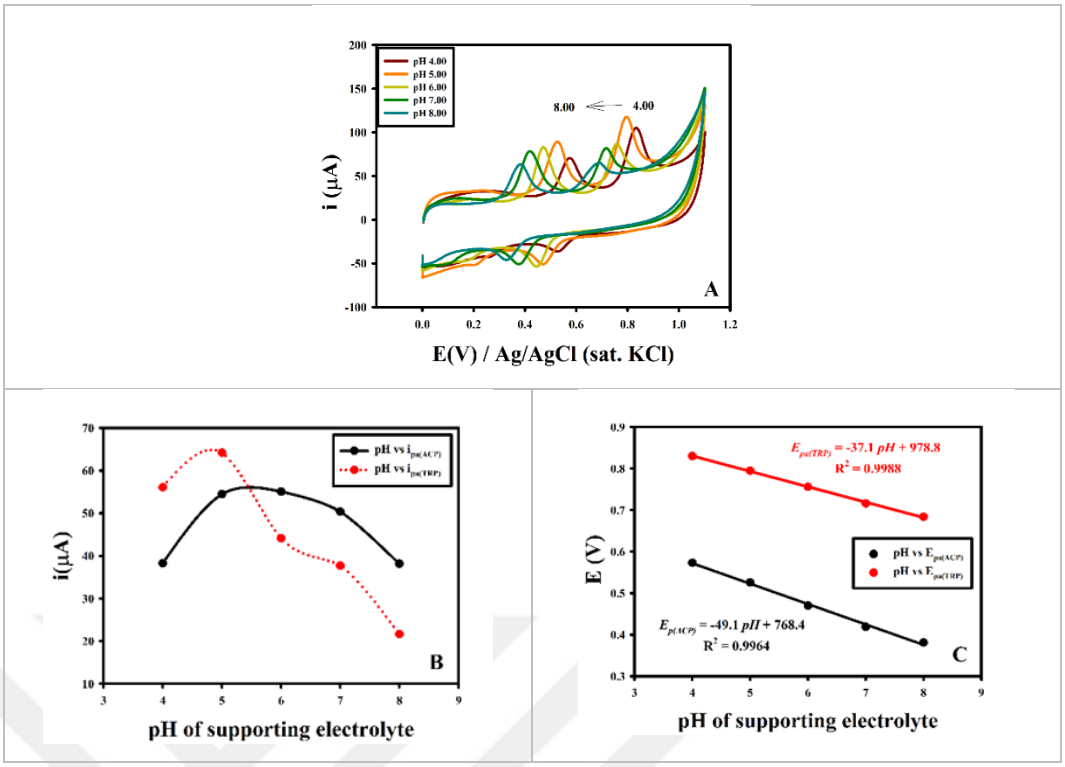

Figure 3.61) A CVs of oxidation of 0.1 mM ACP and TRP at $(NiMoO_4)(5\%)+GO(95\%)/GCE$ in various pH (4.00 to 8.0) at a scan rate of 50 mV/s. B) Plots of current change vs. supporting electrolyte pH for ACP and TRP oxidation. C) Plots of potential change vs. supporting electrolyte pH for ACP and TRP oxidation

Scan Rate Studies of ACP and TRP at $(NiMoO_4)(5\%)+GO(95\%)/GCE$)

CV was used to monitor the effect of the scan rate on the oxidation of ACP and TRP at $NiMoO_4(5\%)+GO(95\%)/GCE$. The influence of the scan rate (v) on peak current and peak potential of 0.1 mmol L^{-1} ACP and 0.1 mmol L^{-1} TRP, were studied over the range from 5 to 500 mV s^{-1} on $(NiMoO_4)(\%5)+GO(\%95)/GCE$ in pH 5.0 AcH/Ac buffer solution by cyclic voltammetry (Fig. 3.62A). The anodic and cathodic peak currents of ACP at $(NiMoO_4)(\%5)+GO(\%95)/GCE$ increased linearly with the square root of the scan rate (Fig. 3.62B), which suggests a diffusion-controlled electrochemical reaction occurs of ACP on the $(NiMoO_4)(\%5)+GO(\%95)/GCE$ surface. In a similar manner, it was determined that the electrode process of TRP was controlled by diffusion on $(NiMoO_4)(\%5)+GO(\%95)/GCE$ (Fig. 3.62 C).

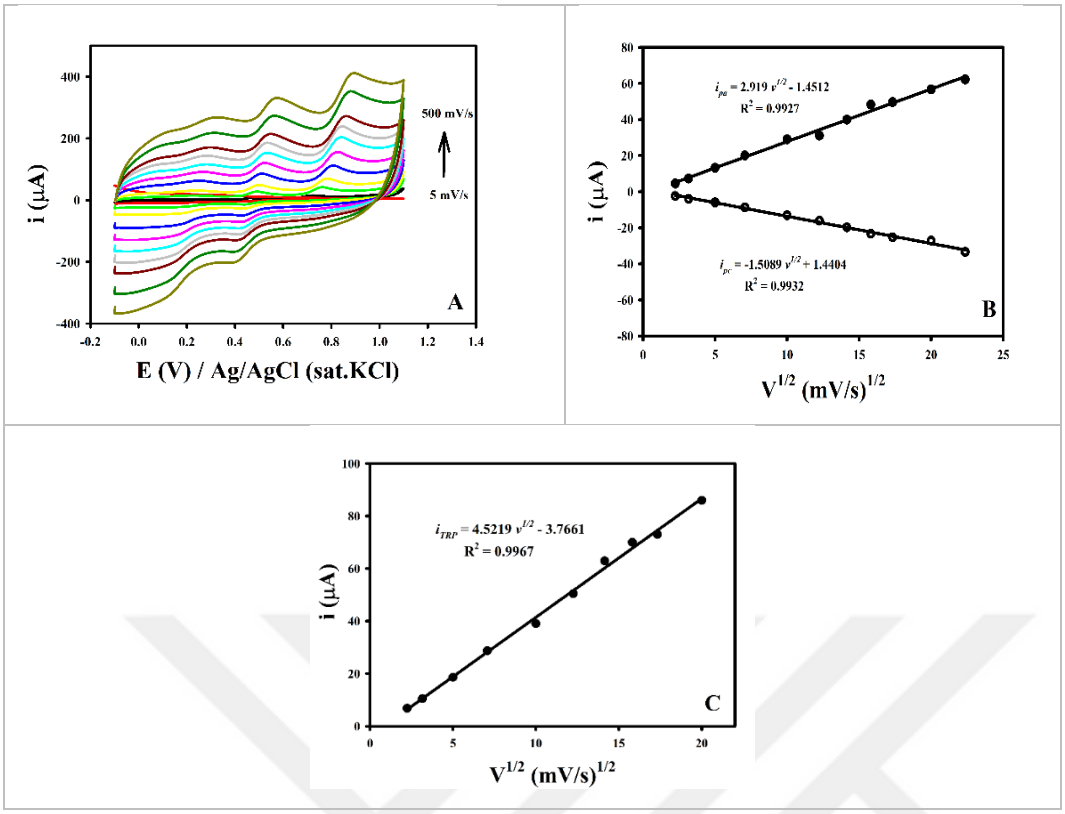

Figure 3.62 (A) CVs of the ($NiMoO_4$)(5%)+GO(95%)/GCE in pH 5.0 AcH/Ac containing 0.1 mM ACP at different scan rates (5–500 mV s−1), (B) the plots of I_{pa} and I_{pc} of ACP vs $V^{1/2}$, (C) the plots of Ipa and Ipc of TRP vs $V^{1/2}$

Square Wave Voltammetric Determination of ACP and TRP

Since SWV is more current sensitive and has higher resolution than CV, it was applied for both the individual and simultaneous determination of ACP and TRP. In following steps of the study, individual and simultaneous voltammetric determinations of ACP and TRP in an AcH/Ac buffer solution at a pH of 5.0 will be carried out.

The SWV parameter of amplitude was optimized by monitoring 1.0 µmol L^{-1} ACP and 10.0 µmol L^{-1} TRP oxidation peaks in pH 5.00 AcH/Ac at $NiMoO_4$(5%)+GO(95%)/GCE (Fig. 3.63 A), before studying the relationship between the oxidation peaks current of ACP and TRP with their concentrations in detail at each electrode by individual and simultaneous detections. The effect of W amplitude on oxidation peaks current were investigated in the range from 5mV to 60 mV (Fig. 3.63 B). The highest peak current was obtained with 30.0 mV amplitude values. Therefore this value was choosen for following studies.

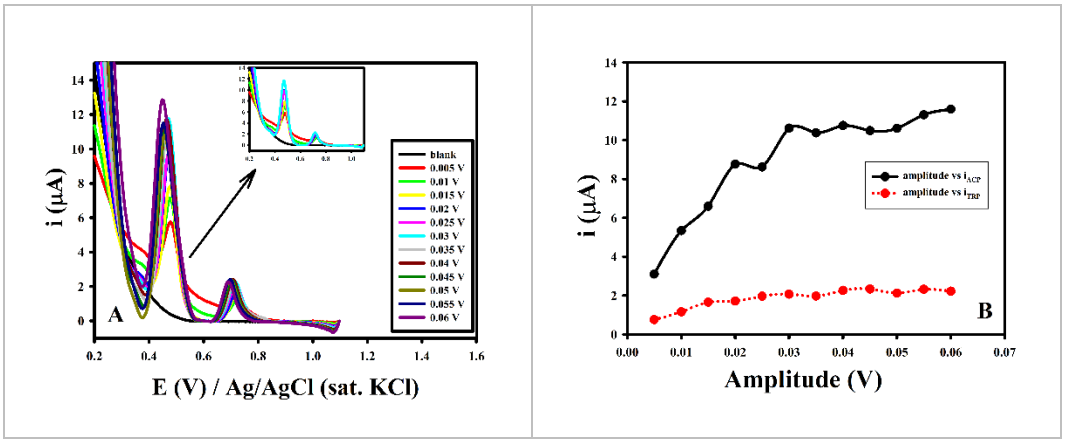

Figure 3.56 SWVs of 1.0 µM ACP and 10 µM TRP at ($NiMoO_4$)(5%)+GO(95%)/GCE) in pH 5.00 AcH/Ac with amplitude 5.0 – 60.0 mV/s; B) The influence of amplitude on the peak current of ACP and TRP.

The influence of SW frequency on the oxidation peak current of 1.0 µmol L^{-1} ACP and 10 µmol L^{-1} TRP in pH 5.00 AcH/Ac were examined in the range from 1.0 Hz to 7.0 Hz (Fig. 3.64 A) and 2.0 Hz frequency value was choosen for following studies.

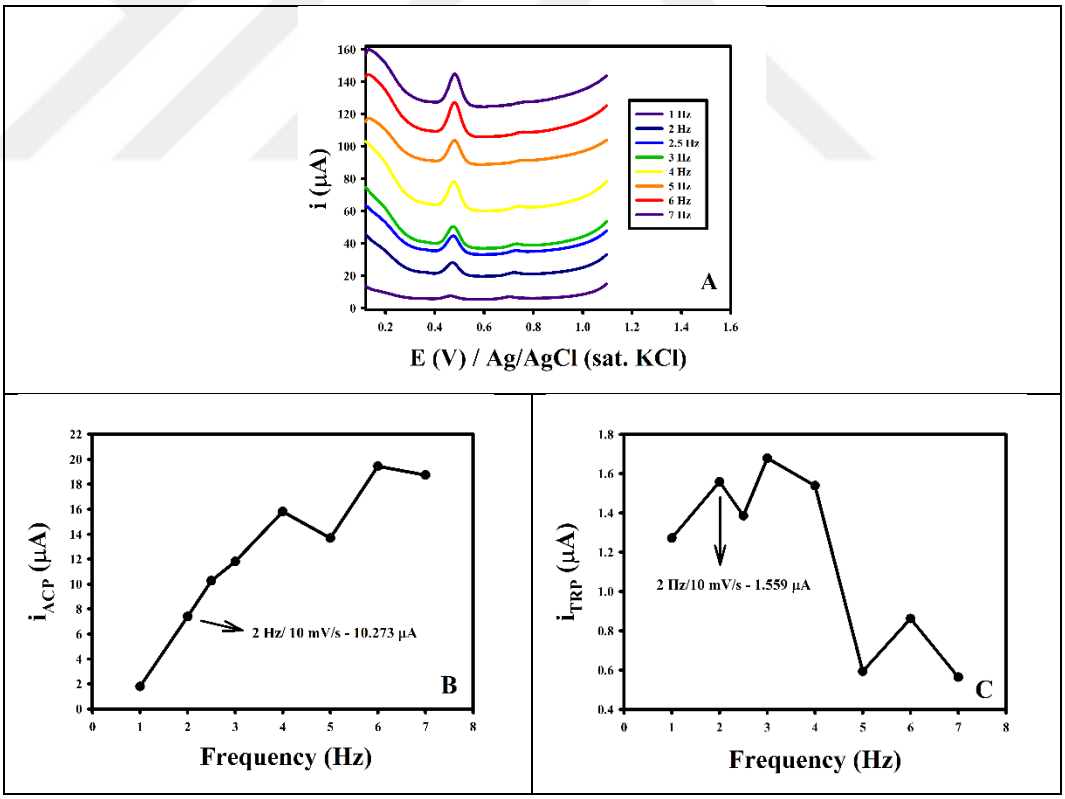

Figure 3.57 SWVs of 1.0 µM ACP and 10 µM TRP at ($NiMoO_4$)(5%)+GO(95%)/GCE) in pH 5.00 AcH/Ac with frequency 1.0 – 7.0 Hz; B) The influence of frequency on the peak current of B) ACP and C) TRP.

The values for the limit of detection were determined using a S/N=3 and calibration curves. The mean value of background current was determined by

analyzing 10 different voltammograms. The calculation of LODs was performed in order to estimate the values of linear ranges for all electrodes.

Initial studies with SWV was focused on the electrochemical respons of increasing ACP concentrations at bare GCE, GO/GCE and $NiMoO_4$ (5%)/GO(95%)/GCE in pH 7.0 PBS. The oxidation peak current of ACP was observed at 0.422 V and the peak current was linearly increased in the ACP concentration range from 1.0 µmol L^{-1} to 400.0 µmol L^{-1} at bare GCE. The linear regression equations were i_{pa} = 0.0159 c_{ACP} - 0.0185 with correlation coefficients of R^2=0.9968 (Fig. 3.65).

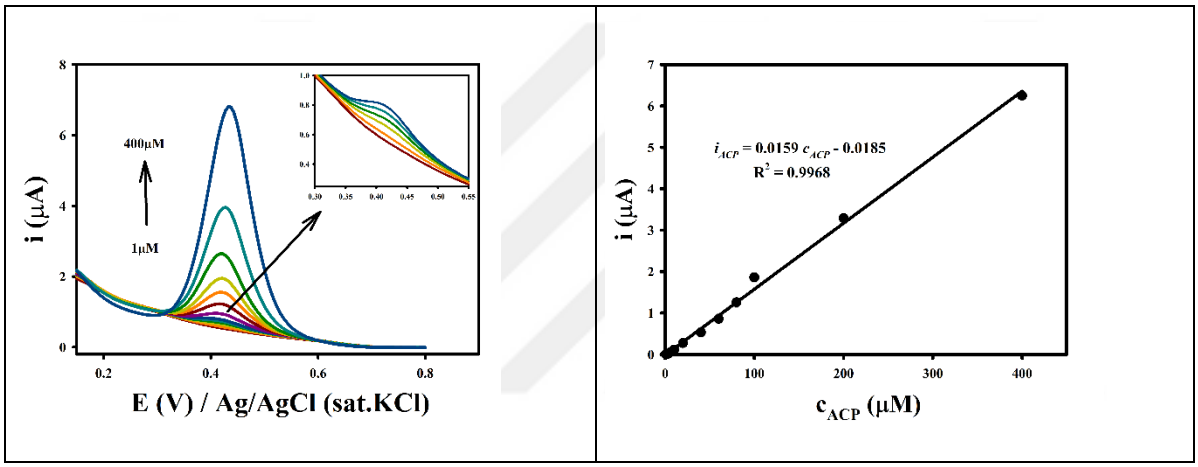

Figure 3.58 SWV of different concentrations of ACP (1.0; 2.0; 4.0; 6.0; 8.0; 10.0; 20.0; 40.0; 60.0; 80.0; 100.0; 200.0 and 400.0 µM) at bare GCE in the pH 7.00 PBS with 2 Hz ferquency and 30 mV amplitude. The linear curves of i_{ACP} vs c_{ACP}.

Fig. 3.66 A shows that SWV response of ACP in various concentrations in pH 7.0 PBS on GO/GCE. The calibration graphs were shown in Fig. 3.66 B-C. The dynamic range of ACP on GO/GCE is ranged from 0.2 µmol L^{-1} – 1.0 mmol L^{-1}. The linear range of ACP on GO/GCE is 0.2 µmol L^{-1}– 200.0 µmol L^{-1} with equation Ip_{acp} = 0.7302 c_{ACP} + 0.8383 (R^2=0.9964). The LOD was 0.181 µmol L^{-1}.

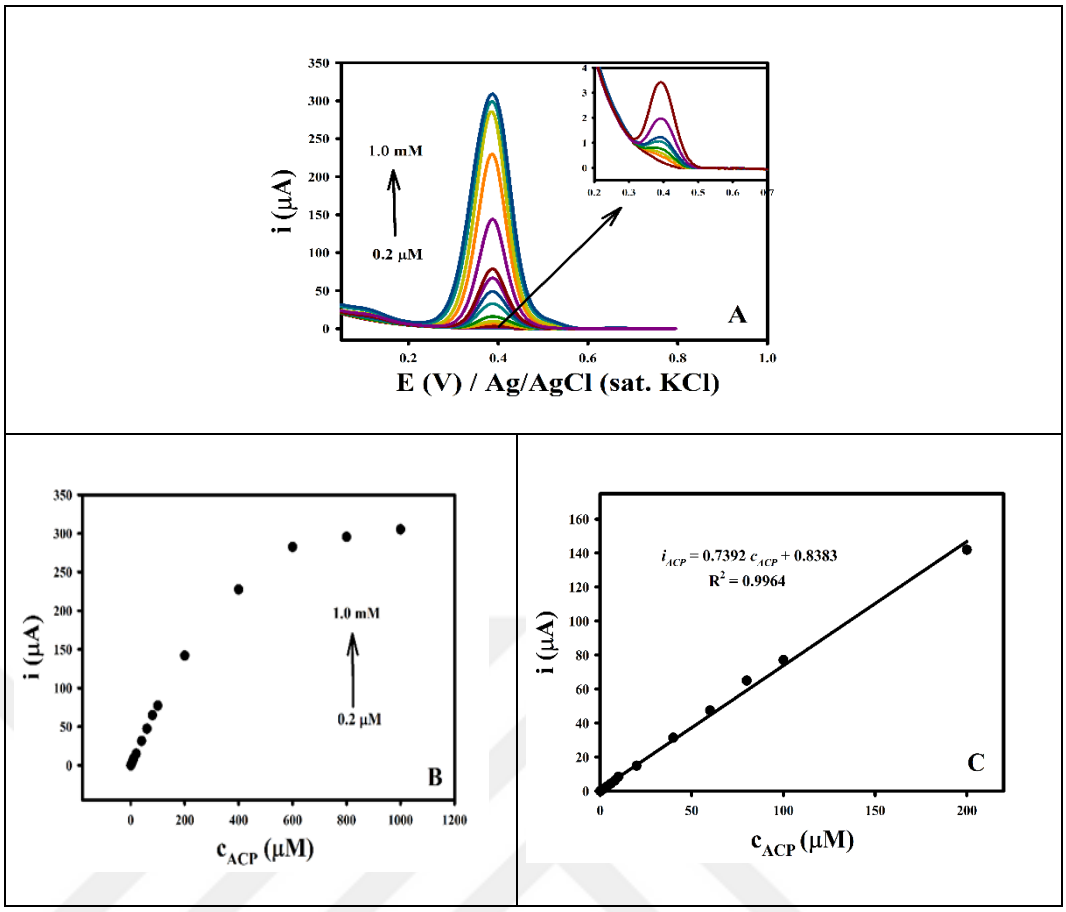

Figure 3.59 A) SWV of different concentrations of ACP (0.2; 0.4; 0.6; 0.8; 1.0; 2.0; 4.0; 6.0; 8.0; 10.0; 20.0; 40.0; 60.0; 80.0; 100.0; 200.0; 400.0; 600.0; 800.0 and 1000 µM ACP) B)Plots for ACP oxidation peak currents versus concentration of dynamic range (0.2 µM – 1.0 mM ACP) and C) linear calibration range (0.2 µM – 200.0 µM) at GO/GCE in the pH 7.00 PBS with 2 Hz ferquency and 30 mV amplitude.

In addition Fig. 3.67A demonstrated that the oxidation peak current of ACP was increased by inceasing of its concentration in the range from 0.1 µmol L^{-1} to 800.0 µmol L^{-1} on $NiMoO_4$ (5%)/GO(95%)/GCE. The calibration curves were constructed with concentration variation in dynamic range from 0.10 µmol L^{-1} to 800 µmol L^{-1} (Fig. 3.67 B) and linear dynamic range from 0.1 µmol L^{-1} to 100 µmol L^{-1} with an equation i_{pa} =1.8058 c_{ACP} – 2.3372; R^2=0.9966 (Figure 3.67 C). The limit of detection (LOD) was obtained as 11.9 nmol L^{-1} The LOD value was found from the equation LOD=3.3S/m. In this equation, S is the is the standard deviation value of the blank solution, m is the the calibration graph slope.

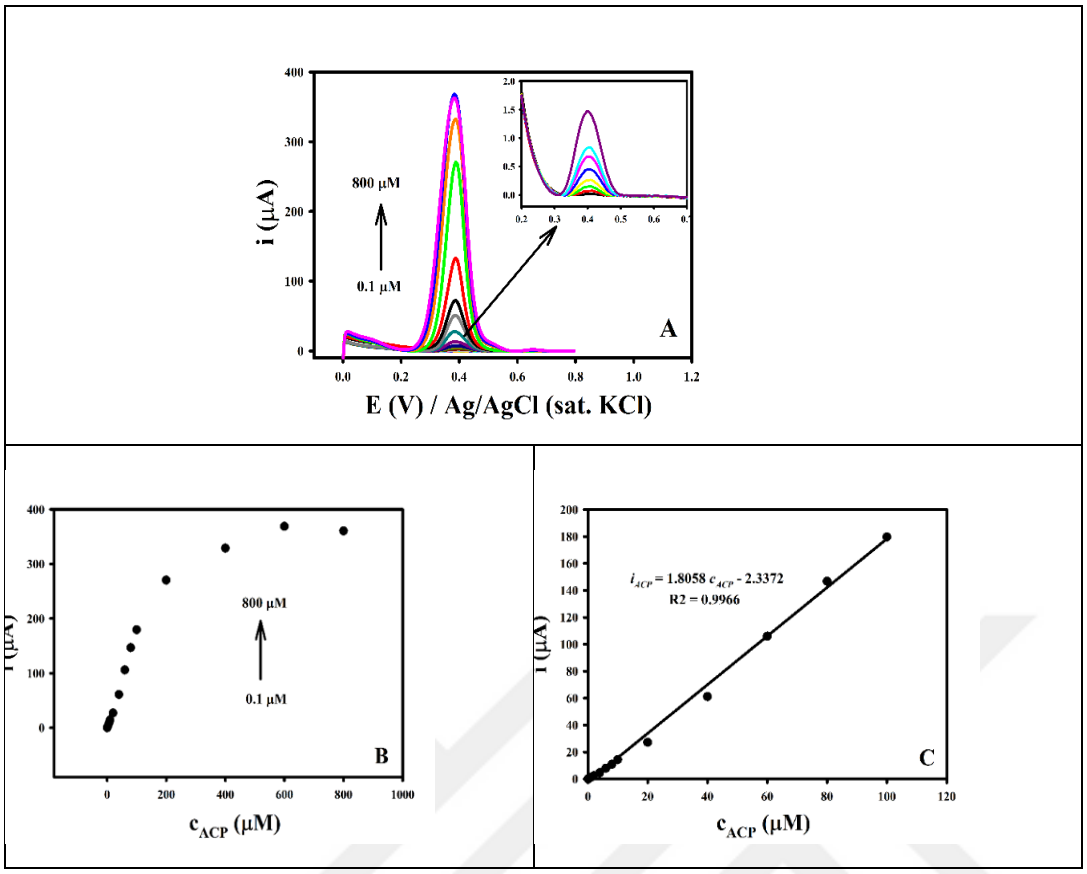

Figure 3.60 A)SWV of different concentrations of ACP (0.1; 0.2; 0.4; 0.6; 0.8; 1.0; 2.0; 4.0; 6.0; 8.0; 10.0; 20.0; 40.0; 60.0; 80.0; 100.0; 200.0; 400.0; 600.0 and 800.0 µM) at ($NiMoO_4$)(%5)+(%95)GO/GCE in the pH 7.00 PBS with 2 Hz frequency and 30 mV amplitude B) Plots for ACP oxidation peak currents versus concentration of dynamic range (0.1 µM – 800.0 µM ACP) and C) linear calibration range (0.2 µM – 100.0 µM) at $NiMoO_4$(5%)/GO(95%)/GCE in the pH 7.00 PBS.

More sensitive results were found at ($NiMoO_4$)(%5)+(%95)GO/GCE, as shown by the results indicating that this modified electrode provides the best catalytic activity towards oxidation of ACP with a maximum slope value.

A comparative SWV behaviour of TRP was investigated depending on increasing TRP concentration in pH 5.00 AcH/Ac, and the peak current dependency on TRP concentrations were shown in Fig 3.68 at bare GCE; Fig 3.69 and Fig 3.70 at GO/GCE and Fig. 3.71 and 3.72
at (%5)($NiMoO_4$)+(%95)GO/GCE.

The oxidation peak current of TRP was appeared at 0.803 V and the peak current was linear by increasing the TRP concentration range from 0.6 µmol L^{-1} to 100 µmol L^{-1} at bare GCE (Figure 3.68). The linear regression equation was i_{pa} = 0.0109 c_{TRP} - 0.055 with correlation coefficients of R^2=0.9973. The LOD was 0.128 µmol L^{-1}.

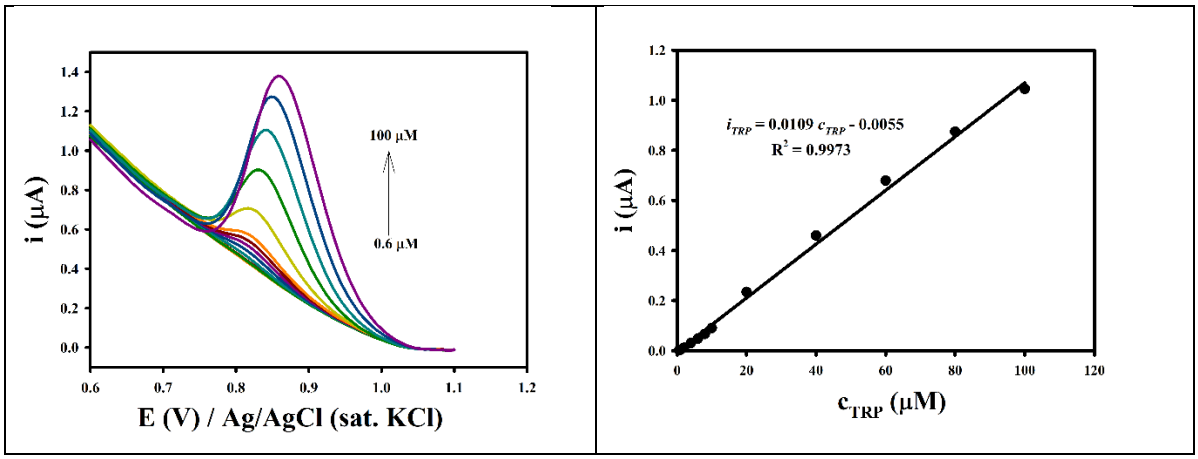

Figure 3.61 SWV of different concentrations of TRP (0.6; 0.8; 1.0; 2.0; 4.0; 6.0; 8.0; 10.0; 20.0; 40.0; 60.0; 80.0 and 100 µM) at bare GCE in the pH 5.00 AcH/Ac. The linear curves of i_{TRP} vs c_{TRP}.

The oxidation of TRP was studied in two different potential ranges, 0.15 V – 1.1 V and 0.4 V – 1.1 V at GO/GCE and $NiMoO_4$(%5)+GO(%95)/GCE. It has been observed that it gives oxidation peaks at 0.45 V and 0.76 V respectively when the experimental was performed in a expanded potential window as 0.15 V – 1.10 V. For this reason, calibration curves were constructed for both current potential windows (Figure 3.69 – 3.72). In the case of the SWVs obtained by expanded potential range current potential window, two different calibration curves were performed by considering the alone each peak height at 0.45 V and 0.76 V (Figure 3.69 B) and the sum of two peak currents at 0.45 V and 0.76 V (Figure 3.69 C). The calibration curves were obtained with linear regression equation as i_{pa} *(I)* = 1.0965 c_{TRP} - 0.3254 (R^2=0.9906) and i_{pa} *(II)* = 0.1313 c_{TRP} - 0.1474 (R^2=0.9934).

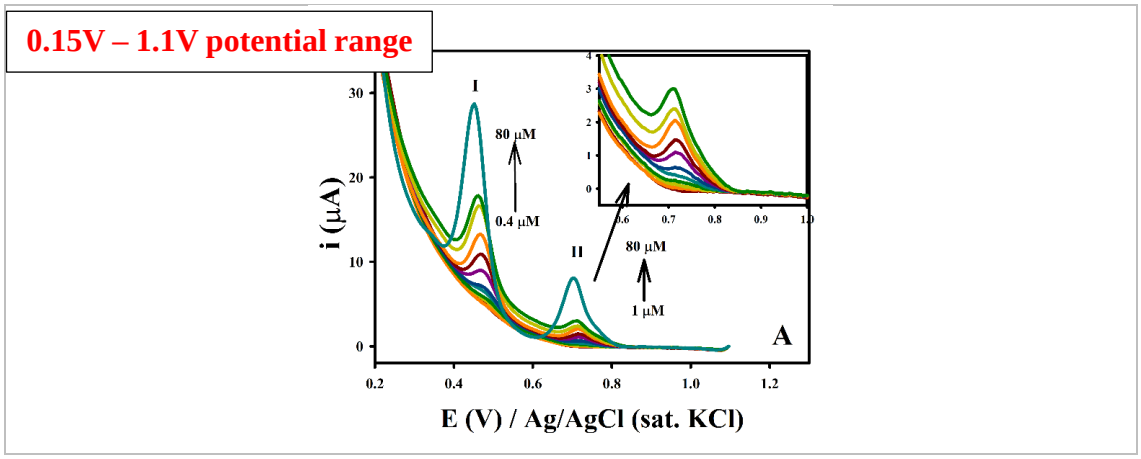

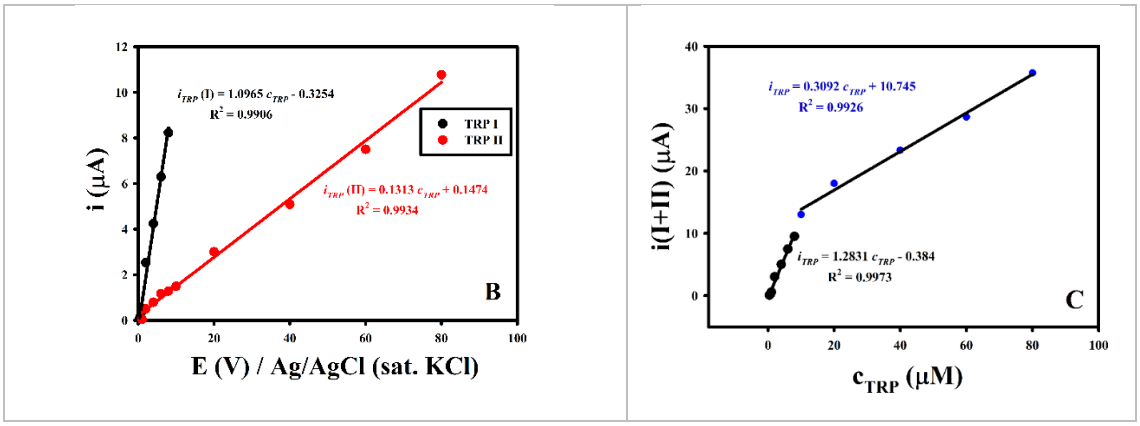

Figure 3.62 SWV of different concentrations of TRP (0.6; 0.8; 1.0; 2.0; 4.0; 6.0; 8.0; 10.0; 20.0; 40.0; 60.0; 80.0 and 100 µM)) at GO/GCE in the pH 5.00 AcH/Ac with 2 Hz ferquency and 30 mV amplitude. The linear curves of oxidation i_{TRP} vs c_{TRP}..

In the case of narrow potential range from 0.40 V to 1.10 V current potential scan by SWV technique, only an oxidation peak was observed at 0.72 V in the presence of varied concentration of TRP in pH 5.0 AcH/Ac buffer solution on GO/GCE (Figure 3.70). The oxidation peak current was linear in the concentration ragne from 0.6 µmol L^{-1} to 100.0 µmol L^{-1} of TRP. The calibration curve was obtained with linear regression equation as i_{pa} =0.0704 c_{TRP} - 0.2688 (R^2=0.9928).

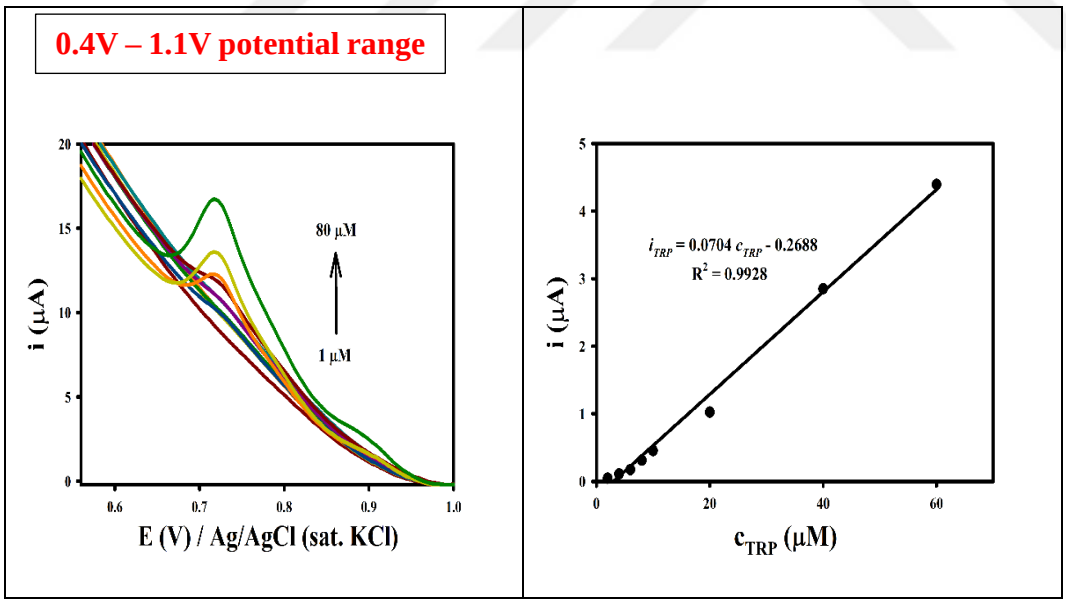

Figure 3.63 SWV of different concentrations of TRP (1.0; 2.0; 4.0; 6.0; 8.0; 10.0; 20.0; 40.0; 60.0 and 80.0 µM)) at GO/GCE in the pH 5.00 AcH/Ac with 2 Hz ferquency and 30 mV amplitude. The linear curves of oxidation i_{TRP} vs c_{TRP}.

The SWV behaviour of TRP was studied by increasing its concentration from 0.4 µmolL^{-1} to 80.0 µmolL-1 in pH 5.00 AcH/Ac buffer solution on $NiMoO_4$(%5)+GO(%95)/GCE by monitoring the voltammograms in both

expanded current potential window and narrov current potential window. The ox **0.15V – 1.1V potential range** 0.487 V and 0.714 V for expanded current potential window as from 0.15 V to 1.10 V and at 0.727 V for narrow current potential window. (Figure 3.71 and 3.72). In the case of the SWVs obtained by expanded current-potential window, two different calibration curves were constructed by taking into account the alone each peak height at 0.487 V and 0.727 V (Figure 3.71 B) and the sum of two peak currents at 0.487 V and 0.727 V (Figure 3.71 C).

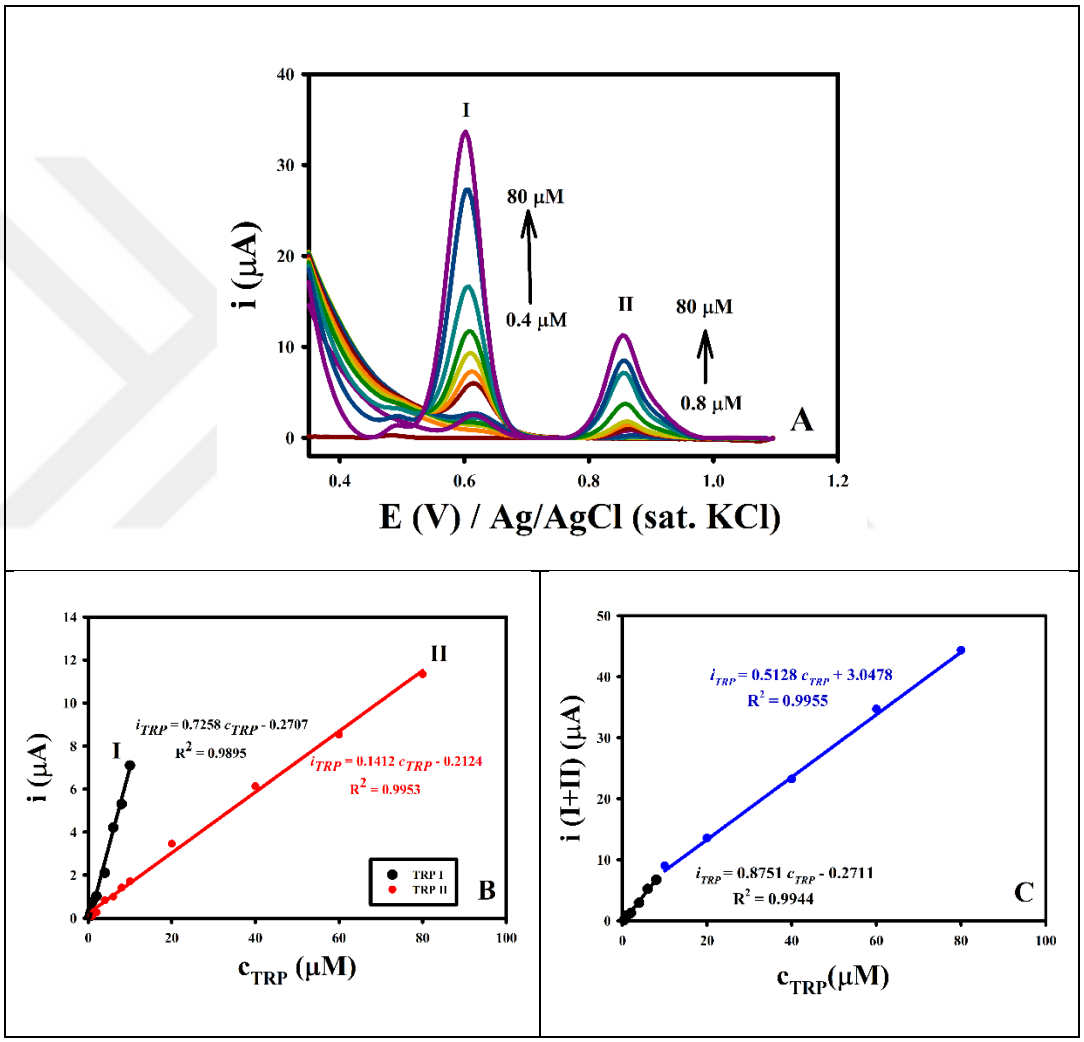

Figure 3.64 SWV of different concentrations of TRP I) (0.4; 0.6; 0.8; 1.0; 2.0; 4.0; 6.0; 8.0; 10.0; 20.0; 40.0; 60.0 and 80.0 µM)) and II) 0.8; 1.0; 2.0; 4.0; 6.0; 8.0; 10.0; 20.0; 40.0; 60.0 and 80.0 µM) at $NiMoO_4$(%5)+GO(%95)/GCE: in the pH 5.00 AcH/Ac with 2 Hz ferquency and 30 mV amplitude. The linear curves of oxidation i_{TRP} vs c_{TRP}.

In the case of narrow potential range from 0.40 V to 1.10, only an oxidation peak was observed at 0.737 in the presence of varied concentration of TRP in pH 5.00 AcH/Ac buffer solution on $NiMoO_4$(%5)+GO(%95)/GCE (Fig. 3.72A). The oxidation peak current of TRP was increased by inceasing of its concentration in

the range from 0.8 µmol L^{-1} to 1.0 mmol L^{-1} on $NiMoO_4$(5%)/GO(95%)/GCE . The calibration curves were constructed with concentration variation in dynamic range from 0.8 µmol L^{-1} to 1000 µmol L^{-1} (Figure 3.72 B) and linear dynamic range from 0.8 µmol L^{-1} to 80 µmol L^{-1} with an equation i_{pa} =0.1435 c_{TRP} – 0.0215; R^2=0.9971 (Figure 3.72 C).

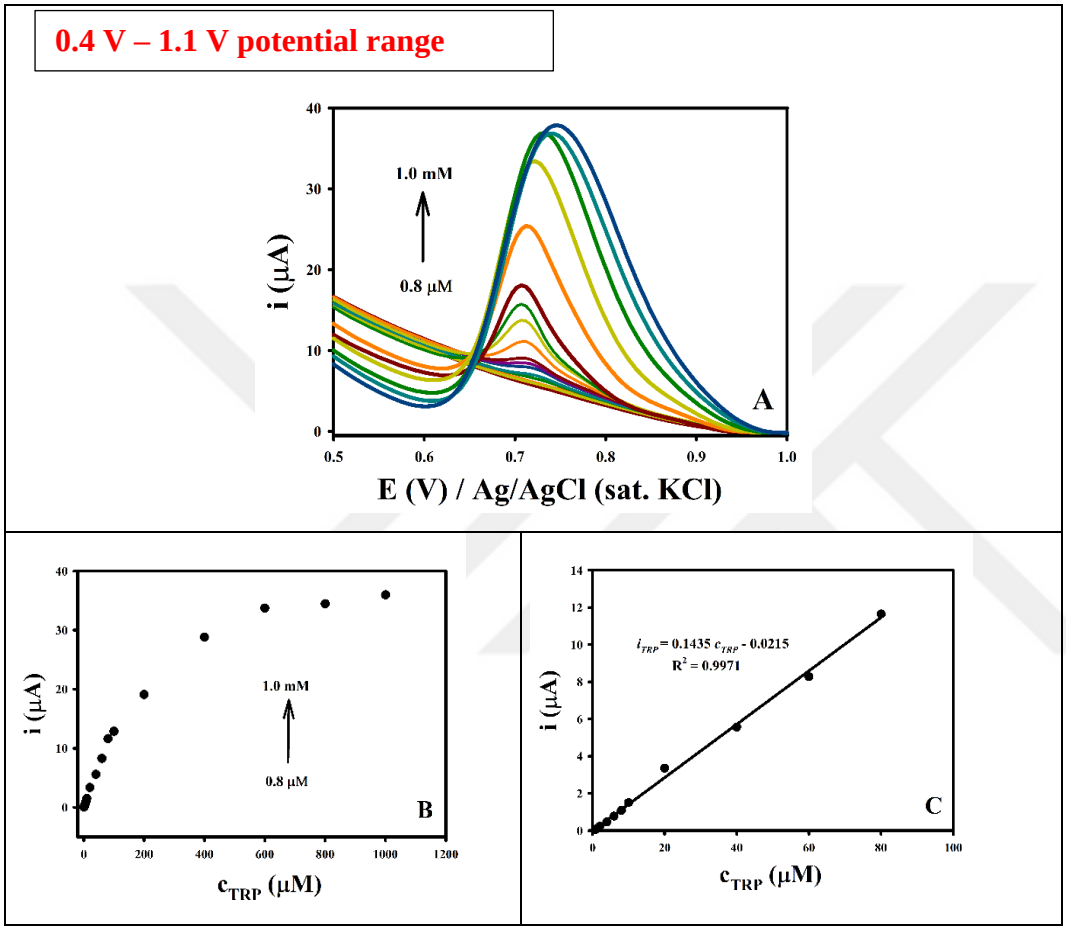

Figure 3.65 A) SWV of different concentrations of TRP (0.8; 1.0; 2.0; 4.0; 6.0; 8.0; 10.0; 20.0; 40.0; 60.0; 80.0; 100.0; 200.0; 400.0; 600.0;800.0 µM and 1.0 mM)) at GO/GCE in the pH 5.00 AcH/Ac with 2 Hz ferquency and 30 mV amplitude. B) Plots for TRP oxidation peak currents versus concentration of dynamic range (0.8 µM – 1.0 mM TRP) and C) linear calibration range (0.8 µM – 80.0 µM) at $NiMoO_4$(5%)/GO(95%)/GCE in the pH 5.00 AcH/Ac

Table 3.22 Limit of detection (LOD) and linear concentration range of bare and modified electrodes for individual determination of ACP and TRP.

ANALYTES	Acetaminophen	Tryptophan
ELECTRODE	BARE GCE	
LINEAR RANGE	$1.0x10^{-6}$ mol L^{-1}- $4.0x10^{-4}$ mol L^{-1}	$6.0x10^{-7}$ mol L^{-1}-$4.0x10^{-4}$ mol L^{-1}
LOD	$9.57x10^{-7}$ mol L^{-1}	4 .28 x 10^{-7} mol L^{-1}
ELECTRODE	GO/GCE	
LINEAR RANGE	$2.0x10^{-7}$ mol L^{-1}- $2.0x10^{-4}$ mol L^{-1}	4.0 x 10^{-7} mol L^{-1}– $8.0x10^{-}$ mol L^{-1}

LOD	1.81 x 10^{-7} mol L^{-1}	3.51 x 10^{-7} mol L^{-1}
ELECTRODE	**$NiMoO_4$(5%)+GO(95%)/GCE**	
LINEAR RANGE	1.0x10^{-7} mol L^{-1}- 1.0 x 10^{-4} mol L^{-1}	4.0x10^{-7} mol L^{-1} – 8.0x10^{-5} mol L^{-1}
LOD	1.19 x 10^{-8} mol L^{-1}	1.69x10^{-7} mol L^{-1}

3.7 Simultaneous Voltammetric Determination of Acetaminophen and Tryptophan by Square Wave Voltammetry

In the simultaneous determination of ACP and TRP, SWV often exhibits greater sensitivity in detecting the analyte response as compared to CV. Simultaneous determination of ACP and TRP was also investigated bare GCE, GO/GCE and $NiMoO_4$(%5)+GO(%95)/GCE. Determination of one component presence of another was carry out by addition of increasing concentrations of the analyte while keeping the other analyte's concentration constant.

Figure 3.73 exhibits the SW voltammograms obtained for increasing concentrations of TRP, while the concentration of ACP was kept constant at a value of 20 µM on bare GCE in pH 5.0 AcH/Ac. The dependence of peak current on the concentration of TRP was a linear relationship in the range of 0.6 µmol L^{-1} – 80.0 µmol L^{-1} for bare GCE. The linear regression equation of TRP i_{trp} = 0.0118 c_{TRP} + 0.0057 was obtained with correlation coefficent of R^2=0.996.

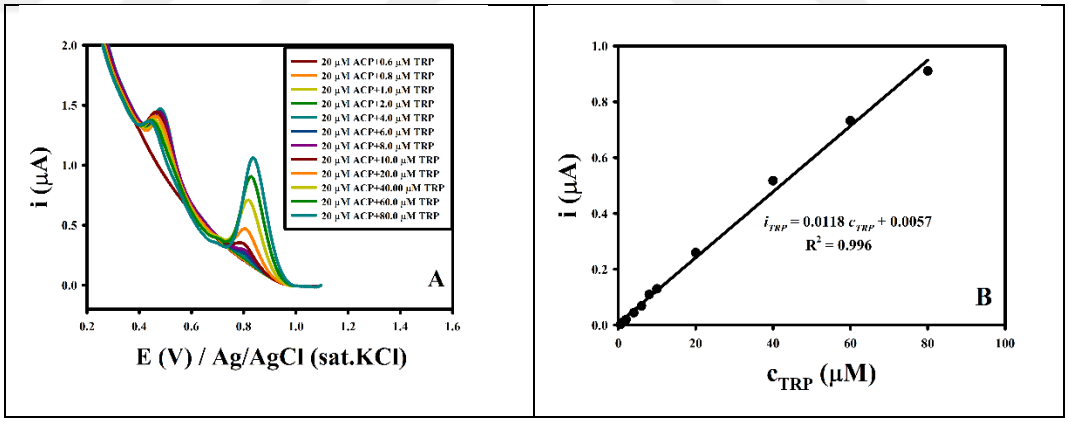

Figure 3.66 A) SW voltammograms of bare GCE in the presence of ACP (20 µM) for increasing concanterations of TRP (0.6; 0.8; 1.0; 2.0; 4.0; 6.0; 8.0; 10.0; 20.0; 40.0; 60.0 and 80.0 µM)) in pH 5.00 AcH/Ac and B) calibration curve of increasing TRP concenrations.

Fig. 3.74 shows the SW voltammograms obtained for increasing concentrations of ACP, while the concentration of TRP was kept constant at a value of 50 µM on bare GCE in pH 5.00 AcH/Ac buffer solution. The linear range of ACP was found as 1.0 - 400.0 µM by the same way that mentioned above previously. The peak current of TRP was decreased only slightly with the increasing ACP concentrations. The

linear regression equation can be expressed as I_p = 00.0128 c_{ACP} - 0.1066 (R^2=0.9977) that shown as Fig. 3.74 B the related voltammogram.

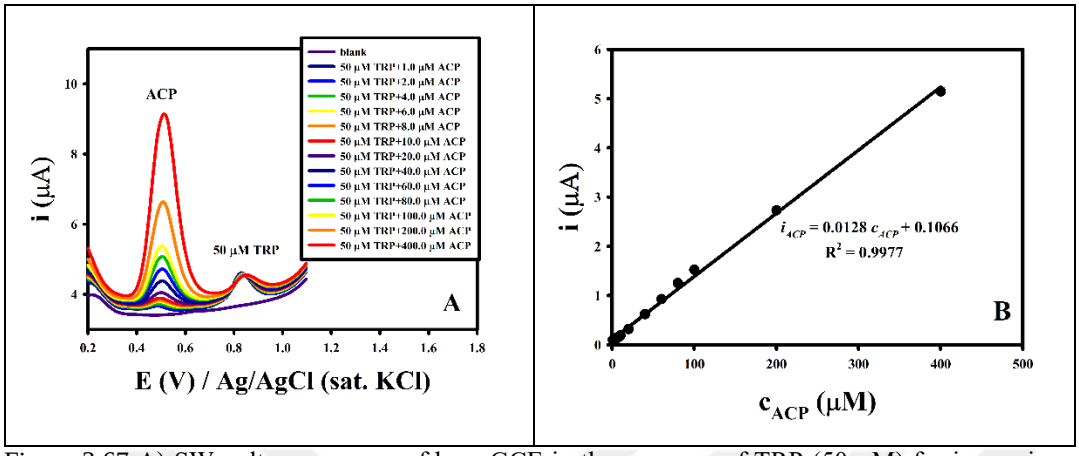

Figure 3.67 A) SW voltammograms of bare GCE in the presence of TRP (50 µM) for increasing concanterations of TRP (1.0; 2.0; 4.0; 6.0; 8.0; 10.0; 20.0; 40.0; 60.0; 80.0; 100.0; 200.0 and 400.0 µM)) in pH 5.00 AcH/Ac B) calibration curve of increasing ACP concenrations.

Similarly, as shown Fig. 3.75 the concantration of ACP constant (10.0 µmol L^{-1}), and the concentration of TRP increased on GO/GCE. The results show that, ipa is proportional to the concentrations of TRP in the range from 1.0 µmol L^{-1} – 80.0 µmol L^{-1}. The regression equation was ip = 0.1014 c_{TRP} + 0.0257, with linear correlation coefficent of R^2=0.9974.

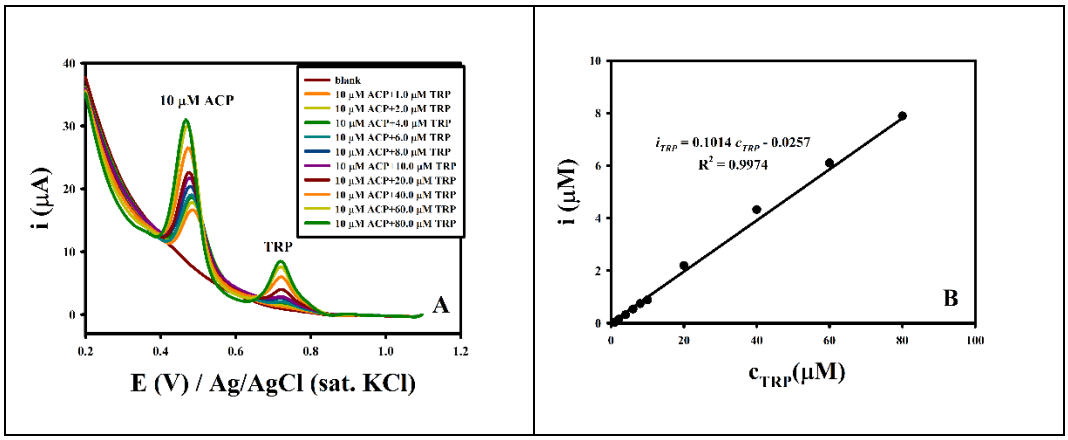

Figure 3.68 A) SW voltammograms of GO/GCE in the presence of ACP (6.0 µM) for increasing concanterations of TRP (1.0; 2.0; 4.0; 6.0; 8.0; 10.0; 20.0; 40.0; 60.0 and 80.0 µM)) in pH 5.00 AcH/Ac and B) calibration curve of increasing TRP concenrations.

Fig. 3.76 A demostrates SW voltammograms recorded for TRP concentration varying, while the ACP concentration was kept constant as 10.0 µmol L^{-1} at $NiMoO_4$(%5)+GO(%95)/GCE in pH 5.00 AcH/Ac buffer solution. However, the peak current of ACP has not maintain a constant value by variying of TRP

concentration, the peak current was linearly increased by increasing of TRP concentration in the range from 0.6 µmolL^{-1} to 100 µmol L^{-1} The linear regression equation of TRP *ip(trp)* = 0.1711 c_{trp} + 0.2397 was obtained with correlation coefficent of R^2=0.9965 (Fig. 3.76 B).

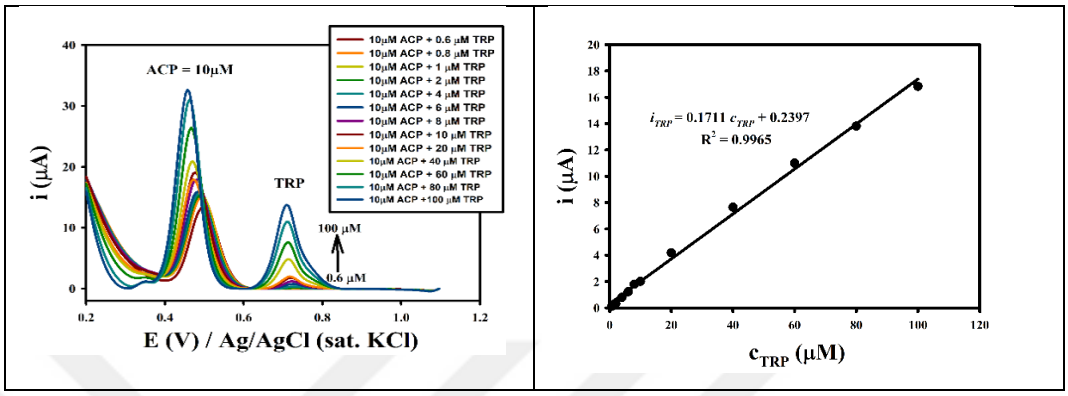

Figure 3.69 SW voltammograms of $NiMoO_4$(%5)+GO(%95)/GCE in the presence of ACP (10 µM) for increasing concanterations of TRP (0.4; 0.6; 0.8; 1.0; 2.0; 4.0; 6.0; 8.0; 10.0; 20.0; 40.0; 60.0; 80.0 and 100.0 µM)) in pH 5.00 AcH/Ac and corresponding calibration curve of increasing TRP concenrations.

While the concentration of TRP was maintained constant as 6.0 µmol L^{-1} TRP, the ACP concentration was gradually increased (Fig. 3.77). The results show that, ip_{acp} was proportional to the concentrations of ACP in the range from 1.0 µmol L^{-1} to 400.0 µmol L^{-1}. The regression equation was i_{acp} = 0.9724 c_{acp} + 2.9029 with a linear correlation coefficient (R^2) as 0.9961.

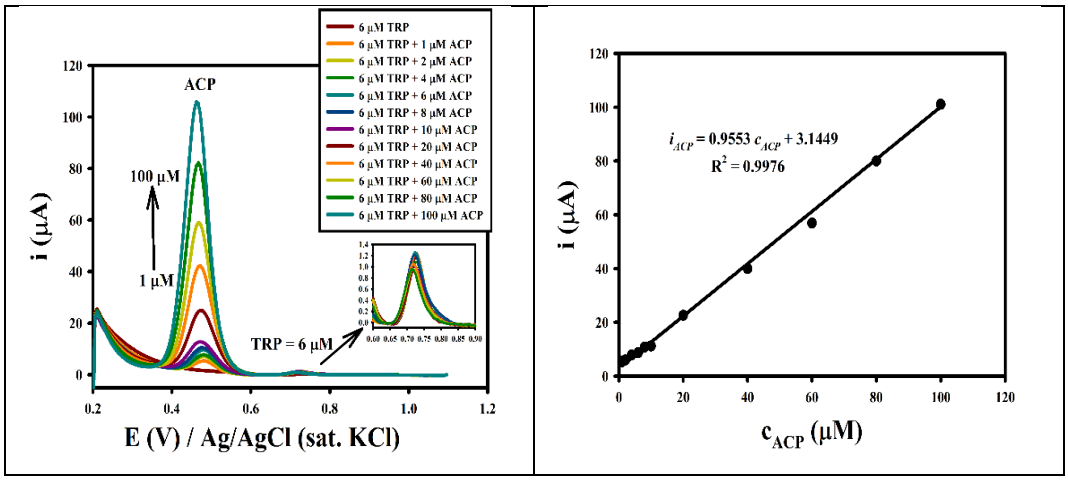

Figure 3.70 SW voltammograms of $NiMoO_4$(%5)+GO(%95)/GCE in the presence of TRP (6 µM) for increasing concanterations of ACP in pH 5.00 AcH/Ac and corresponding calibration curve of increasing ACP concenrations (1µM-100 µM).

On the other hand, the SWVs were performed by simultaneously increasing the concentration of ACP and TRP in pH 5.00 AcH/Ac buffer solution on bare GCE (Fig. 3.78). Two well defined oxidation peaks were appeared at 0.467 V and 0.764

V for ACP and TRP. The oxidation peak currents of both ACP and TRP were linearly increased by ACP and TRP concentrations in the range from 0.6 µmol L^{-1} to 80 µmol L^{-1} and from 0.8 µmol L^{-1} to 80 µmol L^{-1} respectively. The regression equations were i_{acp} = 0.089 c_{acp} + 0.0174 and i_{trp}= 0.0103 c_{trp} + 0.0054 with a linear correlation coefficients (R^2) as 0.9965 and 0.9939, respectively. The LOD were 0.33 µmol L^{-1} for ACP and 0.2 µmol L^{-1} for TRP. The results shown that the simultaneously determination of ACP and TRP can be carried out on bare GCE.

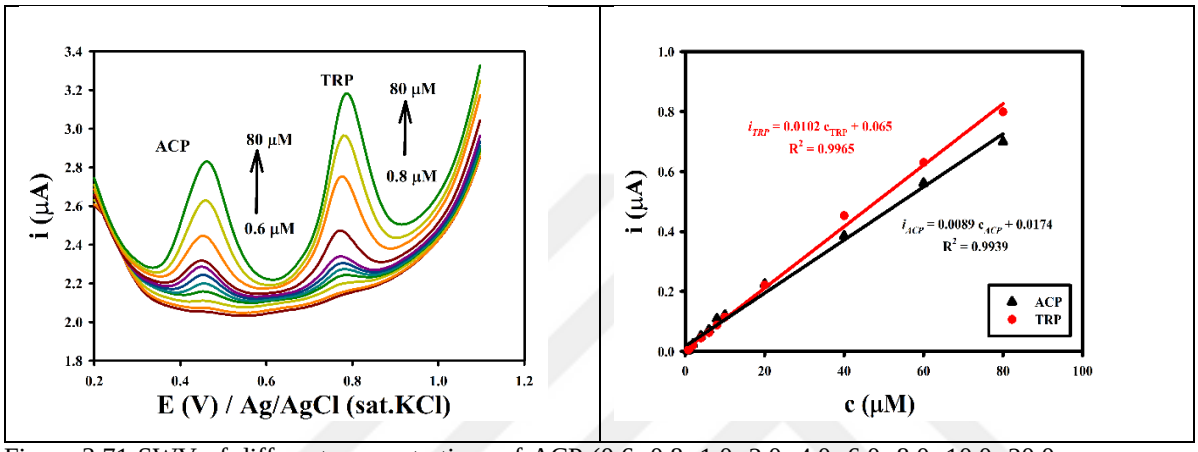

Figure 3.71 SWV of different concentrations of ACP (0.6; 0.8; 1.0; 2.0; 4.0; 6.0; 8.0; 10.0; 20.0; 40.0; 60.0 and 80.0 µM) and TRP (0.8; 1.0; 2.0; 4.0; 6.0; 8.0; 10.0; 20.0; 40.0; 60.0 and 80.0 µM) at bare GCE in the pH 5.00 AcH/Ac. The linear curves of oxidation peak current versus different concentrations of ACP and TRP.

Fig. 3.79 A shows that SWV response of GO/GC electrodes in pH 5.00 in the absence and presence of increasing concentrations of ACP and TRP. The linear concentration range of ACP and TRP was incraesed from 0.4 µmol L^{-1} to 10.0 µmol L^{-1} and 1.0 µmol L^{-1} – 80 µmol L^{-1}, respectively. The calibration curve for ACP was shown two linear segments: the first linear segment increases from 0.4 µmol L^{-1} to 1.0 µmol L^{-1} with linear regression equation I_p=4.4341 c_{ACP} – 1.6494 (R^2=0.9939) and second linear segment increases from 2.0 µmol L^{-1} to 10.0 µmol L^{-1} with linear regression equation of I_p=1.4925 c_{ACP} – 2.5458 (R^2=0.9938), respectively (Fig. 3.79 B). Additionally, Fig. 3.79 C have shown that the oxidation peaks current were linearly related to TRP concentrations in the concentration range from 1.0 µmol L^{-1} to 80.0 µmol L^{-1} at GO/GCE. The equation of linearity is I_p=0.1041 C_{TRP} + 0.0891 (R^2=0.9934). The LOD values of ACP and TRP on GO/GCE were calculated as 8.84x10^{-8} mol L^{-1} and 1.52x10^{-7} mol L^{-1} respectively.

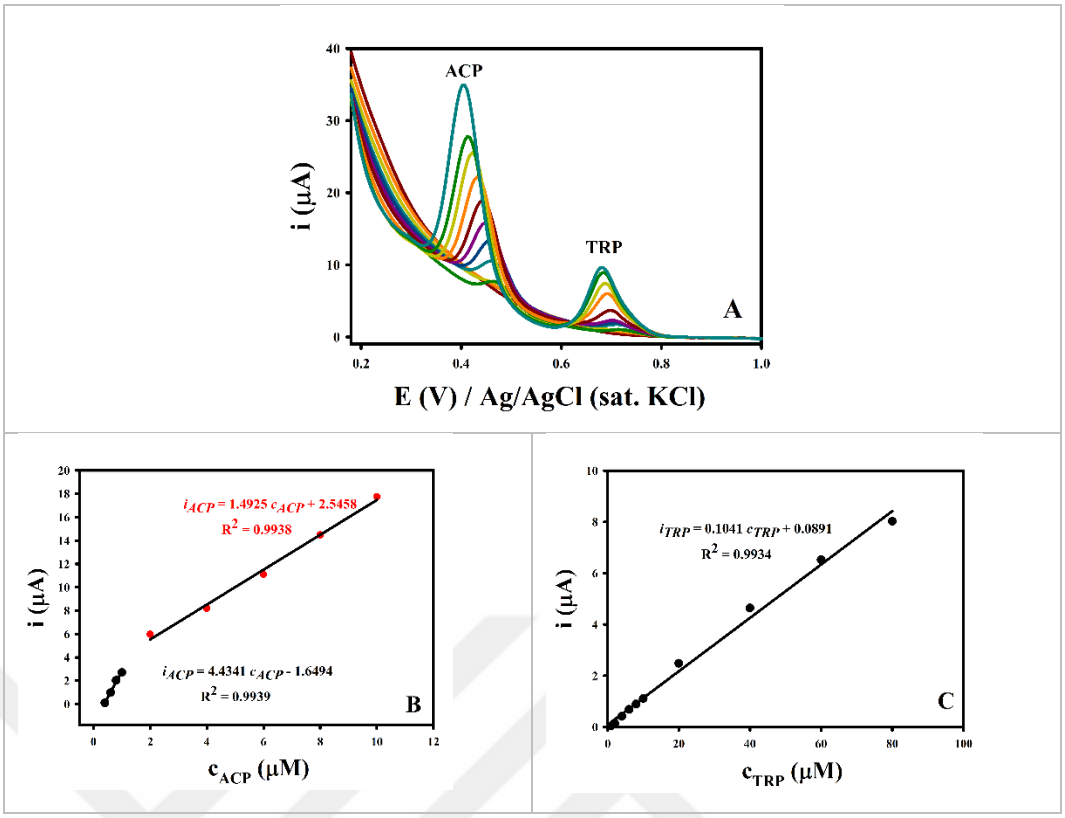

Figure 3.72 A) SWV of different concentrations of ACP (0.4; 0.6; 0.8; 1.0; 2.0; 4.0; 6.0; 8.0; 10.0 μM) and TRP (1.0; 2.0; 4.0; 6.0; 8.0; 10.0; 20.0; 40.0; 60.0 and 80.0 μM) at GO/GCE in the pH 5.00 AcH/Ac. B) The linear curves of oxidation peak current versus different concentrations of ACP and C) TRP.

SWV response of simultaneous gradually increasing concentration of ACP and TRP in 0.1 mol L^{-1} AcH/Ac buffer solution on ($NiMoO_4$)(5%)+(95%)GO/GCE were shown in Fig. 3. 80A. The peaks current were increased by increasing the ACP and TRP concentartions in the range from 0.1 μmol L^{-1} to 10.0 μmol L^{-1} and from 0.6 μmol L^{-1} to 60.0 μmol L^{-1} respectively. The calibration curve for ACP demostrate two linear segments: the first linear segment increases from 0.1 μmol L^{-1} to 1.0 μmol L^{-1} with linear regression equation I_p=4.7114 c_{ACP} – 0.5456 (R^2=0.9918) and second linear segment increases from 2.0 μmol L^{-1} to 10.0 μmol L^{-1} with linear regression equation of I_p=2.8087 c_{ACP} + 2.7284 (R^2=0.9933), respectively (Fig. 3.80 B). Additionally, Fig. 3.80 C have shown that the oxidation peaks current were linearly related to TRP concentrations in the concentration range from 0.6 μmol L^{-1} to 60.0 μmol L^{-1} at ($NiMoO_4$)(%5)+(%95)GO/GCE. The equation of linearity is I_p=0.1339 c_{ACP} + 0.069 (R^2=0.9934). The LOD values of ACP and TRP on ($NiMoO_4$)(%5)+(%95)GO/GCE were calculated as 10.0 nmol L^{-1} and 0.798 nmol L^{-1} respectively.

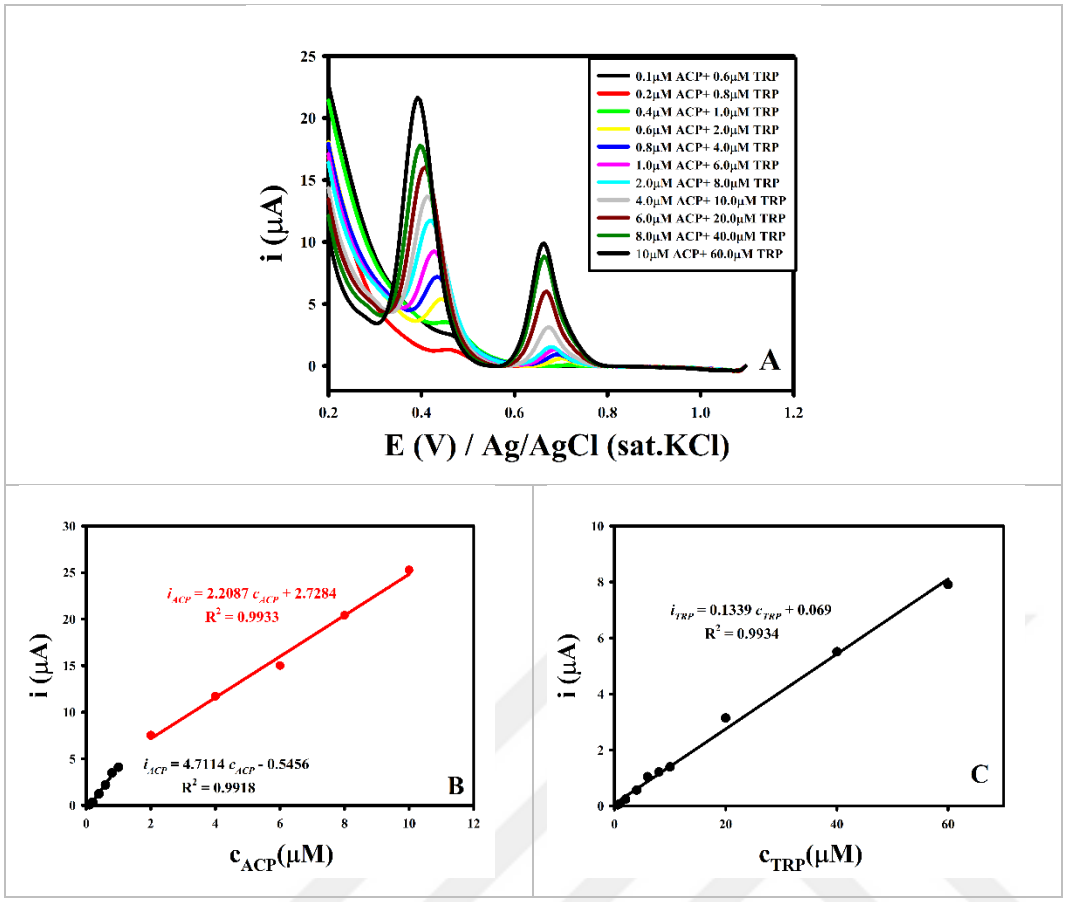

Figure 3.73 A) SWV of different concentrations of ACP (0.1; 0.2; 0.4; 0.6; 0.8; 1.0; 2.0; 4.0; 6.0; 8.0 and 10.0 µM) and TRP (0.6; 0.8; 1.0; 2.0; 4.0; 6.0; 8.0; 10.0; 20.0; 40.0 and 60.0 µM) at ($NiMoO_4$)(5%)+(95%)GO/GCE in the pH 5.00 AcH/Ac. The linear curves of oxidation peak current versus different concentrations of ACP (B) and TRP (C).

Table 3.23 shows a comparison of the LOD, and linear concentration range of ACP and TRP at bare GCE and modified electrodes.When comparing bare and modified electrodes, it is clear that the ($NiMoO_4$)(%5)+(%95)GO/GCE exhibits more activity toward ACP and TRP oxidation, with an increase in the detection limit.

Table 3.23 Limit of detection (LOD) and linear concentration range of bare and modified electrodes for simultaneous determination of ACP and TRP.

ANALYTES	**Acetaminophen**	**Tryptophan**
ELECTRODE	**BARE GCE**	
LINEAR RANGE	$6.0x10^{-7}$ – $8.0x10^{-5}$ M	$8.0x10^{-7}$ – $8.0x10^{-5}$ M
LOD	3.33 x 10^{-7} M	2.0 x 10^{-7} M
ELECTRODE	**GO/GCE**	

LINEAR RANGE	4.0×10^{-7} – 4.0×10^{-6} M 4.0×10^{-6} – 1.0×10^{-5} M	1.0×10^{-6} – 8.0×10^{-5} M
LOD	8.84×10^{-8} M	1.52×10^{-7} M
ELECTRODE	**$NiMoO_4$(5%)+GO(95%)/GCE**	
LINEAR RANGE	1.0×10^{-7} – 1.0×10^{-5} M	6.0×10^{-7} – 6.0×10^{-5} M
LOD	10.0×10^{-9} M	7.98×10^{-8} M
ANALYTE	**ACP (10^{-5} M) + TRP ↑**	**TRP (6×10^{-6} M) + ACP ↑**
ELECTRODE	**$NiMoO_4$(5%)+GO(95%)/GCE**	
LINEAR RANGE	1.0×10^{-6} – 100.0×10^{-6} M	6.0×10^{-7} – 1.0×10^{-4} M
LOD	3.33×10^{-8} M	2.0×10^{-7} M

*LOD values calculated from calibration curve

Table 3.24 Comparison of the developed electrodes results with other modifie electrode previous reports for the detection of ACP and TRP.

Electrodes	**LR (µmol L^{-1})**	**LOD (mol L^{-1})**	**Reference**
poly-Trypan Blue modified glassy carbon electrode	0.2 – 530.0 (ACP) 1.0-345.0 (TRP)	1.0×10^{-7} (ACP) 8.0×10^{-7} (TRP)	Taei et. al., 2017
SnSe/TiO_2@GO	0.0089−410 (ACP) 0.0136−190 (TRP)	3.0×10^{-9} 5.3×10^{-9}	Murugan E. and Kumar K. 2022
Lewatit® FO36 resin (LFOR modified GPE	7.0- 300.0 10.0-300.0	8.42×10^{-7} 3.085×10^{-7}	Rajabi et. al., 2016
trimetallic nanoparticles of (Au/Ag/Pd)NPs uniformly capped electropretreated graphene oxide (EPGrO)	5.0-700.0 1.0-600.0	3.0×10^{-8} 1.2×10^{-8}	Abdelwahab et.al., 2020
$NiMoO_4$(5%)+GO(95%)/GCE	**0.06 – 10.0** **20.0 – 80.0**	**10.0×10^{-9}** **7.98×10^{-8}**	**Present study**

3.3.5 Reproducibility, Repeatability of ($NiMoO_4$)(5%)+(95%)GO/GCE

The SWV method was used to investigate repeatability, reproducibility, and stability. To evaluate the repeatability of the modified electrode, the responses to the ACP and TRP were investigated for five different modified electrodes prepared in the same way. As an obvious result of this, the relative standard deviation (RSD) of the peak currents for ACP and TRP, respectively (n=5), were 1.64% and 1.54%, respectively. This demonstrates that the electrode showed good reproducibility (Fig. 3.74 A).

Relative standard deviation (RSD) of peak current was 0.26% for ACP and 0.36% for TRP when using the same electrode during a day to analyze electrode repeatability (n=5). (Fig. 3.74 B).

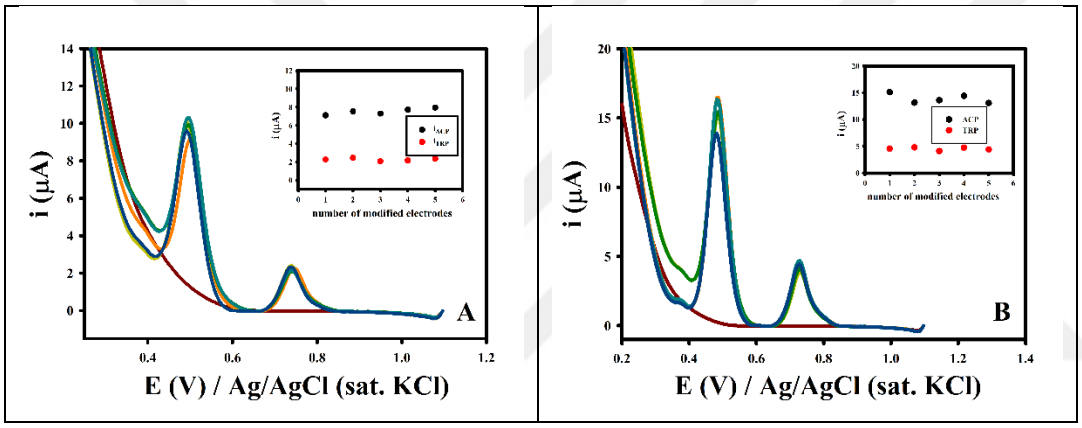

Figure 3.74 SWV studies on A) inter-day (n=5) and B) intra-day (n=5) with ($NiMoO_4$)(5%)+(95%)GO/GCE for 0.6 μM ACP and 10.0 μM TRP.

3.3.6 Interference Studies

Selectivity of (5%)($NiMoO_4$)+(95%)GO/GC electrode was determined by studying Selectivity of (5%)($NiMoO_4$)+(95%)GO/GC electrode was controled by monitoring 2.0 $\mu molL^{-1}$ ACP and 20.0 $\mu molL^{-1}$ TRP oxidation in the presence of possible interferents of inorganic salts and organic compounds. The effects of various of species on analytical responses of ACP and TRP were studied. For this aim, the other species were added into 0.1M AcH/Ac (pH 5.0) containing 2.0 $\mu molL^{-1}$ ACP, and 20 $\mu molL^{-1}$ TRP. The obtained results were evaluated and were given in Table 3.26. The SWV responses of 2.0 $\mu molL^{-1}$ ACP, and 20 $\mu molL^{-1}$ TRP were not affected by concentrations of common ions such as 100 fold of Na^+, K^+, Ni^{2+}, Fe^{2+}, Cl^-, NO^{3-}, $SO_4{}^{2-}$. Other commonly present organic were also studied for their potential to cause interference. However, equal molars of ascorbic acid and

dopamine cause serious interference, uric acid have interfere after addition of 100 fold of their concenteration. The interference of various amino acids such as L-methionine and cysteine has also been studied. While L-methionine was interfered to ACP and TRP responses in the presence of 100-fold concentration. Morever, cysteine can be interefered in the presence of 100-fold concentration to ACP response and in the presence of same concentration with TRP.

Table 3.25 Relative (%) change of the analytical signal of ACP ($2.0x10^{-6}$ mol.L^{-1}) and TRP ($2.0x10^{-5}$ mol.L^{-1}) in the pH 5.0 AcH/Ac on (5%)($NiMoO_4$)+(95%)GO/GCE.

Interfering species	**Molar ratio ([Interferingspecies]/[ACP])**	**Change on the analytical signal**	
		ACP (%)	**TRP (%)**
Ascorbic acid	1	-10.44	+5.83
	10	-15.49	-1.03
	100	+0.61	-6.36
	1000	-0.47	-66.43
Dopamine	10	+5.43	-6.00
	100	-25.64	-33.06
	1000	-83.91	-
Glucose	10	-3.97	-4.79
	100	-1.20	-5.74
	1000	-13.08	-25.06
Uric Acid	1	+23.19	-3.29
	10	-3.33	-12.89
	100	-10.60	-11.18
	1000	-	-44.56
L-Cysteine	10	-0.59	+15.48
	100	-25.05	-86.60
	1000	-93.9	-
L-Methionine	1	+28.4	-21.09
	10	+4.86	-23.86
	100	+3.49	-27.50
	1000	-9.96	-51.89
Na^+	10	-2.00	+1.47
	100	-5.84	-4.49
	1000	-6.75	-28.84
K^+	10	+6.65	+0.29
	100	-7.56	-0.81
	1000	-8.65	-21.87
Fe^{2+}	10	+5.65	+2.69
	100	-2.96	+4.33
	1000	-7.41	-6.69
Ni^{2+}	10	+5.65	+2.69
	100	-2.96	+4.33
	1000	-7.41	-6.69
Cl^-	10	-2.00	+1.47
	100	-5.84	-4.49
	1000	-6.75	-28.84
NO_3^-	10	+6.65	+0.29
	100	-7.56	-0.81
	1000	-8.65	-21.87
SO_4^{2-}	10	+5.65	+2.69
	100	-2.96	+4.33

	1000	-7.41	-6.69

3.3.6 Sample Analysis

The standard addition method was used to evaluate the performance of (5%)($NiMoO_4$)+(95%)GO/GCE. The results were given in Table 3. The recovery values were obtained between 93.59 – 104.0 % for the ACP and 89.26-105.83 % for TRP. The obtained data showing that the sensor could be successfully applied for the simultaneous determination of the analytes in these type of samples (Fig.3.75).

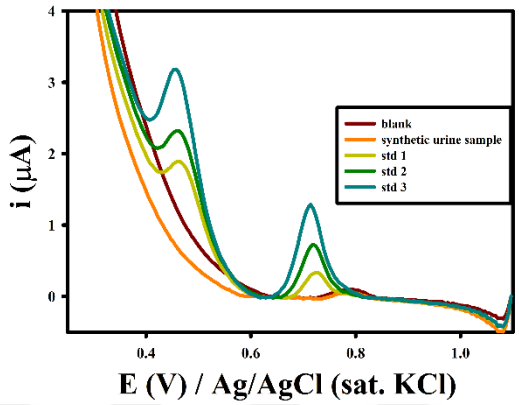

Figure 3.75 SWs for standart addition method of ACP and TRP determination in synthetic urine.

Table 3.26 Determination of ACP and TRP in synthetic urine by SWV.

Analyte	Added (µM)	Faund (µM)	Recovery (%)	RSD (n=3)
ACP	0.1	0.103	103	3.8
	0.2	0.208	104	4.1
	0.4	0.374	93.59	5.2
TRP	4.00	3.571	89.26	5.3
	6.00	6.350	105.83	2.5
	8.00	7.951	99.39	3.3

4. CONCLUSIONS

The development of novel composites electrodes remains very active in the last two decade. The simplify of fabrication, low-cost materials, improved electroanalytical and electrocatalytic properties of composite materials represent the subject. The fabrication of new composite electrodes have distinguished capabilities in the monitoring of biological and pharmaceutical importants compounds with in the low detection limits and linear response range that are required for real sample analysis. In particular, the complex composition of biological samples, including some important interfering organic and inorganic species, determines the success of the composite electrode application.

Electrochemical techniques with chemically modified and nanocomposite electrodes offer a powerful platform for sensitive, precise and selective analysis in real samples. Their ability to enhance electrocatalytic properties, minimize interference, and provide tailored surfaces for specific analytes makes them indispensable tools in modern analytical chemistry. However, electroanalytical methods with chemically modified and nanocomposite electrodes provide a valuable alternative that simplifies the analytical process and can yield accurate and reliable results with less sample preparation effort. Therefore, the electroanalytical approach is a great alternative to other analytical techniques.

In this thesis, three different composite electrodes were developed from MWCNT, conducting polymers, graphene oxide and varous metal/metal oxides for sensitive and selectice detection of rutin, ACP and TRP in some pharmaceuticals and in syhentetic urine samples.

Rutin, or water-soluble vitamin P, is a flavonoid glycoside molecule. In the clinic, rutin is used for its ability to reduce blood pressure andreduced capillary permeability. It was also effective in treating hypertension and other blood-related disorders. In the food industry, it can be used in a number of different ways as a stabilizer, colorant, preservative, and UV absorber. Therefore there is a major importance for the determination of rutin level in food, clinical and pharmaceutical samples. Up to the present, many detection methods have been developed by different techniques such as chromatography, spectroscopic techniques. Conversely, the progress of detection methods with lower cost, timesaving response

time, high sensitivity and operational simplicity are required, and the electrochemical analysis techiques have fascinated research interests in this respect.

In addition, electrochemical systems demostrate fast electron transfer and higher selectivity and sensitivity due to containig of mediators and catalysts in the compositions and enhance the sensing properties with composite or nanostructured electrodes. In this thesis, a unique Co_3O_4 modified multi-walled carbon nanotube/polyphenosafranine composite electrode (Co_3O_4/MWCNT/PPSF/GCE) was developed by electrochemical techniques for the sensitive and selective detection of rutin. Highly conductive MWCNT and PPSF with large surface area and numereous Co_3O_4 active sites have been developed. The combination of MWCNT/PPSF and Co_3O_4 have been effectively proved the electrocatalytic properties of the composite electrode towards on rutin quasireversible electrochemical behaviour compare with bare GCE, MWCNT/GCE and MWCNT/PPSF/GCE. The lowest detection limit and wider calibration range for rutin were acquired with Co_3O_4/MWCNT/PPSF/GCE.

The composite surface also demostrates high stability, repeatability, and reproducibility for rutin SWV response. The high stability was proved for 10 days by maintaining the peak height of 96.2% the orginal peak. The inter-day and intra-day RSD values for 0.1 μmol L^{-1} rutin were 1.62 % and 2.63 % respectively. These RSD values indicate that the Co_3O_4/MWCNT/PPSF modified GCE have high reproducibility. The satisfactory repeatability was obtained by fifty consecutive measurements of oxidation peak of 0.10 μmolL^{-1} rutin in pH 3.0 BR buffer solution with a the 2.88 % RSD. The interfering study of some species showed no significant interference with the detection of rutin. The application of the developed composite electrode to detection of rutin some real samples achived satisfactory results, without the necessity of sample pretreatments or time-consuming extractions. The obtained analytical data with Co_3O_4/MWCNT/PPSF/GCE for rutin such as quick detection, high reproducibility, stability, wide linear dynamic range, and low detection limit offer that the developed composite electrode is an attractive postulant for real sample applications.

The second part of this thesis include the chemical synthesis of graphene oxide (GO) and MnO_2:h-MoO_3 hybrid materials to prepare composite electrodes for sensitive and selective detection of ACP. Based on this purpose, newly synthesized

hybrid materials incorporated with GO was composed with to form a unique surface with high surface area.

The second part of this thesis, a hybrid metal oxides of MnO_2/h-MoO_3 and GO were synthesized by chemical precipitation and Brodie methods respectively to sensitive and selective detection of ACP with electroanalytical techniques. The characterization studies by SEM and XRD were identified the well defined hegzagonaol crystal structure of h-MoO_3 while a poor crsytaline structure of MnO_2 was formed in the a hybrid composition.

The preparation of composite material from hybride oxides (MnO_2:h-MoO_3) and GO (**(5%)(3:1)(MnO_2:h-MoO_3)+(95%)GO/GCE)** have higher electron transfer rate, active surface area and electrochemical activity towards ACP compare with bare GCE, **5%)(MnO_2)+(95%)GO/GCE, (5%)(h-MoO_3)+(95%)GO/GCE**. Especially the oxidation peak current of ACP was significantly enhanced on (3:1)(MnO_2:h-MoO_3)(5%)+GO(95%)/GCE. A linear variation of peak current with ACP concentration was obtained while the calibration curve was constituted with two different linear parts at (3:1)(MnO_2:MoO_3)(5%)+GO(95%)/GCE: the first linear part was obtained between 0.06 μmol L^{-1} to 10.0 μmol L^{-1} with linear regression equation of $i_{pa}(\mu A)$= 1.9868 C_{ACP} $(\mu molL^{-1})$ - 0.3217 (R^2=0.9981) and second linear part was establihed between 20.0 μmol L^{-1} – 80.0 μmol L^{-1} with a linear regression equation of $i_{pa}(\mu A)$= 1.2912 C_{ACP} $(\mu molL^{-1})$ + 11.923 (R^2=0.9947). Morever a stable oxidation peak current of ACP was monitored in the presence at least 100 fold concentration of possible interferences of inorganic and organic species. The developed a new (3:1)(MnO_2:h-MoO_3)(5%)+GO(95%) composite electrode and voltammetric method can be used to sensitive and selective detection of ACP in syrup samples. Futuremore, the new composite electrode has some prominent advantages such as simple and easy preparation, low cost, high reproducibility, stability, wide linear dynamic range, and low detection limit offer that the developed composite electrode is an attractive canditate for real sample applications.

In the third part of the thesis, a new hybride nickel molybdate ($NiMoO_4$) compound was synthesized by hydrothermal synthesis method and then a composite material was prepared by incorporation of $NiMoO_4$ and GO for

simultenaous determination of ACP and TRP. The characterization studies by SEM and XRD indicate that a poor crystal structure of $NiMoO_3$ was formed with hydrothermal synthesis. However, the prepared composite material from 5% $NiMoO_4$ and 95% GO was shown almost same electrochemical properties such as electron transfer rate and active surface area with GO/GCE in the presence of in 0.1 mol L^{-1} KCl solution + 5.0 mmol L^{-1} $K_3[Fe(CN)_6]/K_4[Fe(CN)_6]$, while a higher electrocatalytic activity was observed towards for both ACP and TRP oxidation reaction at more negative potentials compare to the bare GCE, GO/GCE and $NiMoO_4$(5%)+GO(95%)/GCE in the presence of pH 5.0 AcH/Ac buffer solution. The higher electrocatalytic activity could be explaned by more interaction between the metal oxides and analytes compare with GO/GCE surafce.

A linear changing of peak currents of individual ACP or TRP concentrations were found and the calibration curves were constituted for ACP with two different linear parts at $NiMoO_4$(5%)+GO(95%)/GCE: the first linear part was obtained as from $0.1x10^{-6}$ to $1.0x10^{-6}$ M and the second linear part from $2.0x10^{-5}$ to $1.0x10^{-5}$ M and the calibartion curve was constructed in the concentration range of TRP from $0.6x10^{-6}$ – $6.0x10^{-5}$ M. The detection limits were calculated to be 10.0 nM ACP and 0.798 nM TRP respectively. On the other hand, the simultaneous detection of ACP and TRP were also investigated when the concentration of one species changed and the other was kept constant. In both type of studies, a linear current variations were obtained by increasing of both ACP and TRP concentrations**.**

The SWV method was used to investigate repeatability, reproducibility, and stability. To evaluate the repeatability of the modified electrode, the responses to the ACP and TRP were investigated for five different modified electrodes prepared in the same way. As an obvious result of this, the relative standard deviation (RSD) of the peak currents for ACP and TRP, respectively (n=5), were 1.64% and 1.54%, respectively. This demonstrates that the electrode exhibited satisfactory levels of repeatability. In order to investigate the repeatability of the electrode, the same electrode was utilized multiple times during the same day. The relative standard deviation (RSD) of the peak current was 0.26% for ACP and 0.36% for TRP.

Morever a stable peak currents of ACP and TRP were found in the presence at least 100 fold concentration of possible interferences of inorganic and organic

species. The addition of inorganic ions such as Cl-, NO^{3-}, and K^{+} ions, as well as organic molecules like glucose and ascorbic acid, had essentially no effect on the oxidation peak indicating that they did not interfere with the determination of ACP and TRP. However, the ACP and TRP peak current were affected by serotonin and dopamine concentrations that were 100 times higher. The developed composite electrode was applied successfully to detectin of ACP and TRP in synthetic urine samples.

REFERENCES

Abdelwahab, A. A., Elseman, A. M., Alotaibi, N. F., & Nassar, A. M. (2020). Simultaneous voltammetric determination of ascorbic acid, dopamine, acetaminophen and tryptophan based on hybrid trimetallic nanoparticles-capped electropretreated graphene. Microchemical Journal, 156, 104927.

Abdulla, S., Mathew, T. L., & Pullithadathil, B. (2015). Highly sensitive, room temperature gas sensor based on polyaniline-multiwalled carbon nanotubes (PANI/MWCNTs) nanocomposite for trace-level ammonia detection. Sensors and Actuators B: Chemical, 221, 1523-1534.

Ahamed, M., Akhtar, M. J., Khan, M. M., & Alhadlaq, H. A. (2021). SnO_2-doped ZnO/reduced graphene oxide nanocomposites: synthesis, characterization, and improved anticancer activity via oxidative stress pathway. International journal of nanomedicine, 89-104.

Alhans, R., Singh, A., Singhal, C., Narang, J., Wadhwa, S., & Mathur, A. (2018). Comparative analysis of single-walled and multi-walled carbon nanotubes for electrochemical sensing of glucose on gold printed circuit boards. Materials Science and Engineering: C, 90, 273-279.

Ali A, Chiang YW, Santos RM. X-ray Diffraction Techniques for Mineral Characterization (2022): A Review for Engineers of the Fundamentals, Applications, and Research Directions. Minerals. 12(2):205. https://doi.org/10.3390/min12020205

Alizadeh, M., Asrami, P. N., Altuner, E. E., Gulbagca, F., Tiri, R. N. E., Aygun, A., ... & Cheraghi, S. (2022). An ultra-sensitive rifampicin electrochemical sensor based on Fe_3O_4 nanoparticles anchored Multiwalled Carbon nanotube modified glassy carbon electrode. Chemosphere, 309, 136566.

REFERENCES (continued)

Aktürk, M., Karabiberoğlu, Ş. U., & Dursun, Z. (2018). Fabrication of Cu−CeO_2 coated multiwall carbon nanotube composite electrode for simultaneous determination of guanine and adenine. Electroanalysis, 30(2), 238-249.

Aktürk, M., & Dursun, Z., 2023, Fabrication of Co_3O_4 particles-modified multi-walled carbon nanotube and poly (phenosafranine) composite electrode for selective and sensitive rutin detection. Electroanalysis, e202200539.

Al-Kadhi, N. S., Pashameah, R. A., Ahmed, H. A., Alrefaee, S. H., Alamro, F. S., Faqih, H. H., ... & Mostafa, A. M. (2022). Preparation of NiO/MWCNTs nanocomposite for the removal of cadmium ions. Journal of Materials Research and Technology, 19, 1961-1971.

Ariga, K, Yamauchi, Y., Mori, T. and Hill, J.P., 2013, What can be done with the langmuir-blodgett method? Recent developments and its critical role in materials science, *Advance. Materials,* 25:6477–6512 pp.

Babaei, A., & Afrasiabi, M. (2015). A glassy carbon electrode modified with MCM-41/nickel hydroxide nanoparticle/multiwalled carbon nanotube composite as a sensor for the simultaneous determination of dopamine, piroxicam, and cefixime. Ionics, 21, 1731-1740.

Baezzat, M. R., & Jahromi, F. Z. (2022). Differential Pulse Voltammetric Determination of Acetaminophen Using Carbon Paste Electrode Modified with β-Cyclodextrin/Gold/Titanium Dioxide Nanocomposite. Journal of Analytical Chemistry, 77(1), 101-109.

Beitollahi, H., Garkani-Nejad, F., Tajik, S., & Ganjali, M. R. (2019). Voltammetric determination of acetaminophen and tryptophan using a graphite screen printed electrode modified with functionalized graphene oxide nanosheets

within a Fe_3O_4@ SiO_2 nanocomposite. Iranian journal of pharmaceutical research: IJPR, 18(1), 80.

Bokov, D., Turki Jalil, A., Chupradit, S., Suksatan, W., Javed Ansari, M., Shewael, I. H., ... & Kianfar, E. (2021). Nanomaterial by sol-gel method: synthesis and application. Advances in Materials Science and Engineering, 2021, 1-21.

Brito, J. L., & Barbosa, A. L. (1997). Effect of phase composition of the oxidic precursor on the HDS activity of the sulfided molybdates of Fe (II), Co (II), and Ni (II). Journal of Catalysis, 171(2), 467-475.

Brodie, B. C. (1859). XIII. On the atomic weight of graphite. Philosophical transactions of the Royal Society of London, (149), 249-259.

Chastain, J., & King Jr, R. C. (1992). Handbook of X-ray photoelectron spectroscopy. Perkin-Elmer Corporation, 40, 221.

Chen, D., Feng, H., & Li, J. (2012). Graphene oxide: preparation, functionalization, and electrochemical applications. Chemical reviews, 112(11), 6027-6053.

Chen, H., Yang, T., Liu, F., & Li, W. (2019). Electrodeposition of gold nanoparticles on Cu-based metal-organic framework for the electrochemical detection of nitrite. Sensors and Actuators B: Chemical, 286, 401-407.

Chikere, C. O., Hobben, E., Faisal, N. H., Kong-Thoo-Lin, P., & Fernandez, C. (2021). Electroanalytical determination of gallic acid in red and white wine samples using cobalt oxide nanoparticles-modified carbon-paste electrodes. Microchemical journal, 160, 105668.

REFERENCES (continued)

Chu, H., Wei, L., Cui, R., Wang, J., & Li, Y. (2010). Carbon nanotubes combined with inorganic nanomaterials: Preparations and applications. Coordination Chemistry Reviews, 254(9-10), 1117-1134.

Cook, S. F., King, A. D., van den Anker, J. N., & Wilkins, D. G. (2015). Simultaneous quantification of acetaminophen and five acetaminophen metabolites in human plasma and urine by high-performance liquid chromatography–electrospray ionization–tandem mass spectrometry: method validation and application to a neonatal pharmacokinetic study. Journal of Chromatography B, 1007, 30-42.

Çevikkalp, S. A., Löker, G. B., Yaman, M., & Amoutzopoulos, B. (2016). A simplified HPLC method for determination of tryptophan in some cereals and legumes. Food chemistry, 193, 26-29.

Creighton, J. R., & Ho, P. (2001). Introduction to chemical vapor deposition (CVD). Chemical vapor deposition, 2, 1-22.

Dalkıran, B., Erden, P. E., & Kılıç, E. (2017). Graphene and tricobalt tetraoxide nanoparticles based biosensor for electrochemical glutamate sensing. Artificial Cells, Nanomedicine, and Biotechnology, 45(2), 340-348.

Demir, N., Atacan, K., Ozmen, M., & Bas, S. Z. (2020). Design of a new electrochemical sensing system based on MoS_2–TiO_2/reduced graphene oxide nanocomposite for the detection of paracetamol. New Journal of Chemistry, 44(27), 11759-11767. https://doi.org/10.1039/D0NJ02298E.

Dinç, E., & Baleanu, D. (2002). Two new spectrophotometric approaches to the multicomponent analysis of the acetaminophen and caffeine in tablets by classical least-squares and principal component regression techniques. Il Farmaco, 57(1), 33-37.

REFERENCES (continued)

Dreyer, D. R., Park, S., Bielawski, C. W., & Ruoff, R. S. (2010). The chemistry of graphene oxide. Chemical society reviews, 39(1), 228-240.

Eagambaram, M., & Kumar, K. (2022). Design of an Efficient Tin Selenide-Based Ternary Nanocomposite Electrode for Simultaneous Determination of Paracetamol, Tryptophan, and Caffeine. ACS omega, 7(40), 35486-35495.

Fan, W., Zhang, L., & Liu, T. (2017). Graphene-carbon nanotube hybrids for energy and environmental applications. Springer Singapore:

Fu, K., Wang, Y., Yan, C., Yao, Y., Chen, Y., Dai, J., ... & Hu, L. (2016). Graphene oxide-based electrode inks for 3D-printed lithium-ion batteries. Advanced Materials, 28(13), 2587-2594.

Gholami, M., Zarei-jelyani, M., Babaiee, M., Baktashian, S., & Eqra, R. (2020). Physical vapor deposition of TiO_2 nanoparticles on artificial graphite: An excellent anode for high rate and long cycle life lithium-ion batteries. Ionics, 26, 4391-4399.

Gholivand, M. B., Mohammadi-Behzad, L., & Hosseinkhani, H. (2016). Application of a Cu–chitosan/multiwalled carbon nanotube film-modified electrode for the sensitive determination of rutin. Analytical biochemistry, 493, 35-43.

Goyal, R. N., Gupta, V. K., & Chatterjee, S. (2010). Voltammetric biosensors for the determination of paracetamol at carbon nanotube modified pyrolytic graphite electrode. Sensors and Actuators B: Chemical, 149(1), 252-258.

Gómez-Romero, P., & Sanchez, C. (Eds.). (2006). Functional hybrid materials. John Wiley & Sons.

REFERENCES (continued)

Guzmán, M. G., Dille, J., & Godet, S. (2009). Synthesis of silver nanoparticles by chemical reduction method and their antibacterial activity. Int J Chem Biomol Eng, 2(3), 104-111.

Hernández-Carabalí, L. A., Sachdeva, R., Rojas-Trigos, J. B., Marín, E., & Garcia, C. D. (2021). Monitoring the advanced oxidation of paracetamol using ZnO films via capillary electrophoresis. Journal of Water Process Engineering, 41, 102051.

Han, M., Jung, S., Lee, Y., Jung, D., & Kong, S. H. (2021). PEI-functionalized carbon nanotube thin film sensor for CO_2 gas detection at room temperature. Micromachines, 12(9), 1053.

Harsha, P. J., Thotakura, N., Kumar, M., Sharma, S., Mittal, A., Khurana, R. K., ... & Raza, K. (2019). A novel PEGylated carbon nanotube conjugated mangiferin: An explorative nanomedicine for brain cancer cells. Journal of Drug Delivery Science and Technology, 53, 101186.

Hazra, S. K., & Basu, S. (2016). Graphene-oxide nano composites for chemical sensor applications. C, 2(2), 12.

He, J. L., Yang, Y., Yang, X., Liu, Y. L., Liu, Z. H., Shen, G. L., & Yu, R. Q. (2006). β-Cyclodextrin incorporated carbon nanotube-modified electrode as an electrochemical sensor for rutin. Sensors and Actuators B: Chemical, 114(1), 94-100.

He, Q., Wu, Y., Tian, Y., Li, G., Liu, J., Deng, P., & Chen, D. (2019). Facile electrochemical sensor for nanomolar rutin detection based on magnetite nanoparticles and reduced graphene oxide decorated electrode. Nanomaterials, 9(1), 115.

REFERENCES (continued)

Huang, H., Zhu, W., Tao, X., Xia, Y., Yu, Z., Fang, J., & Zhang, W. (2012). Nanocrystal-constructed mesoporous single-crystalline Co_3O_4 nanobelts with superior rate capability for advanced lithium-ion batteries. ACS applied materials & interfaces, 4(11), 5974-5980.

Inkson, B. J. (2016). Scanning electron microscopy (SEM) and transmission electron microscopy (TEM) for materials characterization. In Materials characterization using nondestructive evaluation (NDE) methods (pp. 17-43). Woodhead publishing.

Isacfranklin, M., Deepika, C., Ravi, G., Yuvakkumar, R., Velauthapillai, D., & Saravanakumar, B. (2020). Nickel, bismuth, and cobalt vanadium oxides for supercapacitor applications. Ceramics International, 46(18), 28206-28210.

Jang, Y., Kim, S. M., Spinks, G. M., & Kim, S. J. (2020). Carbon nanotube yarn for fiber-shaped electrical sensors, actuators, and energy storage for smart systems. Advanced Materials, 32(5), 1902670.

Kakaei, K., Esrafili, M. D., & Ehsani, A. (2019). Graphene-based electrochemical supercapacitors. In Interface science and technology (Vol. 27, pp. 339-386). Elsevier.

Karabiberoğlu, Ş. U., & Dursun, Z. (2018). Fabrication of nickel coated graphene oxide composite electrode for sensitive determination of Rutin. Journal of Electroanalytical Chemistry, 815, 76-85.

Karthika, A., Karuppasamy, P., Selvarajan, S., Suganthi, A., & Rajarajan, M. (2019). Electrochemical sensing of nicotine using $CuWO_4$ decorated reduced graphene oxide immobilized glassy carbon electrode. Ultrasonics sonochemistry, 55, 196-206.

REFERENCES (continued)

Karyaoui, M., Jemia, D. B., Daoudi, M., Bardaoui, A., Boukhachem, A., Amlouk, M., & Chtourou, R. (2021). Physical properties of graphene oxide GO-doped ZnO thin films for optoelectronic application. Applied Physics A, 127, 1-14.

Kavya, K. V., Muthu, D., Varghese, S., Pattappan, D., Kumar, R. R., & Haldorai, Y. (2022). Glassy carbon electrode modified by gold nanofibers decorated iron metal–organic framework nanocomposite for voltammetric determination of acetaminophen. Carbon Letters, 32(6), 1441-1449.

Keerthi, M., Boopathy, G., Chen, S. M., Chen, T. W., Rwei, S. P., & Liu, X. (2019). An efficient electrochemical sensor based on Ag nanoparticle decorated MnO_2/reduced graphene oxide ternary nanocomposite for detection of acetaminophen in human urine sample. Int. J. Electrochem. Sci, 14, 346-358. http://dx.doi.org/10.20964/2019.01.59.

Kochen, W., & Steinhart, H. (Eds.). (1994). L-Tryptophan: current prospects in medicine and drug safety. Walter de Gruyter.

Koçak, Ç.C. and Dursun, Z., 2013, Simultaneous determination of ascorbic acid, epinephrine and uric acid at over-oxidized poly(p-aminophenol) film modified electrode, Journal of Electroanalytical Chemistry, 694:94–103 pp

Komura, T., Ishihara, M., Yamaguchi, T., & Takahashi, K. (2000). Charge-transporting properties of electropolymerized phenosafranin in aqueous media. Journal of Electroanalytical Chemistry, 493(1-2), 84-92.

Korkmaz, S., & Kariper, İ. A. (2020). Graphene and graphene oxide based aerogels: Synthesis, characteristics and supercapacitor applications. Journal of Energy Storage, 27, 101038.

REFERENCES (continued)

Kounaves, S. P. (1997). Voltammetric techniques. Handbook of instrumental techniques for analytical chemistry, 709-726.

Kiaeefar, A., Bolourian, H., Raoufi, A., Rajabi, N., & Ebrahimi, M. (2022). Voltammetric Determination of Acetaminophen with Ag/PANI/PW12 Nanocomposites-Modified Carbon Paste Electrodes. Russian Journal of Physical Chemistry A, 96(6), 1273-1279.

Kloprogge et al., 2020, Handbook of Mineral Spectroscopy, Volume 1: X-ray Photoelectron Spectra, Kloprogge J. T., Elsevier, USA

Kumar, S., Singh, A., Singh, R., Singh, S., Kumar, P., & Kumar, R. (2020). Facile h-MoO_3 synthesis for NH_3 gas sensing application at moderate operating temperature. Sensors and Actuators B: Chemical, 325, 128974.

Lavanya, A. L., Kumari, K. G. B., Prasad, K. R. S., & Kumar Brahman, P. (2021). Nickel and Tungsten Bimetallic Nanoparticles Modified Pencil Graphite Electrode: A High-performance Electrochemical Sensor for Detection of Endocrine Disruptor Bisphenol A. Electroanalysis, 33(3), 591-600.

Li, L., Li, Y., Gao, S., & Koshizaki, N. (2009). Ordered Co_3O_4 hierarchical nanorod arrays: tunable superhydrophilicity without UV irradiation and transition to superhydrophobicity. Journal of Materials Chemistry, 19(44), 8366-8371.

Li, X., Li, Y., Xie, S., Zhou, Y., Rong, J., & Dong, L. (2022). Zinc-based energy storage with functionalized carbon nanotube/polyaniline nanocomposite cathodes. Chemical Engineering Journal, 427, 131799.

Li, Y., Zhang, S., Ma, M., Mu, X., Zhang, Y., Du, J., ... & Zhang, Z. (2019). Manganese-doped nickel molybdate nanostructures for high-performance asymmetric supercapacitors. Chemical Engineering Journal, 372, 452-461.

REFERENCES (continued)

Lima, L. F., Matos, C. F., Gonçalves, L. C., Salvatierra, R. V., Cava, C. E., Zarbin, A. J. G., & Roman, L. S. (2016). Water based, solution-processable, transparent and flexible graphene oxide composite as electrodes in organic solar cell application. Journal of Physics D: Applied Physics, 49(10), 105106.

Liu, L., Ma, W., & Zhang, Z. (2011). Macroscopic carbon nanotube assemblies: preparation, properties, and potential applications. Small, 7(11), 1504-1520.

Liu, S. F. (2013). Sensitive fluorometric method for the determination of rutin in combined tablet dosage form. Indian Journal of Pharmaceutical Sciences, 75(5), 614.

Liu, M. C., Kang, L., Kong, L. B., Lu, C., Ma, X. J., Li, X. M., & Luo, Y. C. (2013). Facile synthesis of $NiMoO_4 \cdot x\ H_2O$ nanorods as a positive electrode material for supercapacitors. Rsc Advances, 3(18), 6472-6478.

Liu, Y., Li, Q., Ma, K., Yang, G., & Wang, C. (2019). Graphene oxide wrapped CuV_2O_6 nanobelts as high-capacity and long-life cathode materials of aqueous zinc-ion batteries. ACS nano, 13(10), 12081-12089.

Lu, J. (2021). A perspective on new opportunities in atom-by-atom synthesis of heterogeneous catalysts using atomic layer deposition. Catalysis Letters, 151, 1535-1545.

Luo, G., Zou, R., Niu, Y., Zhang, Y., Zhang, B., Liu, J., ... & Sun, W. (2020). Fabrication of ZIF-67@ three-dimensional reduced graphene oxide aerogel nanocomposites and their electrochemical applications for rutin detection. Journal of Pharmaceutical and Biomedical Analysis, 190, 113505.

Malinauskas, A. (2001). Chemical deposition of conducting polymers. polymer, 42(9), 3957-3972.

REFERENCES (continued)

Mauludin, R., Müller, R. H., & Keck, C. M. (2009). Development of an oral rutin nanocrystal formulation. International journal of pharmaceutics, 370(1-2), 202-209.

Mazloum-Ardakani, M., Beitollahi, H., Taleat, Z., Naeimi, H., & Taghavinia, N. (2010). Selective voltammetric determination of d-penicillamine in the presence of tryptophan at a modified carbon paste electrode incorporating TiO_2 nanoparticles and quinizarine. Journal of Electroanalytical Chemistry, 644(1), 1-6.

Menezes, P. W., Indra, A., González-Flores, D., Sahraie, N. R., Zaharieva, I., Schwarze, M., ... & Driess, M. (2015). High-performance oxygen redox catalysis with multifunctional cobalt oxide nanochains: morphology-dependent activity. ACS Catalysis, 5(4), 2017-2027.

Mehmandoust, M., Erk, N., Alizadeh, M., & Salmanpour, S. (2021). Voltammetric carbon nanotubes based sensor for determination of tryptophan in the milk sample. Journal of Food Measurement and Characterization, 15(6), 5288-5295.

Miyoshi, K., 2002, Surface Characterization Techniques: An Overview, Glenn Research Center, Ohio, http://ntrs.nasa.gov/archive/nasa/casi.ntrs.nasa.gov/20020070606.pdf [available: 20 August 2015].

Muralikrishna, S., Sureshkumar, K., Varley, T. S., Nagaraju, D. H., & Ramakrishnappa, T. (2014). In situ reduction and functionalization of graphene oxide with L-cysteine for simultaneous electrochemical determination of cadmium (II), lead (II), copper (II), and mercury (II) ions. Analytical Methods, 6(21), 8698-8705.

REFERENCES (continued)

Nesbitt, H. W., & Banerjee, D. J. A. M. (1998). Interpretation of XPS Mn (2p) spectra of Mn oxyhydroxides and constraints on the mechanism of MnO2 precipitation. American Mineralogist, 83(3-4), 305-315.

Nie, X., Zhang, R., Tang, Z., Wang, H., Deng, P., & Tang, Y. (2020). Sensitive and selective determination of tryptophan using a glassy carbon electrode modified with nano-CeO_2/reduced graphene oxide composite. Microchemical Journal, 159, 105367.

Niizeki, N., 1986. What are hybrid materials. Sensor Tech. 6 (2), 42-44.

N. Laube, B. Mohr, A. Hesse,2001, Laser-probe-based investigation of the evolutionof particle size distributions of calcium oxalate particles formed in artificialurines, J. Cryst. Growth 233, 367–374.

OBAIDULLAH, I. (2019). Carbon nanotube membranes for water purification: Developments, challenges, and prospects for the future. Separation and Purification Technology, 209, 307-337.

Parashar, M., Shukla, V. K., & Singh, R. (2020). Metal oxides nanoparticles via sol–gel method: a review on synthesis, characterization and applications. Journal of Materials Science: Materials in Electronics, 31, 3729-3749.

Patella, B., Sortino, A., Aiello, G., Sunseri, C., & Inguanta, R. (2019, July). Reduced graphene oxide decorated with metals nanoparticles electrode as electrochemical sensor for dopamine. In 2019 IEEE International Conference on Flexible and Printable Sensors and Systems (FLEPS) (pp. 1-3). IEEE.

Plachá, D., & Jampilek, J. (2019). Graphenic materials for biomedical applications. Nanomaterials, 9(12), 1758.

REFERENCES (continued)

Poo-arporn, Y., Pakapongpan, S., Chanlek, N., & Poo-arporn, R. P. (2019). The development of disposable electrochemical sensor based on Fe_3O_4-doped reduced graphene oxide modified magnetic screen-printed electrode for ractopamine determination in pork sample. Sensors and Actuators B: Chemical, 284, 164-171.

Pushpanjali, P. A., Manjunatha, J. G., Amrutha, B. M., & Hareesha, N. (2021). Development of carbon nanotube-based polymer-modified electrochemical sensor for the voltammetric study of Curcumin. Materials Research Innovations, 25(7), 412-420.

Rajabi, H., Noroozifar, M., & Khorasani-Motlagh, M. (2016). Graphite paste electrode modified with Lewatit® FO36 nano-resin for simultaneous determination of ascorbic acid, acetaminophen and tryptophan. Analytical Methods, 8(8), 1924-1934.

Ren, S., Feng, R., Cheng, S., Huang, L., Wang, Q., & Zheng, Z. (2022). Construction of a sensitive electrochemical sensor based on hybrid 1 T/2H MoS_2 nanoflowers anchoring on rGO nanosheets for the voltammetric determination of acetaminophen. Microchemical Journal, 175, 107129.

Reynolds, D. M. (2003). Rapid and direct determination of tryptophan in water using synchronous fluorescence spectroscopy. Water Research, 37(13), 3055-3060.

Roy, K., Mukherjee, A., Maddela, N. R., Chakraborty, S., Shen, B., Li, M., ... & Cruzatty, L. C. G. (2020). Outlook on the bottleneck of carbon nanotube in desalination and membrane-based water treatment—a review. Journal of Environmental Chemical Engineering, 8(1), 103572.

REFERENCES (continued)

Senthilkumar, B., & Selvan, R. K. (2014). Hydrothermal synthesis and electrochemical performances of 1.7 V $NiMoO_4 \cdot xH2O||$ $FeMoO_4$ aqueous hybrid supercapacitor. Journal of colloid and interface science, 426, 280-286.

Shafi, P. M., Dhanabal, R., Chithambararaj, A., Velmathi, S., & Bose, A. C. (2017). α-MnO_2/h-MoO_3 hybrid material for high performance supercapacitor electrode and photocatalyst. ACS Sustainable Chemistry & Engineering, 5(6), 4757-4770.

Sharma, S. (2018). Preparation of Graphene and it's Derivatives for Biosensing Application.

Sheng, K., Zhang, Q., Li, L., Wang, Y., & Ye, B. (2020). A new voltammetric sensor and its application in pharmaceutical analysis for rutin. Journal of Environmental Science and Health, Part A, 55(7), 837-846.

Shi, L., Wang, Z., Wu, N., Chen, X., Yang, G., & Liu, W. (2020). Reduced graphene/polydopamine-supported Au@ Pt/Au nanoparticles for electrochemical detection of acetaminophen. International Journal of Electrochemical Science, 15, 3922-3934.

Singh, A., Verma, N., & Kumar, K. (2019). Hybrid composites: a revolutionary trend in biomedical engineering. In Materials for Biomedical Engineering (pp. 33-46). Elsevier.

Sohouli, E., Khosrowshahi, E. M., Radi, P., Naghian, E., Rahimi-Nasrabadi, M., & Ahmadi, F. (2020). Electrochemical sensor based on modified methylcellulose by graphene oxide and Fe_3O_4 nanoparticles: Application in the analysis of uric acid content in urine. Journal of Electroanalytical Chemistry, 877, 114503.

REFERENCES (continued)

Song, Z., & Wang, L. (2001). Chemiluminescence investigation of detection of rutin in medicine and human urine using controlled-reagent-release technology. Journal of Agricultural and Food Chemistry, 49(12), 5697-5701.

Song, M. J., Hwang, S. W., & Whang, D. (2010). Non-enzymatic electrochemical CuO nanoflowers sensor for hydrogen peroxide detection. Talanta, 80(5), 1648-1652.

Sun, Y., Hu, X., Luo, W., & Huang, Y. (2012). Ultrafine MoO 2 nanoparticles embedded in a carbon matrix as a high-capacity and long-life anode for lithium-ion batteries. Journal of Materials Chemistry, 22(2), 425-431.

Sun, Y., Guo, T., Sui, Y., & Li, F. (2003). Quantitative determination of rutin, quercetin, and adenosine in Flos Carthami by capillary electrophoresis. Journal of separation science, 26(12-13), 1203-1206.

Şenocak, A., Korkmaz, E., Khataee, A., & Demirbas, E. (2022). A facile and synergetic strategy for electrochemical sensing of rutin antioxidant by Ce–Cr doped magnetite@ rGO. Materials Chemistry and Physics, 275, 125298.

Taei, M., & Jamshidi, M. S. (2017). A voltammetric sensor for simultaneous determination of ascorbic acid, noradrenaline, acetaminophen and tryptophan. Microchemical Journal, 130, 108-115.

Tajik, S., Taher, M. A., & Beitollahi, H. (2013). First report for simultaneous determination of methyldopa and hydrochlorothiazide using a nanostructured based electrochemical sensor. Journal of Electroanalytical Chemistry, 704, 137-144.

Tajyani, S., & Babaei, A. (2018). A new sensing platform based on magnetic Fe_3O_4@NiO core/shell nanoparticles modified carbon paste electrode for simultaneous voltammetric determination of Quercetin and Tryptophan. Journal of Electroanalytical Chemistry, 808, 50-58.

REFERENCES (continued)

Tanner, E. E., & Compton, R. G. (2018). How can electrode surface modification benefit electroanalysis?. Electroanalysis, 30(7), 1336-1341.

Tığ, G. A. (2017). Development of electrochemical sensor for detection of ascorbic acid, dopamine, uric acid and l-tryptophan based on Ag nanoparticles and poly (l-arginine)-graphene oxide composite. Journal of Electroanalytical Chemistry, 807, 19-28.

Tural, H., Gökçel, H.İ. and Ertaş, F.N., 2006, Enstrümental analiz I elektroanalitik yöntemler, Ege Üniversitesi Yayınları Fen Fakültesi, 186, İzmir, 339s.

Uygun, Z.O. and Uygun, H.D.E., 2014, A short footnote: Circuit design for faradaic impedimetric sensors and biosensors, Sensors and Actuators, B, 202:448–453 pp.

Uzun, D. (2021). Determination of paracetamol based on 3-amino-4H-1, 2, 4-triazole coated glassy carbon surface in pharmaceutical sample. Electroanalysis, 33(7), 1699-1706.

Uzun, D., & Tabanlıgil Calam, T. (2022). Electrochemical Behavior and Ultrasensitive, Simple and Effective Voltammetric Determination of Acetaminophen Using Modified Glassy Carbon Electrode Based on 4 Hydroxyquinoline-3-Carboxylic Acid. Electroanalysis. https://doi.org/10.1002/elan.202200182.

Qu, D., Ji, W., & Qu, H. (2022). Probing process kinetics in batteries with electrochemical impedance spectroscopy. Communications Materials, 3(1), 61.

Wallace, G. G., Teasdale, P. R., Spinks, G. M., & Kane-Maguire, L. A. (2002). Conductive electroactive polymers: intelligent materials systems. CRC press.

REFERENCES (continued)

Wang, Y., Zhang, B., Tang, Y., Zhao, F., & Zeng, B. (2021). Fabrication and application of a rutin electrochemical sensor based on rose-like AuNPs-MoS_2-GN composite and molecularly imprinted chitosan. Microchemical Journal, 168, 106505.

Wei, Z., Guo, S., Cheng, L., Li, T., Zhang, Y., & Yang, H. (2019). Simultaneous determination of acetaminophen and tyrosine using screen-printed electrochemical sensor based on MWCNTs-doped poly (glycine)/poly (acrylic acid) conducting polymers. Int. J. Electrochem. Sci, 14, 6748-6758.

White, R. J., Luque, R., Budarin, V. L., Clark, J. H., & Macquarrie, D. J. (2009). Supported metal nanoparticles on porous materials. Methods and applications. Chemical Society Reviews, 38(2), 481-494.

Wong, A., Santos, A. M., & Fatibello-Filho, O. (2018). Simultaneous determination of paracetamol and levofloxacin using a glassy carbon electrode modified with carbon black, silver nanoparticles and PEDOT: PSS film. Sensors and Actuators B: Chemical, 255, 2264-2273.

Xia, H., Zhu, D., Luo, Z., Yu, Y., Shi, X., Yuan, G., & Xie, J. (2013). Hierarchically structured Co_3O_4@ Pt@ MnO_2 nanowire arrays for high-performance supercapacitors. Scientific reports, 3(1), 1-8.

Xing, S., Xu, H., Chen, J., Shi, G., & Jin, L. (2011). Nafion stabilized silver nanoparticles modified electrode and its application to Cr (VI) detection. Journal of Electroanalytical Chemistry, 652(1-2), 60-65.

Xu, H., Li, Y., Tang, H. W., Liu, C. M., & Wu, Q. S. (2010). Determination of rutin with UV-Vis spectrophotometric and laser-induced fluorimetric detections using a non-scanning spectrometer. Analytical letters, 43(6), 893-904.

REFERENCES (continued)

Yamada, A., Sasabe, H., Osada, Y., Shiroda, Y., 1989. Concepts of Hybrid Materials, Hybrid Materials—Concept and Case Studies. ASM International, OH.

Vinoth, S., & Wang, S. F. (2023). Construction of functionalized carbon nanotube@ metal oxide nanocomposite for high-performance electrochemical measurement of antipyretic drug in water samples. Environmental Science and Pollution Research, 1-14.

Yan, N., Hu, L., Li, Y., Wang, Y., Zhong, H., Hu, X., ... & Chen, Q. (2012). Co_3O_4 nanocages for high-performance anode material in lithium-ion batteries. The Journal of Physical Chemistry C, 116(12), 7227-7235.

Yao, J., Gong, Y., Yang, S., Xiao, P., Zhang, Y., Keyshar, K., ... & Ajayan, P. M. (2014). $CoMoO_4$ nanoparticles anchored on reduced graphene oxide nanocomposites as anodes for long-life lithium-ion batteries. ACS Applied Materials & Interfaces, 6(22), 20414-20422.

Yousefipour, K., Sarraf-Mamoory, R., & Yourdkhani, A. (2022). Supercapacitive properties of nickel molybdate/rGO hybrids prepared by the hydrothermal method. Surfaces and Interfaces, 29, 101638.

Zhang, H., & Liu, S. (2020). Electrochemical sensors based on nitrogen-doped reduced graphene oxide for the simultaneous detection of ascorbic acid, dopamine and uric acid. Journal of Alloys and Compounds, 842, 155873.

Zhang, Z., Bao, F., Zhang, Y., Feng, L., Ji, Y., Zhang, H., ... & Liu, X. (2015). Formation of hierarchical $CoMoO_4$@ MnO_2 core–shell nanosheet arrays on nickel foam with markedly enhanced pseudocapacitive properties. Journal of Power Sources, 296, 162-168.

REFERENCES (continued)

Zhen, Q., Xu, B., Ma, L., Tian, G., Tang, X., & Ding, M. (2011). Simultaneous determination of tryptophan, kynurenine and 5-hydroxytryptamine by HPLC: application in uremic patients undergoing hemodialysis. Clinical biochemistry, 44(2-3), 226-230.

Zhou, Y., Song, C., Chen, Z., & Zhou, Q. (2021). Fabrication of h-MoO3 Nanorods and the Properties of the MoO3/WEP Composite Coatings Research. Journal of Composites Science, 5(8), 207.

Zhu, C., Yang, G., Li, H., Du, D., & Lin, Y. (2015). Electrochemical sensors and biosensors based on nanomaterials and nanostructures. Analytical chemistry, 87(1), 230-249.

ACKNOWLEDGEMENT

My supervisor, Prof. Dr. Zekerya DURSUN, has been very supportive, has provided me with helpful advise, and has been very patient with me. For all of these things, I would want to offer my sincere appreciation and thanks to him. It was a wonderful opportunity to work on my PhD studies with his support and get insight from his previous experience conducting research.

I would like to express my appreciation to the members of my doctoral committee, Prof. Dr. H. İsmet Gokcel and Prof. Dr. Filiz KURALAY, for the valuable discussions and accessibility they provided throughout the duration of my PhD studies.

I am grateful to my role model, my dear mother, Beşbine AKTÜRK, for her contributions to my presence of today. I would like to thank to my father Abdullah AKTÜRK, and all my dear family members (Ebru AKTÜRK TEKE; Coşkun TEKE; Banu AKTÜRK; Eftun ELMACI and Soner AKTÜRK) for always supporting me in my whole education life.

I would also like to my dear and precious nieces Belis TEKE and Tülin Elif ELMACI. Thank you for being with me throughout my PhD studies and always making me smile. I am grateful for your existence.

I am very grateful to especially PhD. Student Berkay LEŞKERİ, PhD Şebnem Gül İLARSLAN and all other members of Dursun Research Group and PhD Ayşegül ERDOĞAN because of their friendships we shared as well as the collaboration they provided me with my laboratory work.

Finally,. I would also like to thank Ege University Research Foundation. (Project number FDK-2020-21471).

Merve AKTÜRK

December 2023, İZMİR

CIRRICULUM VITAE

Education
2008-2013: BSc Degree in Chemisty Department of Ege University, Izmir, Turkey
2014-2016: MSc Degree in Chemistry Department of Ege University, Izmir, Turkey.
2017- 2023: PhD Degree in Chemistry Department of Ege University, Izmir, Turkey.
Doktora Tezine Bağlı Yayın ve Bildiriler
Kongre Sunumları
-33. Ulusal Kimya Kongresi, 2021, Online
-17th INTERNATIONAL NANOSCIENCE & NANOTECHNOLOGY CONFERENCE 5-8 Eylül 2022, **Ankara-Türkiye**
SCI Yayın
DURSUN, Z., & AKTÜRK, M. (2023) Fabrication of Co_3O_4 particles–modified multi-walled carbon nanotube and poly (phenosafranine) composite electrode for selective and sensitive rutin detection. Electroanalysis, e202200539.